

**From the Institute of Physics
of the University of Lübeck
Director: Prof. Dr. Christian G. Hübner**

High Pressure Single Molecule FRET

Dissertation
for Fulfillment of
Requirements
for the Doctoral Degree
of the University of Lübeck

from the Department of Natural Sciences

Submitted by

Sven Schneider
from Freiburg im Breisgau
Lübeck 2017

First referee: Prof. Dr. Christian G. Hübner

Second referee: Prof. Dr. Lars Redecke

Date of oral examination: 10.7.2017

Approved for printing: Lübeck, 13.7.2017

Zusammenfassung

Spektroskopische Untersuchungen unter Hochdruck helfen ein besseres Verständnis von biologischen Molekülen zu erlangen. Um zum Beispiel die Proteinfaltung besser verstehen zu können, muss das Protein zunächst einmal entfaltet werden. Dies kann durch Temperatur, Denaturierungsmittel, pH-Veränderung oder Druck geschehen. Im Gegensatz zu anderen Entfaltungsmethoden ist die Druckentfaltung sauber, reversibel und beeinträchtigt innere Wechselwirkungen ausschließlich durch Veränderungen der Abstände der einzelnen Komponenten, wohingegen die Gesamtenergie fast gleich bleibt [9].

Durch die Betrachtung einzelner Moleküle werden mehr Details sichtbar, da durch die Trennung verschiedener Populationen, Heterogenitäten untersucht werden können. Sogar wenn sie in der Minderheit sind, können entfaltete oder gefaltete Proteine oder auch verschiedenen Proteinkonformationen separat untersucht werden. FRET unter Einzelmolekülkonzentration (sm-FRET) ist eine wirkungsvolle Methode zur Untersuchung der Proteinfaltung, da sie nicht nur zur Untersuchung des Entfaltungsgleichgewichts und zur Bestimmung der thermodynamischen Parameters eines Proteins eingesetzt werden kann, sondern auch um die Größe der verschiedenen Konformationen und des entfalteten Zustandes zu bestimmen.

Inspiziert von der Arbeit von Gratton et al. [56, 60], wurde eine Kapillare verwendet um eine Einzelmolekülfluoreszenzmessung, speziell smFRET, unter Hochdruck zu realisieren. Die von Gratton et al. verwendete zylindrische Kapillare ermöglichte es ihnen Objektive mit hoher numerischer Apertur zu benutzen, um Einzelmolekülfluoreszenzuntersuchungen mit Zweiphotonenanregung durchzuführen. Die zylindrische Bauart mit einer Druckstabilität von bis zu 4000 bar ist druckstabiler als eine quadratische mit einer Druckstabilität von bis zu 2000 bar [56, 60]. Jedoch bricht die gekrümmte Oberfläche der zylindrischen Kapillare das Licht ungünstig, was zu einer enormen Vergrößerung des Fokaltvolumens und chromatischen Aberrationen führt. Um eine bessere optische Qualität zu gewährleisten, und somit auch eine Einzelmolekülfluoreszenzuntersuchung mit Einzelphotonanregung zu ermöglichen, verwenden wir eine quadratische, anstatt einer zylindrischen Kapillare.

Die Kapillaren bestehen aus Quarzglas, da es sehr viel druckstabiler als Borosilikatglas ist. Standardobjektive mit hoher numerischer Apertur sind jedoch für Borosilikat gemacht, sodass der unterschiedliche Brechungsindex von Quarzglas zu optischen Aberrationen führt. Um diese optischen Aberrationen zu minimieren und Effekte, die durch die Seitenwände auftreten, zu vermeiden, wurden die optischen Eigenschaften mit einer neuen Anordnung verbessert, bei der die Kapillare, schwimmend in einem optischen Gel mit passendem Brechungsindex, auf einem Quarzdeckglas liegt. Verschiedene Objektivkorrekturringeinstellungen wurden für die neue Anordnung getestet: Für die Einstellung mit dem kleinsten Fokaltvolumen, das durch ein

Rasterbild eines Fluoreszenzmikrokügelchens bestimmt wurde, ist das Fokalvolumen vergleichbar mit dem einer Deckglassmessung. Leider zeigte sich aber für diese Einstellung eine starke chromatische Aberration in z-Richtung. So musste für Zweifarbenexperimente, wie beispielsweise eine FRET-Messung, ein Kompromiss zwischen der chromatischen z- Verschiebung und der Größe des Fokalvolumens gefunden werden. Anhand von FRET-benchmarks, wurde die optimale Objektivkorrekturringeinstellung für Zweifarbenexperimente bestimmt.

Durch eine Fluoreszenzkorrelationsmessung (FCS-benchmark), konnte für Einfarbenexperimente gezeigt werden, dass die Anregungs-und Detektionsqualität einer Deckglassmessung in der Kapillare erreicht werden kann. Für Zweifarbenexperimente, zeigte ein FRET-benchmark, dass smFRET-Messungen unter Druck durch quadratische Kapillaren realisiert werden können und mit der neuen Anordnung weiter verbessert wurden, jedoch nicht die Messqualität einer Deckglassmessung erreichen.

Proteinentfaltung durch Denaturierungsmittel [29] oder Temperaturänderung [77] wurden mittels smFRET untersucht. Mit unserem Aufbau wird auch die Druckentfaltung mit smFRET messbar. FRET-messungen des Entfaltungsübergangs des Zwei-Domänen-Proteins SlyD, des Model Zwei-Zustands-Falters CspA und des intrinsisch entfalteten Hefe-Frataxins werden vorgestellt. Die FRET-Histogramme können ausgewertet werden, um die thermodynamischen Parameter des Entfaltungsübergangs und die Größe der entfalteten Kette zu bestimmen. Im Gegensatz zu einer Erhöhung der Konzentration des Denaturierungsmittels Guanidiniumchlorid oder auch durch eine Temperaturänderung, beeinflusst eine Druckerhöhung die Größe der entfalteten Kette nur schwach.

Abstract

Spectroscopic investigations at high pressure help to get a better understanding of biological molecules. For example to understand protein folding, the protein has to be unfolded reversibly. This can be done by temperature, the addition of denaturants, pH-changes or pressure. In contrast to other unfolding methods, pressure unfolding is clean, reversible and affects internal interactions exclusively by the changes in the distances of the components, whereas the total energy remains almost constant [9].

Investigated on a single molecule level, more details become apparent, because heterogeneities can be investigated by separating different populations. Unfolded and folded proteins or different conformations can be investigated separately, even if they are in minority. FRET under single molecule concentration (smFRET) is a powerful method to investigate protein unfolding, because it can not only be used to investigate the unfolding equilibrium and the thermodynamic parameters of a protein, but also to probe the dimension of the different conformations and the dimension of the unfolded chain.

To realize single molecule fluorescence under pressure, particularly smFRET, a capillary is used, inspired by the work of Gratton et al. [56, 60]. They enabled the use of high numerical aperture objectives for single molecule detection with two photon excitation with a cylindrical capillary. A cylindrical shape is more pressure stable than a square shape with a pressure range up to 4000 bar, instead of 2000 bar in the square capillary [56, 60]. However, the cylindrical capillary's curved surface bends the light which leads to an enormous change of the focal volume and chromatic aberrations. So for a better optical quality, to realize a single molecule measurement with single photon excitation, we used a square, instead of a cylindrical shape.

The capillaries are made of fused silica, because fused silica is much more pressure stable than borosilicate glass. Standard high numerical aperture objectives are made for borosilicate, hence the different refractive index of fused silica leads to optical aberrations. To minimize these aberrations and to avoid sidewall effects, we further improved the imaging properties by a new arrangement, placing the capillary on top of a fused silica coverslip, while immersing the capillary in an optical gel of suitable refractive index. Different objective correction collar settings have been tested for the new arrangement: For the setting with the smallest focal volume, measured by a scan of a fluorescent microsphere (focal volume benchmark), the focal volume is actually comparable to that of a coverslip focus. Unfortunately the chromatical aberrations in z-direction became stronger for this setting. So for two color experiments like a FRET-measurement, we had to find a compromise between the chromatical z-shift and the size of the focal volume. According to FRET-benchmarks, the optimal correction collar setting for two color experiments has been determined.

By a fluorescence correlation spectroscopy measurement (FCS-benchmark), we could show that for single color experiments we get the same excitation- and detection-quality as on a coverslip. For two color experiments, a FRET benchmark showed that a smFRET measurement under pressure could be realized with the square capillary and further improved with the new arrangement, but the measurement quality is not as good as on a bare coverslip.

Protein unfolding with denaturants [29] or temperature [77] has been followed with single molecule FRET. With our setup, also pressure unfolding becomes accessible. FRET-measurements of the unfolding process of the two domain protein SlyD, the model two-state folder CspA and the intrinsically unfolded yeast-Frataxin are presented. The FRET histograms can be interpreted to determine the thermodynamic parameters of the unfolding transition and to probe the dimension of the unfolded chain. In contrast to the increase of the concentration of the denaturant Guanidiniumchloride or by a change of temperature, an increase of pressure only slightly influenced the size of the unfolded chain.

Contents

1	Introduction	1
2	Fundamentals	5
2.1	Photoluminescence	5
2.2	The transition rates	5
2.3	The triplet state	8
2.4	Fluorescence saturation	10
2.5	Fluorescence quenching and bleaching	10
2.6	Fluorescence measurement	11
2.7	Single molecule fluorescence	11
2.8	Fluorescence resonance energy transfer (FRET)	12
2.9	Single molecule FRET	15
2.10	Fluorescence and pressure	17
2.11	FCS measurement	18
2.12	TCSPC lifetime measurement	23
2.13	Confocal microscopy	24
2.13.1	Confocal principle	24
2.13.2	Excitation	24
2.13.3	Detection	25
2.13.4	Molecular detection efficiency	25
2.13.5	Signal to noise ratio	26
2.14	Protein unfolding	27
2.14.1	Denaturation by chemical influences	28
2.14.2	Temperature denaturation	29
2.14.3	Pressure denaturation	30
2.14.4	Thermodynamics of protein folding	32
2.14.5	Mechanism of the folding process	38
2.14.6	The denatured or unfolded state	41
3	Material and methods	44
3.1	Confocal microscope	44
3.2	Pressure setup	46
3.2.1	High pressure microscopy	46
3.2.2	Reduction of optical aberrations and the new arrangement	50

CONTENTS

3.2.3	Theoretical pressure stability	53
3.3	Temperature control	56
3.4	Samples	56
3.4.1	Dyes	57
3.4.2	Fluorescent microspheres	58
3.4.3	dsDNA	60
3.4.4	SlyD (PDB ID: 2K8I)	60
3.4.5	CspA (PDB ID: 2L15)	61
3.4.6	Frataxin (PDB ID: 2GA5)	63
3.4.7	Buffer	64
3.5	Data Reduction	66
3.5.1	FCS measurement	66
3.5.2	Focal volume measurement	68
3.5.3	FRET measurement	69
3.5.4	Fluorescence lifetime measurement	71
4	Results and discussion	72
4.1	Correction collar benchmark	72
4.1.1	Fret benchmark	72
4.1.2	Focal volume benchmark	74
4.1.3	FCS benchmark	77
4.1.4	Discussion	78
4.2	Comparison of the coverslip, the bare capillary and the new arrangement . . .	78
4.2.1	FCS benchmark	78
4.2.2	Focal volume benchmark	81
4.2.3	FRET benchmark	85
4.2.4	Discussion	90
4.3	Pressure evaluation	91
4.3.1	Discussion	94
4.4	Temperature evaluation	94
4.4.1	Discussion	96
4.5	Protein unfolding	96
4.5.1	SlyD	96
4.5.2	CspA	99
4.5.3	Frataxin	106

5	Conclusion	112
5.1	The quality of a fluorescence measurement in the high-pressure capillary	112
5.2	Protein unfolding by pressure	113
6	Outlook	115
A	Appendix	116
A.1	Capillary handling	116
A.2	Pictures of the square fused silica capillary taken with a Koyence VHX5000 digital microscope	118
A.3	Calculation of the optimal relation between the fused silica and the borosilica thickness for a compensation of the refractive index difference	121
A.4	Influence of the correction collar at the xy-cross section of the focal volume . .	122
A.5	FRET-efficiency histograms of the unspecifically labeled cold-shock protein A .	123
A.6	Fluorescence intensity measurement under pressure	124

1 Introduction

The first observation of single molecules has been already realized by Hirschfeld [27] in 1976, and the first single molecule fluorescence measurement was presented by Shera et al.[28] in 1990. Because single molecule fluorescence spectroscopy allows to overcome the average-limited view of ensemble methods, thus enabling the detailed observation of conformational heterogeneity and dynamics of biomolecules, fluorescence spectroscopy in the life sciences received a tremendous boost with the advent of single molecule techniques [24, 25, 26] in the last two decades.

FRET under single molecule concentration (smFRET) is one of these powerful single molecule fluorescence methods. Unlike most optical methods, FRET provides quantitative information on intermolecular distances by measuring the efficiency of a distance dependent energy transfer between two fluorophores, that are attached to the investigated biomolecule at two specific positions. The molecule is diffusing into a small focal volume of the order of a femtoliter and only the specific FRET-efficiency of one single fluorescently labeled biomolecule is measured at the same time. Even if the molecule's FRET-efficiency belongs to the minority population, it is recorded and added to a FRET-histogram, unlike in an ensemble method, where many molecules are investigated at the same time and the information of this molecule would be lost, if its FRET-efficiency is rare. That is why smFRET is perfectly suitable for the study of the unfolded state of proteins, because it allows for a separated investigation of the unfolded protein [29], even if its population is very small compared to the folded one. Furthermore, smFRET provides quantitative information on intermolecular distances and can not only be used to investigate the unfolding equilibrium and the thermodynamic parameters of a protein, but also to probe the dimension of the unfolded chain. The size and size-changes of a protein can thereby be measured within a range of 1-10 nm.

A first FRET measurement confirming Förster's theory from 1948 [66] has been done by Stryer and Haugland in 1967 [31], attaching dansyl and naphtyl groups to the termini of polyproline peptides and measuring the FRET efficiency as a function of the length of the poly peptide. The idea of a spectroscopic ruler was born. On the other hand, advances in fluorescence microscopy were leading to the advent of the single molecule detection (SMD) in the 1990s. First immobilized molecules were imaged with near field microscopy (SNOM) [32, 34, 33], confocal microscopy [35, 36] and total internal reflection fluorescence (TIRF) [37, 38, 39, 40] until SMD of diffusing molecules could be demonstrated [41, 42]. Ha et al. first succeeded in measuring smFRET [43] of biological molecules by acquiring the fluorescence spectrum using SNOM. Following this pioneering work, numerous smFRET experiments have

been reported, e.g. investigating conformational dynamics of proteins in catalytic reactions [44], ligand induced conformational change [45] and protein folding [46]. Finally, smFRET experiments of freely diffusing molecules could be realized, which are free from influences by the glass surface [47, 48, 49, 50]. In 2000, smFRET measurements even in a live cell were realized [51]. SmFRET is established in a wide range of research. In particular, protein unfolding by temperature and chemical denaturants has been elucidated by smFRET [77, 30, 29]. Yet, smFRET at high pressure to follow pressure unfolding of proteins has not been demonstrated to date.

On the other hand, applying pressure to unravel the energy-landscape of biomolecules also came into the focus of researchers recently [52, 53, 54]. Not only that more than a half ($\approx 62\%$) of the total volume of biosphere is at a depth in excess of 1000 m (i.e. submitted to a pressure higher than 100 bar), that there are organisms that even thrive under those extreme conditions [3, 4], that high pressure has also been broadly used by industry and biotechnology [5, 6, 7], for example for food extraction and preservation, first of all high pressure perturbation changes the free gibbs energy merely through volume work (mechanical energy) [1]. Whereas for temperature, the conjugate variable is entropy, a vitally important but less intuitive quantity, pressure has the advantage that its conjugate is volume, something readily and directly related to the structure [10]. The effects of pressure are more amenable to interpretation than those of temperature: A change of temperature changes the volume and the energy content so the internal interactions of the protein are changed in a way that are not easily foreseen, while pressure affects internal interactions exclusively by the changes in the distances (volumes) of the components [9].

The investigation of proteins under high pressure all started with the pioneering work of the physicist Percy W. Bridgmann in 1914, where he first observed a coagulation of a white egg subjected to hydrostatic pressure [11]. Then for a long period, the sample environment was an overwhelming problem for crystallographic methods and publications were rare until pressure studies of biomolecules fully emerged in the 1960s and 1970s [2]. In 1973, Thomanek reported X-ray crystallographic data collected from a crystal of a sperm whale myoglobin pressurized to 2500 bar in liquid isopentane. Because of the isopentane, the crystal survived the pressurization, diffracted well, and a number of Bragg reflections had intensities that differed from crystals at atmospheric pressure [12]. In the 1980s Kundrot & Richards developed a beryllium specimen chamber for X-ray crystallography and solved the structure of hen egg white lysozyme at up to 1000 bar [14, 15]. Recently, also NMR-spectropists began to study small proteins under pressure such as bovine pancreatic trypsin inhibitor, which has been the first high pressure NMR structure solved [16]. Histidine containing protein [17], ubiquitin [18]

and the GTPase [19] and others [20, 21, 22, 23] followed.

First ensemble fluorescence measurements under high pressure, using a “high pressure bomb” were described by Weber et al. [55]. With an optical path of 5 mm and a window thickness of more than 1 mm, the high pressure bomb is not suitable for single molecule methods, where high numerical aperture (NA)-objectives with small working distances ($< 500 \mu\text{m}$) are needed.

For the study of biomolecules under pressure, several techniques like fluorescence, IR spectra, x-ray scattering and NMR are used, allowing to compare the results and choose the best method for the specific problem, that is investigated. Single molecule fluorescence spectroscopy under pressure, especially FRET, has the potential to contribute significantly to a deeper understanding of biological systems.

Lately high pressure fluorescence measurements at single molecule concentration with two photon excitation have been realized with the use of a fused silica capillary as the pressure cell by Gratton et al [56, 60]. It allows for using high NA-objectives for the measurement because of its small wall thickness. Despite of its thin sidewalls, a cylindrical capillary (od= $300 \mu\text{m}$, id= $50 \mu\text{m}$) can stand pressures of up to 4 kbar [56]. However, the cylindrical shape used by Gratton et al. leads to optical aberrations of the focused laser beam making the cylindrical capillary inappropriate for single molecule fluorescence methods with single photon excitation like smFRET.

Here, an approach is presented, where square bore instead of cylindrical fused silica capillaries are used for better imaging conditions and to realize smFRET under high pressure to investigate pressure induced protein unfolding.

Square capillaries lead to less aberrations, compared to cylindrical capillaries. Unfortunately, standard microscope objectives are optimized for borosilicate coverslips, with a refractive index different to that of fused silica. We aimed to solve this issue with an optical new arrangement, placing the capillary on top of a silica coverslip of appropriate thickness with an index matching gel in between. The disadvantage of square fused silica capillaries with the same dimensions is the reduced pressure stability of only 2 kbar.

In order to evaluate the optics of the capillary, scans of the focal volume, fluorescence correlation benchmarks, and FRET experiments in the square fused silica capillary and in the new arrangement are compared with those performed on a standard coverslip, which serve as a reference for the experimental setup. Then, a pressure dependent fluorescence lifetime measurement, to verify the amount of pressure, and smFRET measurements under pressure of a DNA preference sample, to exclude pressure artifacts, have been performed. Finally, the two domain protein SlyD, the model two-state folder CspA, and the intrinsically unfolded

yeast-frataxin were unfolded with pressure and their unfolding transitions were followed with smFRET and compared to denaturant and temperature unfolding in order to gain insight into the unfolding mechanism by pressure.

2 Fundamentals

2.1 Photoluminescence

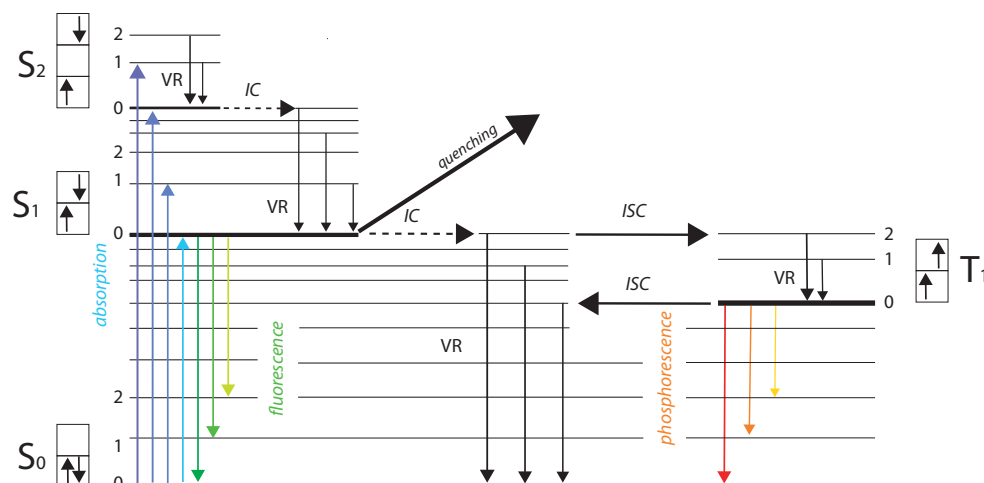


Figure 2.1: Jablonski diagram

Photoluminescence is the emission of light upon an absorption of photons. Hence at first, an electron of an orbital fluorescence molecule has to be excited from the ground state to a singlet state by absorbing a photon. Then the excited fluorophore can relax by various competing pathways to its ground state. If the the excited molecule directly relaxes to its ground state, by emitting a photon, this emission is called fluorescence. If it undergoes an intersystem crossing (ISC) into a triplet state at first, the emission of a photon, by relaxing to its ground state, is called phosphorescence. Another possibility is that the electron relaxes non radiatively by internal conversion (IC) and vibrational relaxation (VR) from a singlet or the triplet state to the ground state by transforming its electronic energy into heat, which is then dissipated to the solvent, by an intreraction with another so called “quencher” molecule or by a chemical reaction. The transitions between these energy levels are shown in the Jablonski diagram in figure 2.1.

2.2 The transition rates

According to the Franck-Condon principle, absorption is an instantaneous event (10^{-15} s) [57]. The principle states that electronic transitions are fast compared with nuclear motions, that vibrational levels are favored when they correspond to a minimal change in the nuclear

2.2 The transition rates

coordinates. According to Kasha's rule, the electron relaxes to the ground state only after a nonradiative relaxation to the vibrational ground state of the excited state. Energy is lost because of the Frank-Condon principle and due to relaxation effects of the polar solution. This leads to a spectral red shift between the absorption and the emission spectra, the so called Stokes shift. It is responsible for the success of fluorescence microscopy, allowing to separate the emitted light from the excitation light by its wavelength.

Table 1: Transition rates

	absorption	IC	VR	ISC	fluorescence	phosphorescence
transition rate (s^{-1})	$\sim 10^{15}$	$\sim 10^{12}$	$\sim 10^{11}$	$\sim 10^7$	$\sim 10^8$	$\sim 10^2$

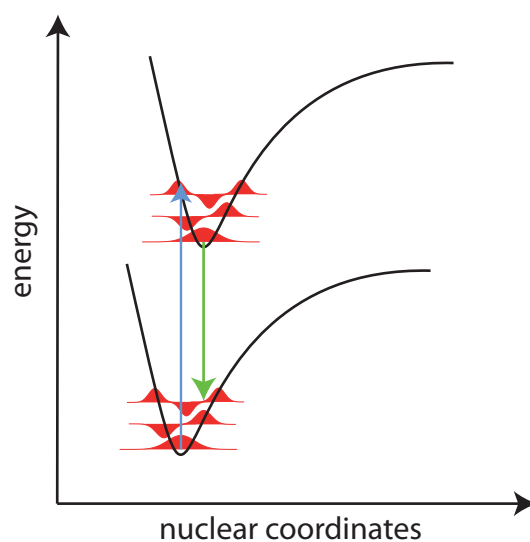


Figure 2.2: Franck-Condon principle

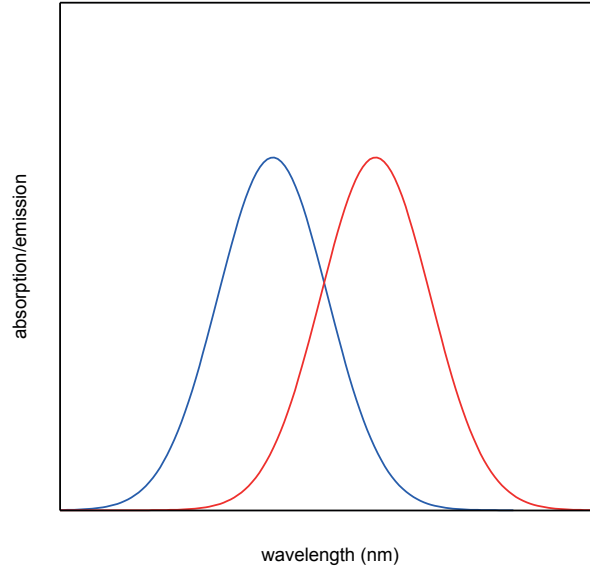


Figure 2.3: Absorption (blue) and emission (red) spectra of a fluorophore

The nonradiative rates of the internal conversion k_{ic} , the intersystem crossing k_{isc} and the quenching rate k_q are much lower than the absorption rate..

$$k_{nr} = k_{ic} + k_{isc} + k_q \quad (2.1)$$

With the fluorescence rate k_F they determine the quantum efficiency Q , which is a quantitative parameter of a fluorophore. It is crucial for the signal to noise ratio because it is the ratio of the emitted k_e and absorbed photons k_a during a measurement:

$$Q = \frac{k_e}{k_a} = \frac{k_F}{k_{nr} + k_F} \quad (2.2)$$

The inverse of the fluorescence rate is called natural fluorescence lifetime τ_n . It is also a characteristic parameter of a fluorophore, stands for the time the fluorophore stays in the excited state without any influence of nonradiative transitions and is typically not directly experimentally accessible:

$$\tau_n = \frac{1}{k_F} \quad (2.3)$$

In contrast the fluorescence lifetime that can be directly measured considers nonradiative influences:

$$\tau = \frac{1}{k_{nr} + k_F} \quad (2.4)$$

2.3 The triplet state

As mentioned above, a fluorescence molecule can undergo an intersystem crossing (ISC) from a singlet into a triplet state. The spin of an excited electron is reversed which is a spin forbidden process. Therefore the intersystem crossing is very inefficient leading to a rather low intersystem crossing rate. The phosphorescence rate is even slower because of the selection rule for photon emission. In certain materials this can lead to an emission even several hours after the original excitation. Because the intersystem crossing rate is that low, the triplet state can be saturated with less power than the singlet state. Therefore it is used for saturation measurements to quantify the excitation quality by measuring the apparent intersystem crossing rate k_{isc}^{app} [58]. It is the rate of the population of the triplet state and is expressed by the absorption rate k_{abs} , the fluorescence rate k_F and the intersystem crossing rate k_{isc} as:

$$k_{isc}^{app} = \frac{k_{abs}}{k_{abs} + k_F} k_{isc} \quad (2.5)$$

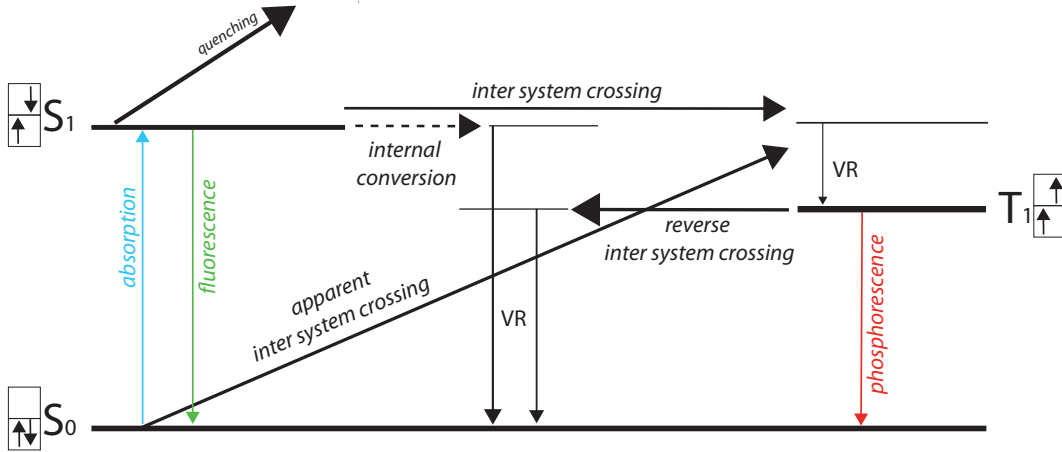


Figure 2.4: Saturation of the triplet state

The triplet rate k_T is the sum of the apparent intersystem crossing rate k_{isc}^{app} and the reverse intersystem crossing rate k_{risc} , which is the depopulation rate of the triplet state:

$$k_T = k_{isc}^{app} + k_{risc} \quad (2.6)$$

The triplet time τ_T is the inverse of this rate:

$$\tau_T = \frac{1}{k_T} = \frac{1}{k_{isc}^{app} + k_{risc}} \quad (2.7)$$

The triplet part T is the part of all excited molecules, that are in the triplet state:

$$\frac{T}{1 - T} = \frac{k_{isc}^{app}}{k_{risc}} \quad (2.8)$$

So the apparent intersystem crossing rate can be directly measured via the triplet time τ_T and the triplet part T resulting of a FCS measurement (see section 2.11):

$$k_{isc}^{app} = \frac{T}{\tau_T} \quad (2.9)$$

The triplet state is by definition saturated when:

$$k_{isc}^{app} = \frac{k_{isc}}{2} \quad (2.10)$$

Due to this, the triplet saturation power P_{sat} can be calculated from a fit of the apparent intersystem crossing rate measured at different laser powers P :

$$k_{isc}^{app}(P) = \frac{k_{isc}}{1 + \frac{P_{sat}}{P}} \quad (2.11)$$

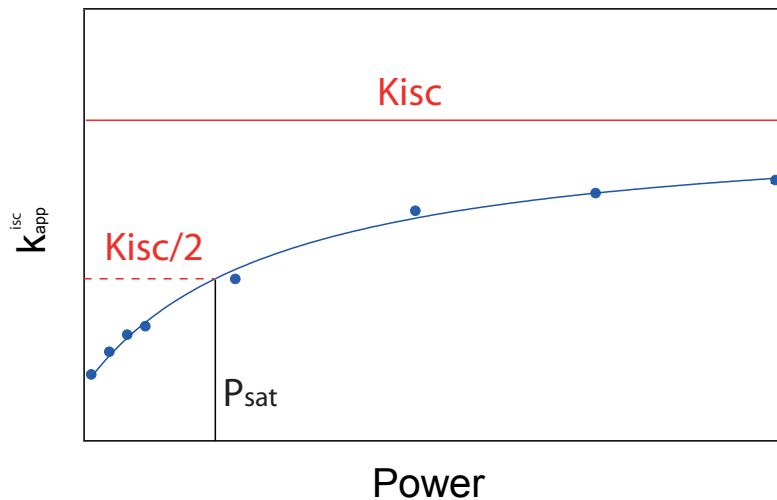


Figure 2.5: Apparent intersystem crossing rate

2.4 Fluorescence saturation

Also the fluorescence rate k_F can be saturated. Because the fluorescence rate k_F is higher than the intersystem crossing rate k_{isc} (see table 1), the singlet state needs more power to be saturated than the triplet state. The saturation power P_{sat} can be calculated from a fit of the fluorescence rate measured at different laser powers P :

$$k_F = k_{F,max} \frac{1}{1 + \frac{P_{sat}}{P}} \quad (2.12)$$

The higher laser power needed, is a disadvantage of the fluorescence intensity saturation measurement as a benchmark of the excitation quality. Especially the background intensity would tamper the measurement dramatically.

2.5 Fluorescence quenching and bleaching

Every process that reduces the fluorescence intensity is called quenching. To quench a fluorophore, the quencher can prevent the excitation by forming a non fluorescent ground-state complex. This is called static quenching. If the fluorescence is excited but the fluorescence emission is avoided by a quencher, it is called dynamic quenching. During its fluorescence lifetime, the excited fluorophore either diffusively collides with a quencher or is already in molecular contact or at close range to a quencher, which causes the fluorophore to return to

the ground state without emitting a photon. FRET (see section 2.8) can also be regarded as a quenching process.

Fluorescence bleaching is the irreversible destruction of a fluorophore. Typically after emitting 10^6 fluorescence photons, the fluorophore undergoes structural changes by photo-oxidation or photoionisation, which leads to a highly reactive non fluorescent radical ionic state. Consequently high excitation intensities should be avoided to reduce photo bleaching.

2.6 Fluorescence measurement

A wide range of problems in chemistry and biology can be studied with fluorescence spectroscopy. Almost every molecular process, including the interaction of solvent molecules with fluorophores, rotational diffusion of biomolecules, distances between sites on biomolecules, conformational changes and binding interactions, can be followed [57]. The advantage of fluorescence is the selectivity of the microscope mode. Whereas for example phase contrast microscopy uses only light that has been retarded in phase by passage through the object, fluorescence imaging uses only light from fluorescent molecules that has been shifted in frequency [64]. Thereby disturbing information like background light can be filtered out and only the molecule of interest delivers the information. On the other hand, except for an investigation of the fluorescence molecule itself, for example a fluorophore like the *green fluorescent protein*, it is an indirect measurement. The molecule of interest, for example a protein or a DNA-chain, has to be labeled with fluorescent molecules, called fluorophores, and the information about the molecule has to be measured indirectly by measuring the fluorescence of the fluorophore. This has to be considered for the interpretation of every experiment.

The investigation can be done by the fluorescence absorption or the emission of light with a wavelength ranging from infrared (μm), to the visible range (900-400 nm) and down to UV (10 nm), only depending on the fluorophores used. In the following section the fluorescence measurement methods, applied in this thesis, will be presented.

2.7 Single molecule fluorescence

Observation of single molecules represents the highest obtainable sensitivity and is now being performed in many laboratories. Biological molecules are inherently heterogeneous; they can be in different folded states, different configurations or stages during an enzymatic process. For single molecule fluorescence (SMF) no synchronization is needed and rare intermediates or subpopulations, which would otherwise be hidden beneath more populous species, can be measured. The ergodic principle says, that the average of a process parameter over time and

2.8 Fluorescence resonance energy transfer (FRET)

the average over the statistical ensemble are the same, which additionally enables us to get the same statistical results from a single molecule measurement over a longer time period as we get from an ensemble measurement of several molecules simultaneously. Hence the only disadvantage of SMF, compared to an ensemble measurement, is the realization that is more difficult and the measurement is typically more time consuming. One possibility is the immobilization of single molecules on a surface, but surface interaction may interfere with the molecule's function. To realize SMF of freely diffusing molecules, it has to be considered that billions of solvent molecules are hampering the detection. Accordingly, highly diluted fluorescently labeled sample solutions are combined with a small focal volume [65]. Free molecules are diffusing by Brownian motion through a focal volume of down to 10^{-15} l. This confines the speed of a dynamic process that can be followed, because if it takes more time than the residence time of the molecule in the focal volume, the process becomes unmeasurable. The measurement variables can be: the absorption or emission spectra of the fluorophore, the fluorescence-lifetime,-anisotropy,-intensity, the diffusion time or the mean number of molecules in the focal volume. Also the triplet state of the fluorophore can be investigated by the triplet fraction and the triplet time. If the molecule is labeled with two or more fluorophores for a FRET-measurement, the FRET-efficiency becomes the measurement variable.

2.8 Fluorescence resonance energy transfer (FRET)

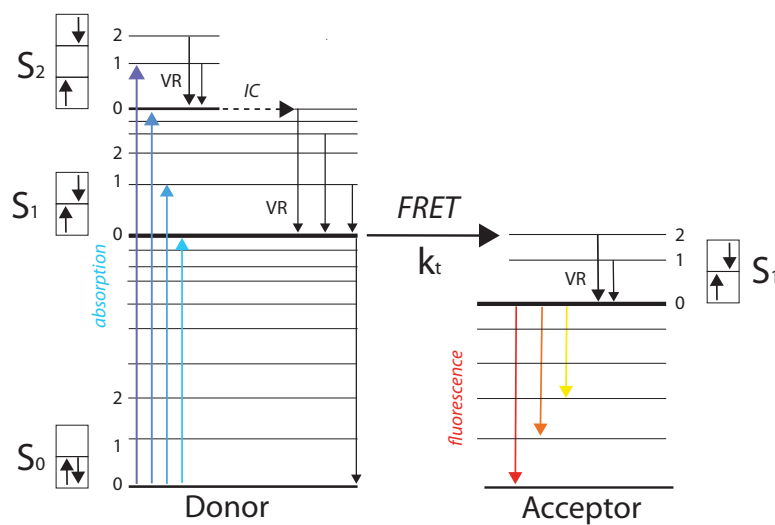


Figure 2.6: Jablonski diagram of the fluorescence resonance energy transfer

FRET is a nonradiative energy transfer from one fluorophore (donor) to another fluorophore (acceptor). The energy of a donor in its excited state is transferred to an acceptor in its ground state via dipole-dipole non-radiative resonant interaction. Thereby the donor relaxes nonradiative to its ground state and the acceptor will be excited to its first excited state which then will be able to relax by emitting a photon.

The quantum mechanical treatment, first given by Theodore Förster [66] provides the transfer rate k_t of this energy transfer, which depends on the dipole orientation of the two fluorophores to each other, i.e. the orientation factor k^2 , the spectral overlap integral $J(\lambda)$ of the two fluorophores, the fluorescence lifetime of the donor fluorophore in absence of the acceptor fluorophore, the refractive index of the surrounding medium n and mainly it depends to the sixth power on the distance r between the donor and the acceptor, which is the most common reason FRET is applied, as follows:

$$k_t = \frac{1}{\tau_{Donor}} \frac{9000(\ln 10)k^2 Q_{donor}}{128\pi^5 N_A n^4} J(\lambda) \frac{1}{r^6} \quad (2.13)$$

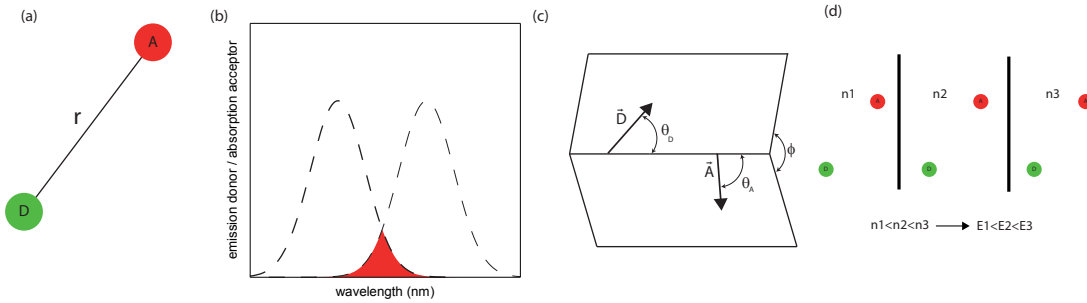


Figure 2.7: Important influences on the transfer efficiency: (a) distance, (b) overlap integral and (c) dipole orientation of the two fluorophores as well as (d) the refractive index of the medium

Figure 2.7 symbolizes the important influences on the transfer rate: the distance between the fluorophores, the overlap integral of the emission spectrum of the donor fluorophore and the absorption spectrum of the acceptor fluorophore and the dipole orientation of the dipoles of the two fluorophores, as well as the refractive index of the medium.

The spectral overlap integral $J(\lambda)$ is defined as the overlap integral of the emission spectrum of the donor fluorophore $F_D(\lambda)$ and the absorption spectrum $\varepsilon_A(\lambda)$ of the acceptor fluorophore:

$$J(\lambda) = \int_0^\infty F_D(\lambda) \varepsilon_A(\lambda) \lambda^4 d\lambda \quad (2.14)$$

The dipole orientation factor is defined as:

$$k^2 = (\sin\theta_D \sin\theta_A \cos\phi - 2\cos\theta_D \cos\theta_A) \cos^2\phi \quad (2.15)$$

The angles θ_D, θ_A and ϕ are shown in figure 2.7 where \vec{D} and \vec{A} are the dipole moments of the fluorophores. The rate k_t depends on the orientation of the two fluorophores to each other because the energy is transferred through a nonradiative dipole–dipole coupling. If the fluorophores are free in motion as always in our measurements we use the mean value of $\frac{2}{3}$ for the orientation factor.

The beauty of Förster's theory is that all the quantities depending on the used pair of fluorophores and the surrounding medium can be easily determined (see table 2) and a Förster radius can be introduced :

$$R_0^6 = \frac{9000(\ln 10)k^2 Q_{donor}}{128\pi^5 N_A n^4} J(\lambda) \quad (2.16)$$

Then the transfer rate becomes:

$$k_t = \frac{1}{\tau_{Donor}} \frac{R_0^6}{r^6} \quad (2.17)$$

So the transfer rate at a distance of R_0 equals the fluorescence and the nonradiative rate of the donor-fluorophore:

$$k_t(r = R_0) = \frac{1}{\tau_{Donor}} \frac{R_0^6}{R_0^6} = \frac{1}{\tau_{donor}} = k_F + k_{nr} \quad (2.18)$$

A FRET-efficiency E was introduced because it is experimentally accessible (see section 2.9) and intuitive. It is defined as the ratio of the transfer rate k_t and the sum of the transfer rate k_t , the fluorescence rate k_F and the nonradiative rate k_{nr} of the donor fluorophore:

$$E = \frac{k_t}{k_t + k_F + k_{nr}} = \frac{k_t}{k_t + \frac{1}{\tau_{Donor}}} = \frac{\frac{1}{\tau_{Donor}} \frac{R_0^6}{r^6}}{\frac{1}{\tau_{Donor}} \frac{R_0^6}{r^6} + \frac{1}{\tau_{Donor}}} = \frac{R_0^6}{R_0^6 + r^6} \quad (2.19)$$

and with the introduced förster radius only depends on R_0 and r .

The FRET-efficiency E for a distance of $r = R_0$ of the fluorophores is:

$$E(R_0) = \frac{R_0^6}{R_0^6 + R_0^6} = 0.5 \quad (2.20)$$

Therefore the Förster distance R_0 is the distance where the efficiency of the energy transfer E is 50%. With R_0 typically in the single digit nanometre range (see table 2), changes of distances in the nanometre regimes can be measured. This is the reason for the success of FRET. The precise measurement of the transfer rate permits to make a quantitative statement about statistical distances, distance changes, dynamics and molecular interactions.

Table 2: R_0 values in Angstrom (\AA) for the fluorophore pairs used in this work. ($k^2 = \frac{2}{3}$, $n = 1.33$)

donor/acceptor	Alexa Fluor 594	Alexa Fluo 647	Atto 647N
Alexa 488	60	56	52

To enable FRET, a protein, DNA-strand or another biomolecule of interest has to be labeled at two positions with two different fluorophores. Experimentally the FRET-efficiency is accessible in two ways. Either the fluorescence lifetimes of the donor in absence τ_D and in presence of the acceptor τ_{DA} :

$$E = 1 - \frac{\tau_{DA}}{\tau_D} \quad (2.21)$$

or the fluorescence intensity of the acceptor and the donor fluorophores have to be measured:

$$E = \frac{I_A}{I_A + I_D} \quad (2.22)$$

In the latter case, the fluorescence of these two fluorophores will be separated by wavelength into two channels by filters. One is the donor channel for the fluorescence of the donor-fluorophore, the other one is the acceptor channel for the fluorescence of the acceptor-fluorophore. It should be mentioned here that equation 2.22 holds only for an ideal experiment and otherwise, correction is needed (see section 3.5.3).

2.9 Single molecule FRET

In an ensemble measurement (left side figure 2.8) many molecules are observed at the same time, so there is a mean donor-channel-intensity (blue) and a mean acceptor-channel-intensity (red). If we calculate the FRET efficiency by equation 2.22, only a mean fret-efficiency can be obtained.

In contrast, in a single molecule FRET-measurement (right side figure 2.8) a time trace of the donor and acceptor channel delivers many fluorescence intensity bursts of fluorescence molecules diffusing into a small focal volume. Of every burst (or every time-binned intensity)

with a sum threshold of the donor and acceptor channel, the fret efficiency of this burst is calculated by eq. 2.22. If there are, for example, two different populations in the sample (blue and red in figure 2.8) with a high FRET-efficiency and a lower FRET-efficiency, a histogram of the fret efficiencies delivers much more information than an ensemble measurement. The two different populations can be investigated separately: Their different FRET-efficiencies (figure 2.8c) and their fractions (figure 2.8d) can be calculated .

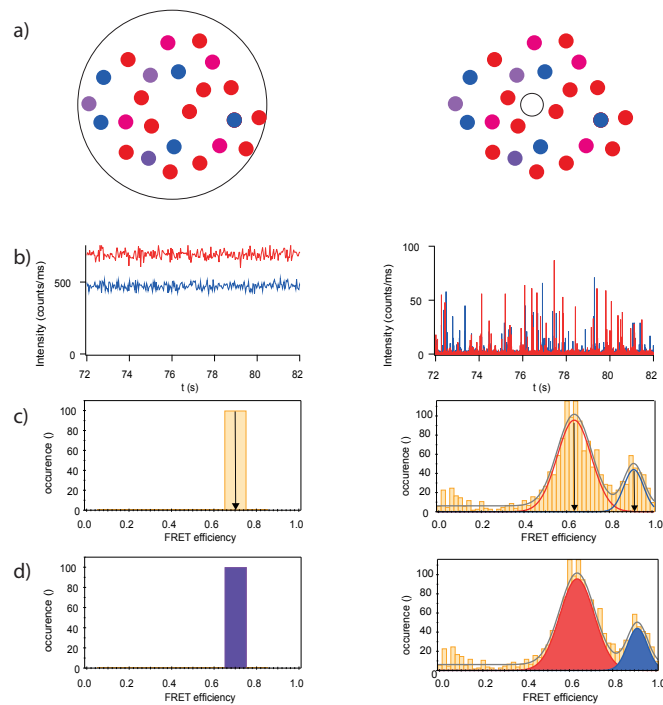


Figure 2.8: Ensemble FRET (left) and single molecule FRET(right): (a) detection volume (black) with high (red)- and low (blue)-FRET-molecules (b) fluorescence intensity in the donor (blue) and the acceptor (red) channel (c) FRET efficiency of the populations in a FRET-histogram (d) fractions of the populations in a FRET-histogram

If the biomolecule is shot-gun labeled, i.e. unspecifically labeled, a lot of molecules are only labeled with two acceptor-or donor-fluorophores. The acceptor-only molecules are not tampering the FRET-histograms since they are simply not excited, but donor-only molecules are leading to a donor-only-peak at a very low FRET-efficiency in the FRET-histogram (see figure 2.8 or figure 4.10). Therefor single molecule FRET offers the possibility of selecting bursts (or bins) that are counted in a histogram and excluding others. By pulsed overlayed excitation (POE) it is thereby possible to use an acceptor-threshold to exclude donor-only labeled molecules. If molecules with a low FRET efficiency are investigated, POE can help to avoid a tampering of the FRET-histogram. Since this was not the case in the presented work

and POE also leads to a bleaching of the acceptor-fluorophore, POE has not been used in the thesis.

2.10 Fluorescence and pressure

The changes in spectra and intensity of fluorescent molecules with changes in pressure are really small in the accessible pressure range of up to 2 kbar here[59]. The fluorescence lifetime in contrast depends much stronger on pressure. This pressure dependence can be explained with a simple model [56]. The fluorescence lifetime depends on the nonradiative rate and the fluorescence rate:

$$\tau(p) = \frac{1}{k_{nr}(p) + k_F(p)} \quad (2.23)$$

Good fluorophores like Alexa 488 have a very high quantum yield ($Q > 0,9$). This allows the approximation:

$$Q \approx 1; \quad k_{nr}(p) \ll k_F(p) \quad (2.24)$$

Thus, the fluorescence lifetime is dominated by the fluorescence rate:

$$\tau(p) = \tau_n(p) = \frac{1}{k_F(p)} \quad (2.25)$$

The Strickler-Berg equation states:

$$k_F = \frac{1}{\tau_n} = 2.88 \cdot 10^{-9} n^2 \frac{\int I(\gamma) d\gamma}{\int I(\gamma) \gamma^{-3} d\gamma} \int \frac{\varepsilon(\gamma)}{\gamma} d\gamma \quad (2.26)$$

Here, n is the refractive index, I the fluorescence emission, ε the molar extinction coefficient connected with the first (lowest) electronic transition and γ the wave number.

The fluorescence rate is in the simplest model only affected by the pressure induced change in the refractive index of the surrounding medium:

$$k_F(p) = \frac{n^2(p)}{n^2(1bar)} k_F(1bar) = \frac{n^2(p)}{n^2(1bar)} \frac{1}{\tau(1bar)} \quad (2.27)$$

The pressure dependence of the refractive index of water shown in figure 2.9 was determined by K.Vedam et al. [75].

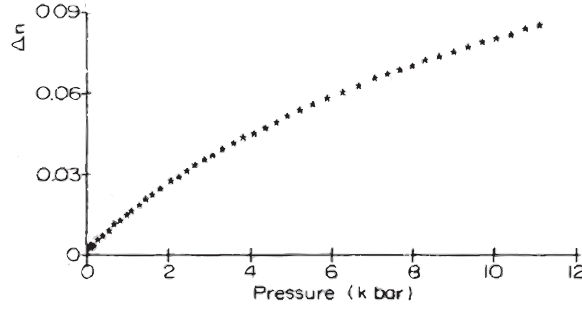


Figure 2.9: Variation of the refractive index of water at $\lambda = 546.1$ nm [75]

Knowing the pressure dependence of the refractive index, the pressure dependence of the fluorescent lifetime can be calculated according to:

$$\tau(p) = \frac{n^2(1\text{bar})}{n^2(p)} \tau(1\text{bar}) \quad (2.28)$$

Hence for a pressure of 2 kbar and a measurement in water a reduction of the fluorescence lifetime of 4 % is expected.

2.11 FCS measurement

The biological function of a biological molecule depends not only on their structure, but also their mobility and dynamic properties, which are also strongly influenced by their environment. Fluorescence correlation spectroscopy (FCS) allows inherent averaging over a large number of single molecule passages through the measurement volume and thus is ideally suited to assess all type of fluctuations [65]. Here FCS is motivated only by determining triplet dynamics and the mean number of fluorescent molecules in the focal volume.

Theoretical basics of FCS were described in the 1970's by Magde, Elson and Webb [68, 69]. The realization in the 1990's was enabled by highly efficient detectors, stable lasers, confocal optics and more efficient dyes [70].

FCS is based on the measurement of signal fluctuations of diffusing fluorescent single molecules through the illuminated focal volume. The fluctuations of the signal $\delta I(t)$ can be described by the signal intensity $I(t)$ and its mean value $\langle I(t) \rangle$:

$$\delta I(t) = I(t) - \langle I(t) \rangle \quad (2.29)$$

The mean fluctuation equals zero:

$$\langle \delta I(t) \rangle = 0 \quad (2.30)$$

From these fluctuations the autocorrelation function can be calculated. In principle the autocorrelation function is the normalized self similarity of the signal after a lag time τ :

$$G(t, \tau) := \frac{\langle I(t)I(t + \tau) \rangle}{\langle I(t) \rangle^2} \quad (2.31)$$

This can be calculated descriptively by the convolution of the signal with itself after a lag time (see figure 2.10):

$$\langle I(t)I(t + \tau) \rangle = \frac{1}{T} \int_0^t dt I(t)I(t + \tau) \quad (2.32)$$

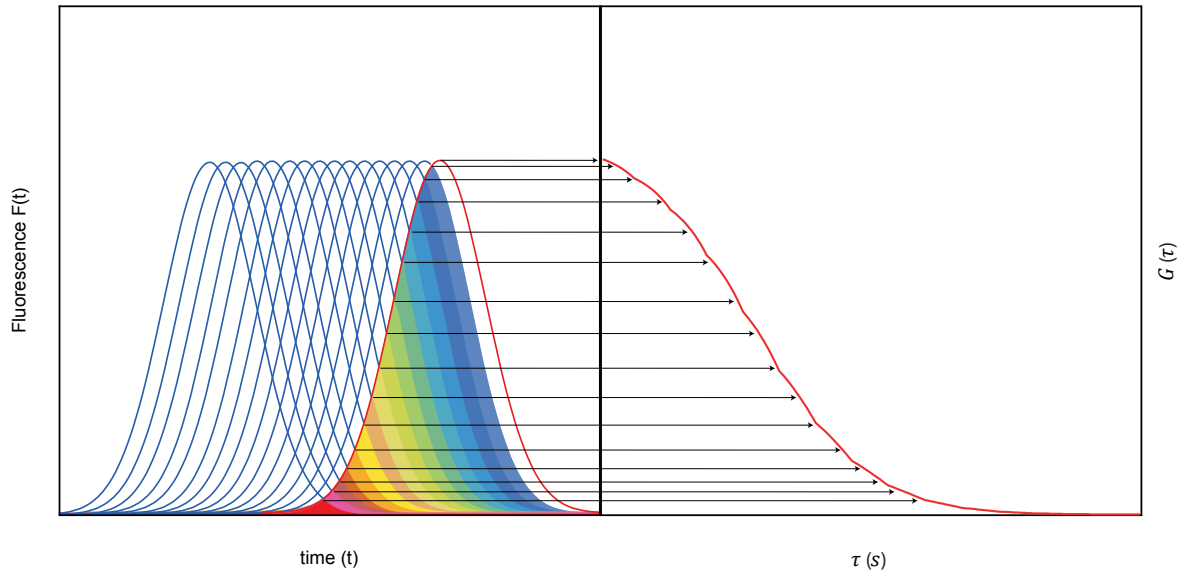


Figure 2.10: Overlap integral

To calculate the autocorrelation from the signal fluctuations $I(t) = \delta I(t) + \langle I(t) \rangle$ has to be substituted in equation 2.31:

$$\begin{aligned} G(t, \tau) &= \frac{\langle (\delta I(t) + \langle I(t) \rangle)(\delta I(t + \tau) + \langle I(t + \tau) \rangle) \rangle}{\langle I(t) \rangle^2} = \\ &= \frac{\langle \delta I(t)\delta I(t + \tau) + \langle I(t) \rangle \delta I(t + \tau) + \delta I(t) \langle I(t + \tau) \rangle + \langle I(t) \rangle \langle I(t + \tau) \rangle \rangle}{\langle I(t) \rangle^2} = \end{aligned}$$

$$\frac{\langle \delta I(t) \delta I(t+\tau) \rangle + \langle \langle I(t) \rangle \delta I(t+\tau) \rangle + \langle \delta I(t) \langle I(t+\tau) \rangle \rangle + \langle \langle I(t) \rangle \langle I(t+\tau) \rangle \rangle}{\langle I(t) \rangle^2} =$$

$$\frac{\langle \delta I(t) \delta I(t+\tau) \rangle + \langle I(t) \rangle \langle \delta I(t+\tau) \rangle + \langle \delta I(t) \rangle \langle I(t+\tau) \rangle + \langle I(t) \rangle \langle I(t+\tau) \rangle}{\langle I(t) \rangle^2} =$$

and, with equation 2.30 and

$$\langle I(t) \rangle = \langle I(t+\tau) \rangle, \quad (2.33)$$

the autocorrelation described by the signal fluctuation becomes:

$$G(t, \tau) = \frac{\langle \delta I(t) \delta I(t+\tau) \rangle}{\langle I(t) \rangle^2} + 1 \quad (2.34)$$

The total autocorrelation function is calculated from the fluctuation originating from diffusing molecules and from photophysical processes, e.g. the triplet state:

$$G_{total} = G_{diff} \cdot \chi_{triplet} + 1 \quad (2.35)$$

The diffusion autocorrelation at a time $t = 0$ is given by:

$$G_{diff}(0, \tau) = \frac{\langle \delta I(0) \delta I(\tau) \rangle}{\langle I(0) \rangle^2} \quad (2.36)$$

The intensity fluctuation $\delta I(t)$ is calculated by the convolution of the concentration fluctuation $\delta C(r, t)$ with the molecular detection efficiency $MDE(r)$ and the molecular emission yield η :

$$\delta I(t) = \eta \int dr MDE(r) \delta C(r, t) \quad (2.37)$$

the signal intensity $I(t)$ is calculated by the convolution of the concentration $C(r, t)$ with the molecular detection efficiency $MDE(r)$ and the molecular emission yield η :

$$I(t) = \eta \int dr MDE(r) C(r, t) \quad (2.38)$$

and with the simplification that the fluctuation of the molecular emission yield $\delta\eta$ equals zero:

$$\delta(\eta C) = C \delta\eta + \eta \delta C; \quad \delta\eta = 0 \quad (2.39)$$

the diffusion autocorrelation function can be written as:

$$G_{diff}(\tau) = \frac{\eta^2 \int \int dr dr' MDE(r, 0) MDE(r', \tau) \langle \delta C(r, 0) \delta C(r', \tau) \rangle}{\eta^2 \langle C \rangle^2 [\int dr MDE(r, 0)]^2} \quad (2.40)$$

Considering only particles that are freely diffusing in three dimensions with the diffusion coefficient D , the so-called number density autocorrelation term $\langle \delta C(r, 0) \delta C(r', \tau) \rangle$ can be calculated:

$$\langle \delta C(r, 0) \delta C(r', \tau) \rangle = \langle C \rangle \frac{1}{(4\pi D\tau)^{3/2}} \exp\left(-\frac{|r - r'|^2}{4D\tau}\right); \quad (2.41)$$

$$G_{diff}(\tau) = \frac{1}{\langle C \rangle (4\pi D\tau)^{-3/2}} \frac{\int \int dr dr' MDE(r, 0) MDE(r', \tau) \exp\left(-\frac{|r - r'|^2}{4D\tau}\right)}{[\int dr MDE(r, 0)]^2} \quad (2.42)$$

Using the following definition of the effective focal volume V_{eff} and the lateral diffusion time τ_D that a molecule stays in the focal volume:

$$V_{eff} = \frac{[\int dr MDE(r, 0)]^2}{\int dr dr' MDE(r, 0) MDE(r', \tau)} = \pi^{\frac{3}{2}} \cdot r_0^2 \cdot z_0; \quad \tau_D = \frac{r_0^2}{4D} \quad (2.43)$$

the diffusion correlation function is found as:

$$G_{diff}(\tau) = \frac{1}{V_{eff} \langle C \rangle} \frac{1}{\left(1 + \frac{\tau}{\tau_D}\right)} \frac{1}{\sqrt{1 + \left(\frac{r_0}{z_0}\right)^2 \frac{\tau}{\tau_D}}} \quad (2.44)$$

So from a signal measurement of $I(t)$ and a calculation of $G(t, \tau) := \frac{\langle I(t)I(t+\tau) \rangle}{\langle I(t) \rangle^2}$, the mean number of molecules in the focal volume $\langle N \rangle$ can be determined:

$$G_{diff}(0) = \frac{1}{V_{eff} \langle C \rangle} = \frac{1}{\langle N \rangle} \quad (2.45)$$

as well as the diffusion time τ_D by fitting the autocorrelation curve since:

$$G_{diff}(\tau_D) = \frac{1}{V_{eff} \langle C \rangle} \frac{1}{\left(1 + \frac{\tau_D}{\tau_D}\right)} \frac{1}{\sqrt{1 + \left(\frac{r_0}{z_0}\right)^2 \frac{\tau_D}{\tau_D}}} \approx \frac{G_{diff}(0)}{2} \quad (2.46)$$

If we also consider fluctuations originating from triplet blinking the total autocorrelation G_{total} becomes:

$$G_{total} = G_{diff} \cdot \chi_{triplet} + 1 \quad (2.47)$$

with a triplet term $\chi_{triplet}$ expressed with the triplet rate T and the triplet time τ_T :

$$\chi_{triplet} = 1 + \frac{T}{1-T} \exp\left(-\frac{\tau}{\tau_T}\right) \quad (2.48)$$

The total autocorrelation thus reads:

$$G_{total} = G_{diff} \cdot \chi_{triplet} + 1 = \left[1 + \frac{T}{1-T} \exp\left(-\frac{\tau}{\tau_T}\right)\right] \left[\frac{1}{N} \frac{1}{\left(1 + \frac{\tau}{\tau_D}\right)} \frac{1}{\sqrt{1 + \left(\frac{r_0}{z_z}\right)^2 \frac{\tau}{\tau_D}}}\right] + 1 \quad (2.49)$$

with the accessible measurement variables: N , τ_D , T and τ_T :

$$G(0) = \left(1 + \frac{T}{1-T}\right) \frac{1}{N} + 1; \quad G(\tau_D) \approx 1 + \frac{1}{2N}; \quad G(\tau_T) \approx \frac{\frac{T}{1-T} \frac{1}{N}}{e} + \frac{1}{N} + 1 \quad (2.50)$$

where the triplet fraction T is the fraction of all excited molecules that are in the triplet state, and τ_T stands for the time the molecule can't be excited. To summarize, from an intensity measurement $I(t)$, the autocorrelation function

$$G(t, \tau) := \frac{\langle I(t)I(t+\tau) \rangle}{\langle I(t) \rangle^2} \quad (2.51)$$

can be fitted by the model:

$$G(t, \tau) = \left[1 + \frac{T}{1-T} \exp\left(-\frac{\tau}{\tau_T}\right)\right] \left[\frac{1}{N} \frac{1}{\left(1 + \frac{\tau}{\tau_D}\right)} \frac{1}{\sqrt{1 + \left(\frac{r_0}{z_z}\right)^2 \frac{\tau}{\tau_D}}}\right] + 1 \quad (2.52)$$

to find the fit parameters N , τ_D , T and τ_T .

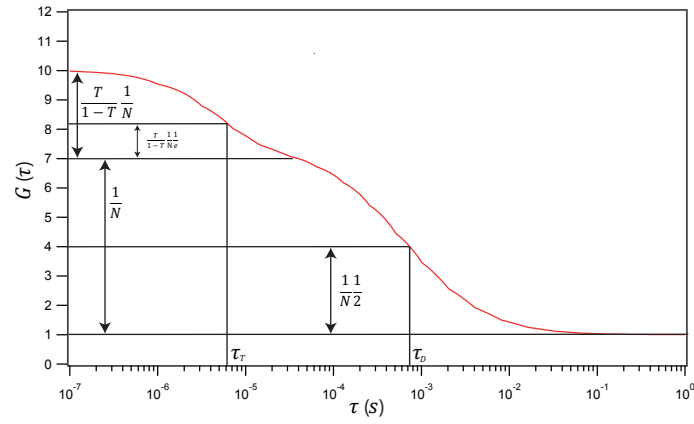


Figure 2.11: Autocorrelation curve

2.12 TCSPC lifetime measurement

As mentioned in section 2.2, the fluorescence lifetime is the time the fluorophore is in the excited state. It can be measured by measuring the time between the laser pulse and the arrival of the photon at the detector (see figure 2.12).

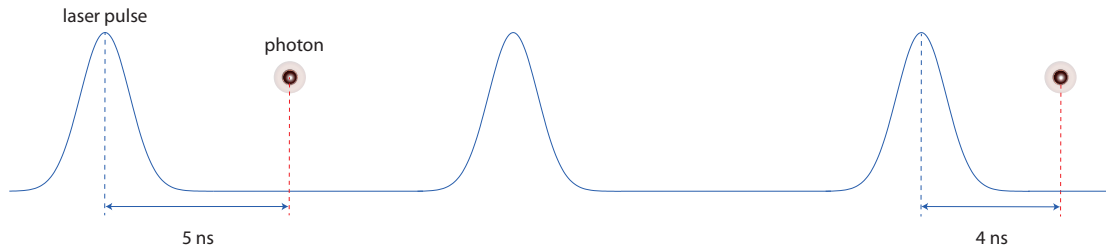


Figure 2.12: Measured time interval

Then the arrival times will be histogrammed and the fluorescence lifetime τ can be calculated from a fit function $n(t)$:

$$n(t) = n_0 \exp\left(-\frac{t - t_0}{\tau}\right) + B \quad (2.53)$$

where n_0 , t_0 , B and τ are the fit parameters. So the fluorescence lifetime is defined as the arrival-time where $\frac{1}{e}$ of the maximal number of photons of the fit function $n(t)$ have arrived at the detector.

2.13 Confocal microscopy

2.13.1 Confocal principle

In a confocal microscope the excitation and the detection pathway share their foci. Thus only fluorescence molecules from one same focal spot will be detected and excited. A defined and smaller focal volume, a higher resolution and a higher signal to noise ratio are the advantages of a confocal measurement.

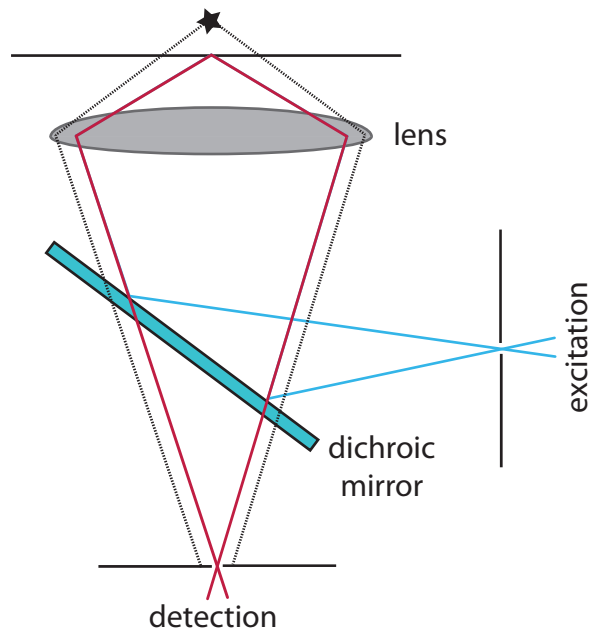


Figure 2.13: Excitation (blue) and detection (red) pathway in a confocal microscope

2.13.2 Excitation

The laser intensity distribution $I_{exc}(\vec{r}, z)$ is Gaussian in radial direction and Lorentzian along the z-axis [64]:

$$I_{exc}(\vec{r}, z) = \frac{w_0^2 I_0}{w_0^2 + \left(\frac{\lambda}{n\pi w_0}\right)^2 z^2} \exp\left(-\frac{\vec{r}^2}{w^2(z)}\right) \quad (2.54)$$

where $w_0 = \frac{\lambda}{n\pi \tan \delta}$ is the beam waist radius at $1/e^2$ intensity, I_0 is the power of the laser beam. \vec{r} is the radial coordinate and z is the distance from the focal plane along the optical axis. δ is the focusing angle of the laser beam in the sample at $1/e^2$ of the intensity, λ the laser wavelength and n is the refractive index of the sample.

2.13.3 Detection

The detection consists of two parts. First of all it is determined by the point spread function $PSF_{det}(\vec{r}, \vec{r}', z)$ of the microscope describing the image of a point source in terms of intensity distribution in the image plane [64]. The second influence is the pinhole $T(\vec{r})$. With the point spread function of the microscope the detection is defined by the collection efficiency:

$$CEF(\vec{r}', z) = \frac{1}{\Delta} \int T(\vec{r}) PSF_{det}(\vec{r}, \vec{r}', z) \quad (2.55)$$

Δ is a factor to normalize the function.

2.13.4 Molecular detection efficiency

The relative intensity of fluorescence from a molecule under real illumination is determined by the molecular detection efficiency $MDE(x, y, z)$. It is the product of their point spread functions, more precisely, the collection efficiency function and the laser intensity distribution, because the detection and the excitation pathways are confocal

$$MDE = I_{exc} \cdot CEF \quad (2.56)$$

It can be approximated by a quasi-cylindrical Gaussian profile:

$$MDE(x, y, z) \approx I_0 e^{-2(x^2+y^2)/r_0^2} e^{-2x^2/z_0^2} \quad (2.57)$$

The condition for this simplification is the correct size s_0 of the pinhole radius projected to the sample space and an underfilling of the objective:

$$w_0 \leq s_0 \leq \frac{0.5 \tan \alpha}{\tan \delta} w_0 \quad (2.58)$$

$$\delta \leq \frac{\alpha}{2} \quad (2.59)$$

Where α is the aperture half-angle of the microscope objective and δ is the focusing angle of the laser beam in the sample at $1/e^2$ intensity. The aperture half-angle α can be determined by the numerical aperture of the objective NA and the refractive index n :

$$\sin \alpha = \frac{NA}{n} \quad (2.60)$$

A defined Gaussian profile of the MDE is required for FCS optimized setups.

2.13.5 Signal to noise ratio

For a successful single molecule fluorescence measurement, a high signal to noise ratio is a key prerequisite. The number of detected photons obeys a Poisson distribution, so the probability of the detection of n photons is:

$$P(n) = \frac{n_{avg}}{n!} e^{-n_{avg}} \quad (2.61)$$

In a Poisson process, the number of observed occurrences fluctuates around its average value n_{avg} with a standard deviation σ_n , which is the noise of the signal:

$$\sigma_n = \sqrt{n_{avg}} = noise \quad (2.62)$$

The average detected photons n_{avg} can be calculated by the sum of the fluorescence signal n_f [63] and the background contribution.

The background consists of the background η_{bg} induced by the excitation laser and the dark signal η_{dark} from the detectors. The laser induced background is light from elastic Rayleigh and inelastic Raman scattering as well as fluorescence in the optical system and the solvent. Whereas the laser induced background is linearly dependent on the laser intensity, the dark signal is a constant, leading to a signal to noise ratio:

$$SNR = \frac{signal}{noise} = \frac{n_f}{\sqrt{n_{avg}}} = \frac{n_f}{\sqrt{n_f + \eta_{bg} + \eta_{dark}}} = \frac{\eta_{det} \cdot R \cdot T_{int}}{\sqrt{\eta_{det} \cdot R \cdot T_{int} + C_b \cdot I_L \cdot T_{int} + N_D \cdot T_{int}}} \quad (2.63)$$

η_{det} is the detection efficiency, R the emission rate of the fluorophore, T_{int} the integration time, C_b the constant of proportionality between the laser intensity I_L and laser induced background intensity, and N_D is the constant dark count rate of the detector.

The signal to noise ratio is plotted against the laser power in figure 2.14. It is optimized, in terms of laser excitation, when it reaches its maximum because of a saturation of the fluorescence signal. The yellow bar indicates the optimal laser power.

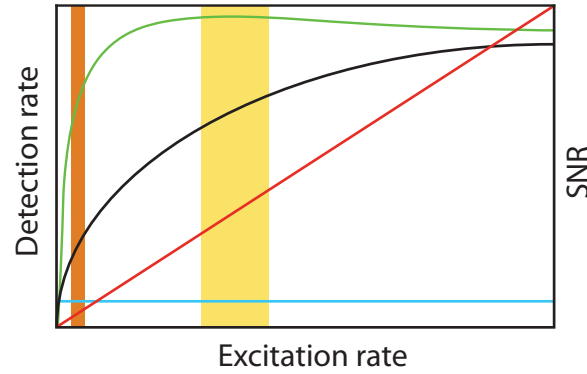


Figure 2.14: Signal to noise ratio (green) as a function of excitation laser intensity according to equation 2.63. It can be calculated with the intensity of the single molecule (black), the dark count rate (blue) and the laser induced-background signal (red). The optimal excitation rate considering photo bleaching (orange) is lower than without photobleaching (yellow) since a lower excitation rate is leading to less photobleaching.

2.14 Protein unfolding

Protein unfolding or protein denaturation is a process in which a protein changes its structure, thereby it can also lose its function. This can be a result of losing its unique 3D structure which is present in its native state. Hydrogen-bonds, hydrophobic interactions, ionic interactions and, in the presence of reducing agents, also disulfide bridges are dissolved by unfolding or denaturation. The strong covalent bonds of the primary structure, i.e. the amino-acid sequence, are unaffected by denaturation.

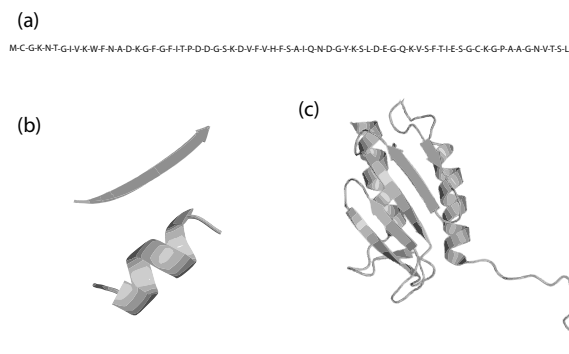


Figure 2.15: (a) Primary structure: amino-acid sequence (b) secondary structure: the three dimensional form of a local segment (e.g. an alpha-helix or a beta sheet) (c) tertiary structure: the three dimensional form of local segments (consists mostly of alpha-helices and beta sheets)

2.14.1 Denaturation by chemical influences

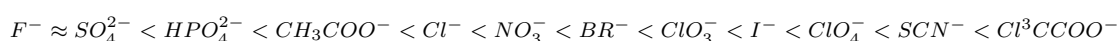
Chaotropic agents: The hydrophobic effect leads to a stabilization of the folded state because structures of water-soluble proteins have a hydrophobic core in which side chains are buried from water (see figure 2.16). By disrupting the hydrogen bonding network between water molecules, chaotropic agents can weaken the hydrophobic effect and thereby decrease the stability of the native state of the proteins in the solution.



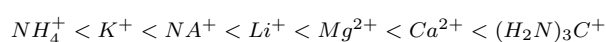
Figure 2.16: Strong (left) and weak (right) hydrophobic effect, demonstrated with hydrophobic (red) and hydrophilic regions (blue)

They are called chaotropic agents because they increase the entropy of water. On the other hand there are also antichaotropic agents, which will strengthen the hydrophobic interaction and lead to a stabilization of the protein. The Hofmeister series is a classification of these ions by their chaotropic effect on macromolecules. The early members are antichaotropic and the later chaotropic.

The following list orders the anions in the series:



cations:



For example, Guanidinium chloride is a really chaotropic agent and was used in this thesis for chemical unfolding:



A serious problem in the interpretation of chemical denaturation is caused by the fact that the thermodynamic parameters are also influenced by the binding of the denaturant molecules to multiple sites on a protein. This binding changes the chemical potential of the protein in an unpredictable way [78].

PH-denaturation Denaturation of proteins can occur at both higher and lower pH outside the optimal pH Region of a protein (see figure 2.17)

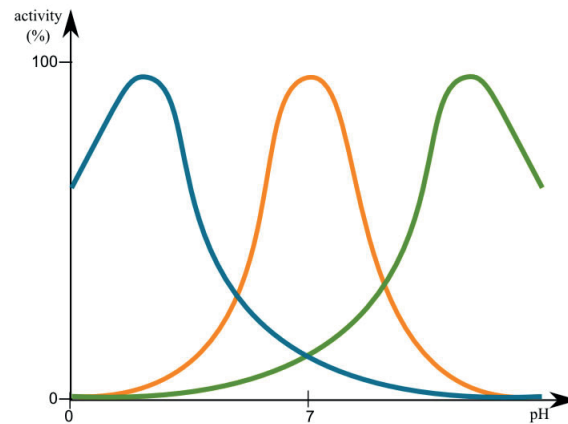


Figure 2.17: Optimal pH region for three different enzymes: pepsin (blue) amylase (orange) and trypsin (green)[79]

At low pH the acid is a proton donor (H^+) and therefore destroys hydrogen bonds and protonates for example the carboxyl groups (COO^-) of the amino acid aspartate and glutamate, producing carboxyl groups ($-COOH$). This inhibits the ionic interaction. In the same manner a base is changing the compositions of the ions.

For these reasons, buffers are used to stabilize the pH during a measurement.

Ethanol, Methanol or other organic solvents Ethanol, propanol or other organic solvents can disrupt hydrogen bonds and thus overcome the hydrophobic effect by dehydration. Thereby they denature membrane proteins, inactivating bacteria and mycells, and destroying the protection layer of viruses. These solvents are often used for disinfection, because they are volatile in contrast to chaotropic agents which are salts. Every denaturation method as well as pressure and heat can be used for sterilization. It has to be noted that pressure has the weakest quality influences for food sterilization.

2.14.2 Temperature denaturation

Increasing the temperature leads to an increasing Brownian motion, which first of all influences the long range interactions and the tertiary structure is changed. By further heating, internal hydrogen bonds and helical structures are destroyed and new hydrogen bonds of the amino acids are built. Therefore and because of aggregation, almost every protein unfolds irreversibly

by temperature. According to le chateliers principle any process which is induced by increasing temperature, should proceed with heat absorption and thus with an increase in the enthalpy and entropy i.e. with disordering of the system under consideration. Hence heat denaturation is an obvious effect. The logical consequence is not to expect that cooling could lead to any significant change of protein structure. A decreasing temperature should lead to increasing order and the native state is the most ordered [76]. But also cold denaturation is possible. The molecular origin is still under debate but the most common interpretation of the origin of this phenomenon is the decreasing strength of the hydrophobic effect with decreasing temperature, which is expected to be connected to changes in the structure and dynamics of the hydration layer around the polypeptide chain [77]. Temperature unfolding leads to changes in volume and thermal energy, and it is difficult to separate these effects from another.

2.14.3 Pressure denaturation

Pressure effects are also governed by le chateliers principle, which states that a system tends to minimize the effect of any external factor by which it is perturbed. By contrast to temperature variation, the internal energy is nearly independent of pressure and an increase of pressure leads solely to a reduction of the volume of the system [78]. The volume change can be written as the sum of three terms:

$$\Delta V = \Delta V_{atoms} + \Delta V_{cavities} + \Delta V_{hydration} \quad (2.64)$$

where ΔV_{atoms} equals zero because the volume of the atoms stays constant. $\Delta V_{cavities}$ is the change of the volume of the cavities, whereas $\Delta V_{hydration}$ is the volume change of the hydration shell resulting from the interactions of the protein with the solvent.

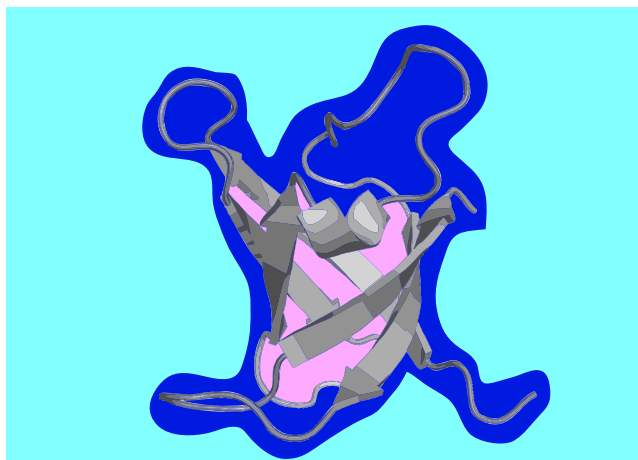


Figure 2.18: Volumes associated with the dissolved protein: bulk water (cyan), hydration shell (blue), void (pink) and the protein (gray)

The size of the protein hydration shell increases by the exposure of hydrophobic residues. This increase is more than compensated by the negative contribution to the change in volume from the disruption of electrostatic and hydrophobic interactions because the exposure of polar and charged groups will lead to a decrease in volume due to electrostrictive effects [78]. Studies have revealed a lack of correlation between protein size and volume change, demonstrating that the exposure of surface area and the accompanying changes in solvent density are not major determinants of the magnitude of pressure effects [80]. In contrast, it could be demonstrated that increasing the amount of internal void volume in the folded states of proteins leads to significant increases in the magnitude of the volume change of unfolding [81]. Hence, the biggest negative contribution is the elimination of internal cavities and voids in proteins under pressure. In general, the volume changes are quite small, typically less than 1% of the total protein volume [82].

Let us take a look at the effect of pressure at the different scales:

Primary structure: The sequence of amino acids is held together by covalent bonds which are really stable and will not be disrupted by pressure at least up to pressure values of 10-15 kbar [78].

Secondary structure: The secondary structure is defined by patterns of hydrogen bonds between the main-chain peptide group. Hydrogen bonds are quite stable depending on the protein. The secondary structure remains essentially unaltered because the replacement of intra-protein hydrogen bonds by protein-water hydrogen bonds on their putative destruction

would be accompanied by rather small changes in volume [78].

Tertiary structure: The tertiary structure is stabilized by hydrogen bonds, ionic interactions, hydrophobic interactions and disulfid bonds. The sensitive tertiary structure controls the basic function of the protein and is much more pressure unstable.

Quaternary structure: Intersubunit regions of oligomeric proteins are rich in weak electrostatic and hydrophobic contacts, which stabilizes their quaternary structure. That is why relatively moderate pressures (0.5-2 kbar) may induce dissociation of oligomeric proteins by weakening these interactions [78].

2.14.4 Thermodynamics of protein folding

The ratio between the concentration of the unfolded proteins c_D and folded proteins c_N expressed as follows Boltzmann's statistics:

$$\frac{c_D}{c_N} = \exp\left(-\frac{\Delta\mu}{RT}\right) \quad (2.65)$$

where R is the gas constant, T the temperature, and $\Delta\mu$ is the difference in chemical potential between the unfolded and the native state:

$$\Delta\mu = \mu_D - \mu_N = -RT \cdot \ln\left(\frac{c_D}{c_N}\right) \quad (2.66)$$

For $\Delta\mu < 0$ more proteins are unfolded,

for $\Delta\mu = 0$ there is an equal population of unfolded and folded proteins and

for $\Delta\mu > 0$ more proteins are folded.

For sake of simplicity and to deal only with a two dimensional phase diagram, here only temperature and pressure unfolding will be considered for the calculation of the chemical potential. If the chemical potential only depends on pressure and temperature, it can be approximated by a Taylor expansion at a reference point: $(P_R; T_R; \Delta S_R; V_R; \Delta\mu_R)$, only considering terms up to the second power:

$$\Delta\mu = \Delta\mu_R + \left(\frac{\partial\Delta\mu}{\partial T}\right)_R(T-T_R) + \frac{1}{2}\left(\frac{\partial^2\Delta\mu}{\partial T^2}\right)_R(T-T_R)^2 + \left(\frac{\partial\Delta\mu}{\partial p}\right)_R(p-p_R) + \frac{1}{2}\left(\frac{\partial^2\Delta\mu}{\partial p^2}\right)_R(p-p_R)^2 +$$

$$\left(\frac{\partial^2 \Delta\mu}{\partial T \partial p}\right)_R (T - T_R)(p - p_R) + \dots \quad (2.67)$$

Thereby the entropy change can be defined as:

$$\Delta S_R = -\left(\frac{\partial \Delta\mu}{\partial T}\right)_R \quad (2.68)$$

the volume change is:

$$\Delta V_R = \left(\frac{\partial \Delta\mu}{\partial p}\right)_R \quad (2.69)$$

the isobaric heat capacity was defined by:

$$\Delta C_P = -T_R \left(\frac{\partial^2 \Delta\mu}{\partial T^2}\right)_R \quad (2.70)$$

the isothermal compressibility:

$$\Delta \beta_T = -\left(\frac{\partial^2 \Delta\mu}{\partial p^2}\right)_R \quad (2.71)$$

and thermal expansion coefficient:

$$\Delta \alpha_P = \left(\frac{\partial^2 \Delta\mu}{\partial T \partial p}\right)_R \quad (2.72)$$

So the difference in chemical potentials between the unfolded and the native proteins at a pressure p and a temperature T is:

$$\begin{aligned} \Delta\mu(T, P) = \Delta\mu_R - \Delta S_R(T - T_R) - \frac{1}{2} \frac{\Delta C_P (T - T_R)^2}{T_R} + \Delta V_R(p - p_R) - \frac{1}{2} \Delta \beta_T (p - p_R)^2 + \\ \Delta \alpha_P (T - T_R)(p - p_R) \end{aligned} \quad (2.73)$$

The difference in chemical potentials of the unfolded and the native state at constant atmospheric pressure of 1 bar is:

$$\Delta\mu(T, 1bar) = -\frac{1}{2} \frac{\Delta C_P (T - T_R)^2}{T_R} - \Delta S_R(T - T_R) +$$

$$(1\text{bar} - p_R) \left[-\frac{1}{2} \Delta\beta_T (1\text{bar} - p_R) + \Delta\alpha_P (T - T_R) + \Delta V_R \right] + \Delta\mu_R \quad (2.74)$$

Figure 2.19 shows the effect of temperature on the difference of the chemical potential of the unfolded and the folded state for ZN-cytochrome c for constant atmospheric pressure. It was calculated with the following thermodynamic parameters:

Table 3: Thermodynamic parameters of ZN-cytochrome c [83]

ΔC_P	$\Delta\beta_T$	$\Delta\alpha_P$	$\Delta V(p_R = 0.91\text{GPa}, T_R = 298\text{K})$	$\Delta S(p_R = 0.91\text{GPa}, T_R = 298\text{K})$
$(\frac{\text{kJ}}{\text{mol}\cdot\text{K}})$	$(\frac{\text{cm}^3}{\text{mol}\cdot\text{GPa}})$	$(\frac{\text{cm}^3}{\text{mol}\cdot\text{K}})$	$(\frac{\text{cm}^3}{\text{mol}})$	$(\frac{\text{kJ}}{\text{mol}\cdot\text{K}})$
5.87	148.1	0.139	-74.6	-0.263

Whereas the entropy of the native state is almost constant with temperature, the entropy of the denatured state decreases with decreasing temperature. The slope of the chemical potential as a function of temperature for the denatured state decreases, while the chemical potential of the native state is linear with temperature. This is the reason why the chemical potentials meet twice (and thus $\Delta\mu = 0$) at the temperature of heat denaturation T_H and cold denaturation T_C . At the temperature of maximal stability T_M the chemical potential and consequently the folded population is maximal.

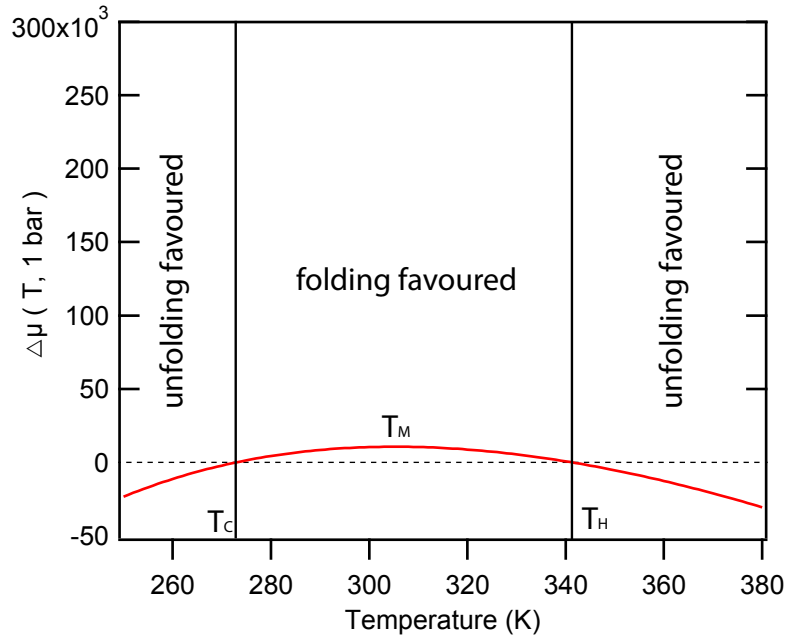


Figure 2.19: Temperature dependent chemical potential with the thermodynamic parameters of ZN-cytochrome c

Analogous to temperature and with the same thermodynamic parameters, the chemical potential can be expressed as it changes with pressure:

$$\Delta\mu(280\text{K}, p) = -\frac{1}{2} \frac{\Delta C_P (300\text{K} - T_R)^2}{T_R} - \Delta S_R (300\text{K} - T_R) + (p - p_R) \left[-\frac{1}{2} \Delta\beta_T (p - p_R) + \Delta\alpha_P (300\text{K} - T_R) + \Delta V_R \right] + \Delta\mu_R \quad (2.75)$$

Figure 2.20 shows the pressure effect on the difference of the chemical potential of the folded and the unfolded state at 280 K :

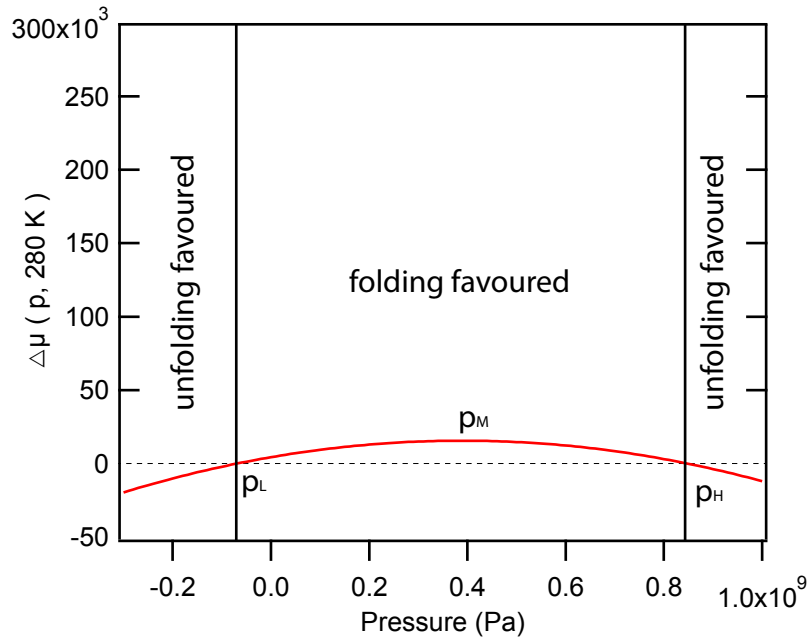


Figure 2.20: Pressure dependent chemical potential with the thermodynamic parameters of ZN-cytochrome c

Already mentioned in section 2.14.3 the unfolded volume V_D is smaller than the native V_N in the real existing positive pressure regime:

$$V_D < V_N$$

The volume of the native state V_N stays constant, while the unfolded state is compressible. Hence the slope of the chemical potential μ_D decreases and the chemical potential of the native and the unfolded proteins meet at the pressure of denaturation p_H where the unfolded and the native population are equal and the chemical potential is zero. A second crossing occurs at negative pressure p_L . Negative absolute pressure is not possible for a perfect gas, but

it is possible for liquids and solids. In solids it is called tension, and happens when a solid is stretched. Solids can resist the forces due to the internal attractive forces between its molecules. In liquids what usually happens when you try to apply negative absolute pressure is cavitation, the formation of bubbles when the pressure drops below the vapor pressure of the fluid. The first experiment were performed by Berthelot in 1850 using spinning capillaries[84]. Stretched states of water at pressures as low as -250 bars have been observed using the same model [85]. p_M is the pressure of maximal stability where $\Delta\mu$ and consequently the folded population are maximal.

To calculate the p-T phase diagram, the corresponding pressure for every temperature at the equilibrium of the native and the unfolded state whith:

$$\Delta\mu = 0 \quad (2.76)$$

has to be calculated.

Therefore equation 2.73 has to equal zero:

$$\begin{aligned} & -\frac{1}{2} \frac{\Delta C_P (T - T_R)^2}{T_R} + -\Delta S_R (T - T_R) + \\ & (p - p_R) \left[-\frac{1}{2} \Delta \beta_T (p - p_R) + \Delta \alpha_P (T - T_R) + \Delta V_R \right] + \Delta \mu_R = 0 \end{aligned} \quad (2.77)$$

Bringing that to a quadratic form:

$$\begin{aligned} & (p - p_R)^2 + \frac{-2[\Delta \alpha_P (T - T_R) + \Delta V_R]}{\Delta \beta_T} (p - p_R) \\ & + \frac{\frac{\Delta C_P (T - T_R)^2}{T_R} + 2\Delta S_R (T - T_R) - 2\Delta \mu_R}{\Delta \beta_T} = 0 \end{aligned} \quad (2.78)$$

and solving it gives:

$$\begin{aligned} & (p - p_R)_{1,2} = \frac{[\Delta \alpha_P (T - T_R) + \Delta V_R]}{\Delta \beta_T} \pm \\ & \sqrt{\frac{[\Delta \alpha_P (T - T_R) + \Delta V_R]^2}{(\Delta \beta_T)^2} - \frac{\frac{\Delta C_P (T - T_R)^2}{T_R} + 2\Delta S_R (T - T_R) - 2\Delta \mu_R}{\Delta \beta_T}} \end{aligned} \quad (2.79)$$

In figure 2.21 the phase transition curve for ZN-cytochrome c is shown (red line in fig 2.21). Inside the ellipse, folding is favored and outside the unfolded state is favored.

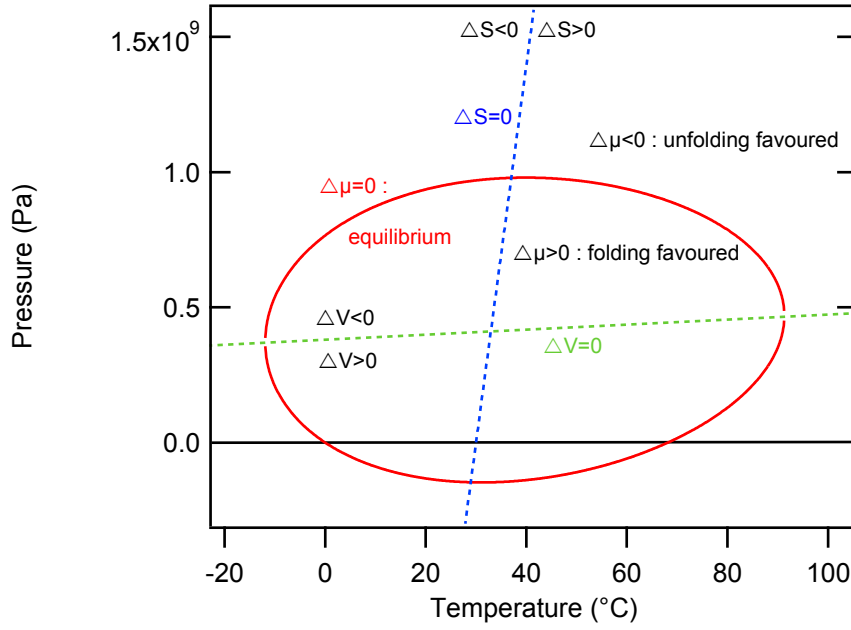


Figure 2.21: p-T phase diagram of ZN-cytochrome c

The temperature of the highest stability of the native state (blue line in fig 2.21) at a specific pressure can be calculated [83]:

$$\Delta S = 0; T_m(p) = T_{m_0} \left(1 + p \cdot \frac{\Delta \alpha_p}{\Delta C_p} \right) \quad (2.80)$$

Also the pressure of the highest stability (green line in fig 2.21) of the native state at a specific temperature can be calculated [83]:

$$\Delta V = 0; p_m(T) = 1 + \left(\frac{\Delta \alpha_p}{\Delta \beta_T} \right) (T - T_{m_0}) \quad (2.81)$$

where T_{m_0} is the temperature of the highest stability at atmospheric pressure.

The change in volume between the native and the unfolded state is calculated by $\partial \Delta \mu / \partial p = \Delta V$ according to equation 2.69 :

$$\Delta V = \Delta V_R + \Delta \alpha_P (T - T_R) - \Delta \beta_T (p - p_R) \quad (2.82)$$

If there are no reference values known, to describe a temperature unfolding at constant pressure, the chemical potential $\Delta \mu$ is calculated from a reference point at the temperature of maximal stability of the native state and the pressure that is held constant during the experiment :

$$\begin{aligned}\Delta\mu(T, P_R) = \Delta\mu_{m,R} - \Delta S_m(T - T_m) - \frac{1}{2} \frac{\Delta C_P(T - T_m)^2}{T_m} + \Delta V_R(P_R - P_R) \\ - \frac{1}{2} \Delta\beta_T(P_R - P_R)^2 + \Delta\alpha_P(T - T_m)(P_R - P_R)\end{aligned}\quad (2.83)$$

and at the temperature of maximal stability, the chemical potential is maximal $-\partial\Delta\mu(T_m)/\partial T = 0$, the entropy equals zero $\Delta S_m = 0$ and the chemical potential at constant pressure can be described as:

$$\Delta\mu(T, p_R) = \Delta H_m - \frac{1}{2} \frac{\Delta C_P(T - T_m)^2}{T_m} \quad (2.84)$$

If there are no reference values known, to describe a pressure unfolding at a constant temperature T_R , the chemical potential $\Delta\mu$ is calculated from a reference point at the pressure of maximal stability of the native state p_M , and the temperature T_R that is held constant:

$$\begin{aligned}\Delta\mu(T_R, p) = \Delta\mu_m - \Delta S_R(T_R - T_R) - \frac{1}{2} \frac{\Delta C_P(T_R - T_R)^2}{T_R} + \Delta V_m(p - p_M) \\ - \frac{1}{2} \Delta\beta_T(p - p_m)^2 + \Delta\alpha_P(T_R - T_R)(p - p_m)\end{aligned}\quad (2.85)$$

and with $\partial\Delta\mu(T_m)/\partial T = \Delta V_m = 0$ the chemical potential becomes:

$$\Delta\mu(T_R, p) = \Delta G_m - \frac{1}{2} \cdot \Delta\beta_T(p - p_m)^2 \quad (2.86)$$

2.14.5 Mechanism of the folding process

In the 1960s Anfinsen's laboratory found that proteins can fold reversibly. The amino acid sequence of ribonuclease A (RNase A) contains the information needed to make the correct four disulfide bonds of the native protein although there are 105 different possible disulfide bonds [107]. Anfinsen proposed that the proteins fold under the driving force of a free energy gradient and the native structures are conformations at the global minima of their accessible free energy and asked for the mechanism of this folding process [106].

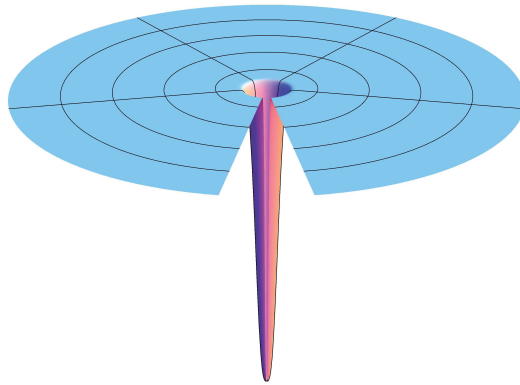


Figure 2.22: Levinthal landscape[109]

Levinthal's paradox Levinthal argued that random searching would not find the native states corresponding to the hypothetical flat playing field shown in figure 2.22. When a ball rolls randomly on a flat course it takes an infinite time to find and fall in the hole. From this perspective, as Levinthal notes, proteins would have a serious search problem .

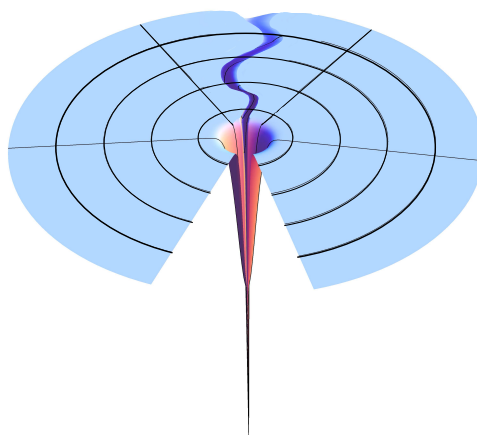


Figure 2.23: The pathway solution[109]

Pathway solution A plausible solution is that there has to be folding intermediates and pathways [100, 101]. This is shown in figure 2.23.

But when Levinthal's calculation was repeated in 1992 with the addition of a small free energy bias as the driving force for folding, the time needed to search all conformations by a random search process, was reduced to a few seconds [102].

Hence, another problem arose, namely the Levinthal dichotomy of thermodynamic versus kinetic control: Does the protein fold by a pathway independent reaching of its most stable structure or is it choosing the fastest folding pathway [108].

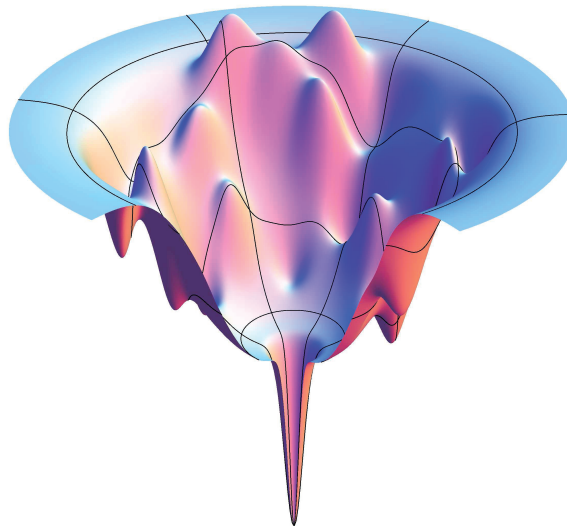


Figure 2.24: Folding funnel [109]

Folding funnel and energy landscapes The idea of an energy landscape of heterogeneous conformations came up with the groundbreaking investigation of the protein Myoglobin by Frauenfelder et al. [103, 104, 105], because it was possible to show that only several conformations and dynamic transformations between these conformations enable the function of a protein.

An energy landscape is the Gibbs energy of every conformation. The conformation is defined by the coordinates of all N atoms in a protein. The vertical axis represents the Gibbs energy, including the sum of the hydrogen bonds, ion pairs, torsion angle energies, hydrophobic and solvation free energies for a chain in a particular conformation. The many lateral axes represent the conformational coordinates; each conformation is represented by a point on the

multidimensional energy surface. Conformations that are similar geometrically are close to each other on the energy landscape. Hills correspond to energetically unfavored conformations that are called intermediate states and valleys are configurations that are more favorable than others nearby, thus they are more populated.

Hence, the process of folding or unfolding can be described as a ball rolling down on this energy surface, that is shaped like a funnel. Instead of following a folding pathway, the protein can take any possible trajectory down a folding funnel. For an ensemble of proteins, folding can be seen as a diffusive process of proteins represented by rolling balls on particular trajectories on the energy landscape [108].

2.14.6 The denatured or unfolded state

The denatured state of a protein is not a single fixed state, but a collection of states of very similar energies that are in very rapid equilibrium with each other [86]. The denatured states are of special interest, because they are the starting point of the protein folding reaction and the stability is defined as the difference in free energies between the native and the denatured states. In cells the native and the denatured state are in dynamic equilibrium [91, 89, 90]. There are also some proteins that can only cross a lipid bilayer after reconvertng into a partially folded or denatured conformation [92, 93, 94]. Additionally, the denatured state is the primary target for degradative enzymes [95, 96, 97].

Intrinsically unfolded proteins The classical view of proteins is that an amino acid sequence specifies a three dimensional sturcture, which is the prerequisite for a proteins function. But this is not always the case: Many proteins require intrinsic disorder to fulfil its function. These, so called intrinsically disordered proteins, represents up to half of the proteins of organisms with a larger proteom size (see figure 2.25). Therefore the denatured state is also important for a better understanding of the function of a protein.

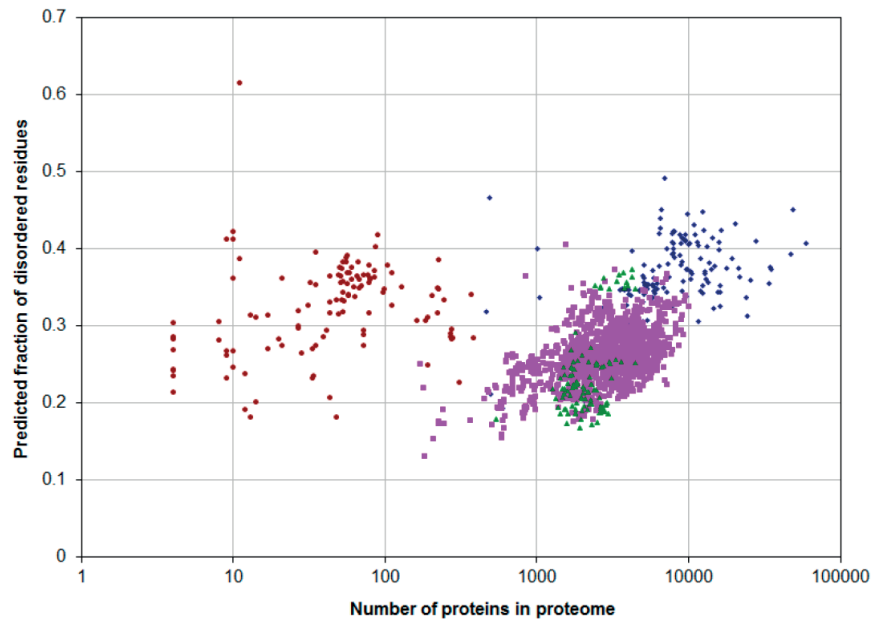


Figure 2.25: Fraction of disordered residues against number of proteins in proteome: Viruses (red), archaea (green), bacteria (pink) and eukaryota (blue) [88]

There are several models for the structure of the denatured state:

Random coil:

The random coil is an ideal chain. The only constraints are bond angles. Poly-amino acids and long linear DNA often behave like random coils. For a denatured protein, the random coil model may seem like a natural choice, but denatured proteins can be quite compact even though they are disordered. Although classical experiments by Tanford [91] showed that several proteins in 6M guanidinium hydrochloride (Gdmcl) exhibit the hydrodynamic properties of random coils, this is not the case for all denatured states. Most of them behave like nonideal polymer chains.

Nonideal polymer chains:

Nonideal chains undergo attractive interaction of hydrogen bonds and hydrophobic forces. Also steric repulsion, because of the excluded volume effect, are influencing the nonideal chain.

Solvent effects If the polymer segments are weakly soluble due to the hydrophobicity, these segments will undergo a hydrophobic collapse to reduce the unfavorable interactions with the

solvent. On the other hand, a good solvent will make the chain more extended. A theta solvent makes intersegment attractions counteract the excluded volume repulsion, hence it creates unique conditions for evaluating the basic properties of chain molecules, because a solution of polymers then conforms to theories for ideal chain molecules. However one should have in mind that although the length scales proportional to a fractional power of the number of segments like the random coil:

$$R_N \propto N^{1/2}, \quad (2.87)$$

in other respects, the behaviour is different from that of a random coil. Excluded volume prevents compact conformations from forming and this is compensated by attractive forces that make the more extended conformations less likely. Consequently the probability distribution for the end-to-end distance of a polymer in a theta solvent is sharper than for an ideal chain [98].

Investigation of the denatured state As mentioned above the properties of the denatured state depend on the solvent conditions. The denatured state under physiological conditions, D_0 is the most relevant to an understanding of protein stability, but most proteins under native conditions are stable by $\Delta\mu = +(5 - 20)$ kcal/mole. With equation 2.66 one can see that protein chains in the D_0 state are very rare under physiological conditions. Consequently, experimental studies have concentrated on denatured states under non physiological conditions. Analyzing how the properties of denatured states vary under these more extreme conditions and extrapolation back to physiological conditions, can give an estimation of the properties of D_0 [87]. To develop better experimental models for D_0 , it is necessary to characterize molecules at the margin of stability. Only unstable molecules, for example the investigated protein yeast frataxin, have significant populations of denatured conformations at physiological conditions. Single molecule FRET studies can give insight into the D_0 behaviour, since the unfolded state can be investigated separately from the folded, even if lowly populated. Pressure studies can give a different insight because it is assumed to have a weaker influence on the denatured state.

3 Material and methods

3.1 Confocal microscope

The fluorescence measurements were carried out using a custom built confocal microscope with a 60X water immersion objective (CFI Plan Apo VC 60XWI, Nikon) with a NA of 1.2, a working distance of 0.31-0.28 mm and a glass thickness correction collar (CC) of 130-190 μm . With the piezo actuators (P-733.2CL, P-721.CLQ, Physik-Instrumente GmbH & Co. KG) the sample can be scanned in three dimensions within a range of 100 \times 100 \times 100 μm (x,y and z).

A pulsed Laser with a wavelength of 470 nm (LDH-P-C470, Picoquant GmbH) or a pulsed Laser with a wavelength of 635 nm (LDH-P-P635, Picoquant GmbH) was used for the fluorescence lifetime measurements, and three continuous wave lasers with a wavelength of 488 nm (PC13589, Spectra Physic Cyan, Newport Corp.), 594 nm (Obis 594LS, Coherent) and 640 nm (OBIS 640LX, Coherent) were used for the fluorescence excitation of all other measurements. The repetition rate of the pulsed lasers can be regulated by a driver (Sepia-PDL-808, Picoquant GmbH, Berlin, Germany). The laser power is measured at the entrance of the objective (IM) and tuned mechanically by a screw in the pathway before the fibre.

Our setup is optimized for single molecule measurements. To achieve the best signal to noise ratio, we need a small as possible excitation volume, hence we overfill the objective ($\delta > \alpha$) with a laser beam diameter of 8 mm defined by an aperture. Consequently the laser intensity is an airy disc. We used a 50 μm pinhole (PH) between two tube lenses (TL) which is thereby small enough to suppress the maxima of higher orders of the airy disc and big enough to let enough photons pass. In the detection pathway the same pinhole was used to suppress background light because only light that was emitted from the excitation focus can be transmitted.

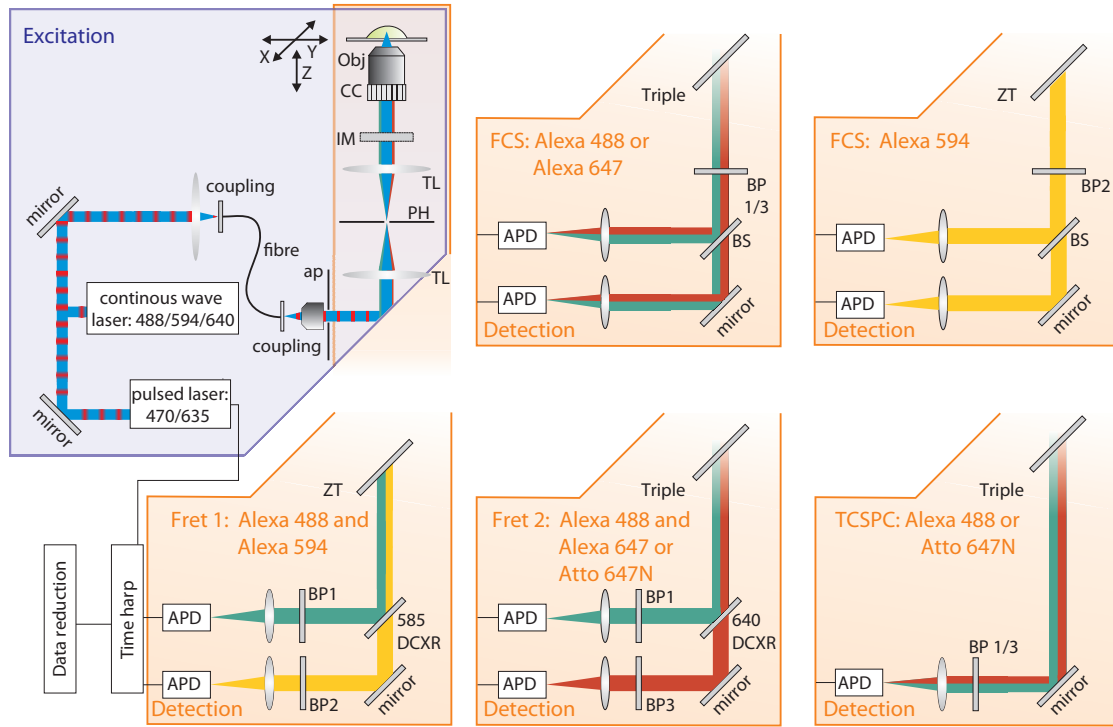


Figure 3.1: Confocal microscope (abbreviations can be found in red in the text). The fluorophore-excitation part (purple) can be combined with different detection pathways (orange), depending on the application: FCS (Fluorescence Correlation Spectroscopy), FRET (Fluorescence Resonance Energy Transfer) or a TCSPC (Time Correlated Single Photon Correlation)-fluorescence-lifetime measurement

The detection light was separated from the emission light with a dichroic mirror (ZT 488/594 for Alexa Fluor 488 and Alexa Fluor 594 and Triple Z 405/470/633 for Alexa Fluor 488 and Alexa 647/Atto 647N, Chroma).

For the FCS experiments, the photons were separated by a 50/50 beamsplitter (BS) and only one band-pass filter is used for both detection channels, (positioned in front of the beam-splitter) depending on the fluorophore [BP1: HQ525/50 (Alexa Fluor 488), BP2: HQ650/100 (Alexa Fluor 594) and BP3: HQ685/70 (Alexa 647), AHF Analysetechnik]. The fluorescence intensity was measured in two channels and crosscorrelated to remove afterpulsing effects.

For the FRET measurement, the emitted photons were separated by wavelength with a longpass filter into a donor and an acceptor channel (585DCXR for Alexa Fluor 488/Alexa594, Chroma and BS640DCXR for Alexa Fluor 488/Atto647N and for Alexa Fluor 488/Alexa647, AHF Analysetechnik). Additionally, there was a bandpass filter in every channel [BP1: HQ525/50 (Alexa Fluor 488) for the donor channel and BP2: HQ650/100 (Alexa Fluor 594) and BP3:

3.2 Pressure setup

HQ685/70 (Atto 647N) for the acceptor channel, AHF Analyse-technik] to suppress background photons.

The fluorescence photons were detected with two **APDs** (SPCM-AQR 14, PerkinElmer Optoelectronics, Massachusetts, USA), one for every channel.

For the **TCSPC**-fluorescence-lifetime measurement only one band-pass filter is used depending on the observed dye (**BP1**: HQ525/50 for Alexa Fluor 488 and **BP3**: HQ685/70 for Atto 647N). For the lifetime measurement, the photons have been detected with an **APD** (Micro Photon Devices, Bolzano, Italy), which has a considerably enhanced timing accuracy compared to traditional APDs.

To record the detected photons, single-photon counting electronics were used (**Timeharp** 200, Picoquant GmbH).

3.2 Pressure setup

3.2.1 High pressure microscopy

High pressure up to 2 kbar was generated by a system similar to that described by Gratton [56, 60], where a capillary served as the pressure cell with an observation window. The pressure was generated by pushing water into this capillary by a screw piston pump (see figure 3.2). The difference is that we chose a square bore silica capillary as the pressure cell, instead of a cylindrical, because of its better optical properties.

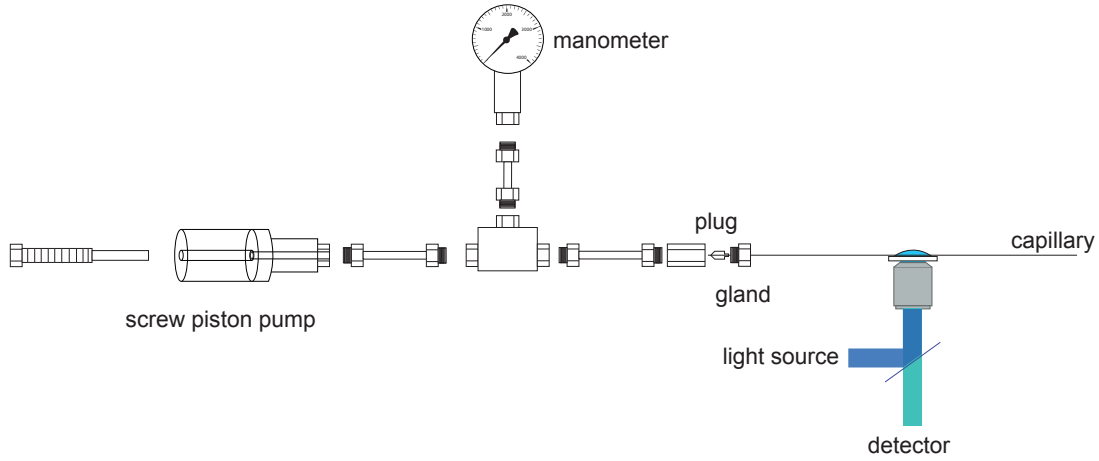


Figure 3.2: Schematic drawing of the instrument. The capillary, connected to the high-pressure-screw-piston-pump (stainless steel, 37-5.75-60, PTG pressure technology, Frankfurt am Main, Germany) and the manometer (0-4000 bar, Ø100 mm, PTG pressure technology, Frankfurt am Main, Germany) is placed on the confocal microscope for fluorescence measurements under pressure.

This fused silica microcapillary (Z-FSF-050365, Postnova) has a refractive index of $n=1,45-1,46$ depending on the wavelength (see figure 3.5), an inner diameter of $50\pm5\text{ }\mu\text{m}$, and an outer diameter of $300\pm15\text{ }\mu\text{m}$ (pictures in detail, taken with a digital microscope, can be seen in Appendix A.2). We chose a silica capillary and not a borosilicate because of its better stability. The tensile strength of borosilicate is 7 MPa, but 50 MPa of fused silica [111, 110]. The capillary is covered with a $30\text{ }\mu\text{m}$ protection layer of polyimide for a better stability during transport and preparation. The pressure cell is shown in figure 3.3. It should be mentioned that sapphire is much more pressure resistant with a tensile strength of 186.4 MPa, but it is not suited to be used as a pressure cell because of its very different refractive index (compared to borosilicate) of $n=1.77$, which would lead to even stronger aberrations than with fused silica. As can be seen in figure 3.3 b), the glass is not perfectly flat, which will also lead to aberrations.

3.2 Pressure setup



Figure 3.3: (a) Schematic cross-section of the fused silica capillary with polyimide protection layer (orange), roughly to scale. (b) Photo of the inner wall of the capillary made with a digital microscope (VHX-5000, Keyence).

We used a 20 cm long capillary and removed a 20 mm long area of the protection layer with the flame of a blow torch to form an observation window. Then we cleaned the capillary with acetone and glued it into a custom-built capillary pressure plug (see figure 3.4 a) with an epoxy resin (301-2,EPO-TEK). This bonding was baked for 3.5 hours at 80°C to harden the adhesive.

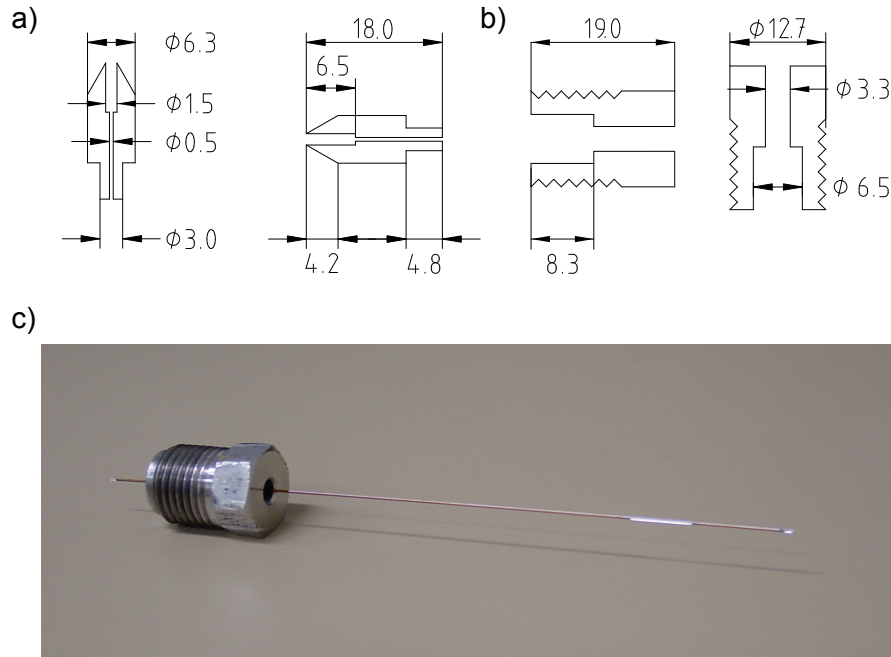


Figure 3.4: (a) Pressure plug made of brass (b) pressure gland made of stainless steel (c) Photo of the capillary glued into the pressure plug with epoxy resin and inserted in the pressure gland (left). 20 mm of the protection layer have been removed for the fluorescence measurement and the tip of the capillary has been closed by the flame of a blow torch (right). (all dimensions are in mm)

Then we filled in the sample solution of interest by capillary force, dipping the end of the capillary into the solution. To close the capillary, the very end was touched by the flame of a propane-oxygen blowtorch. The other end was then dipped into an oil drop to separate the solution from the pressurizing liquid. Finally, we inserted the pressure plug with the capillary into the pressure gland (figure 3.4b). Then we connected the capillary to a pressure screw piston pump (37-5.75-60, PTG pressure technology) with the pressure gland (see Appendix A.1 for the complete capillary handling instruction). The piston pump can generate pressure up to 4000 bar by pushing water in the capillary. A manometer (0-4000 bar, Ø100 mm, PTG pressure technology, Frankfurt am Main, Germany) was used to read the pressure. A simplified scheme of the pressure setup is shown in figure 3.2.

3.2.2 Reduction of optical aberrations and the new arrangement

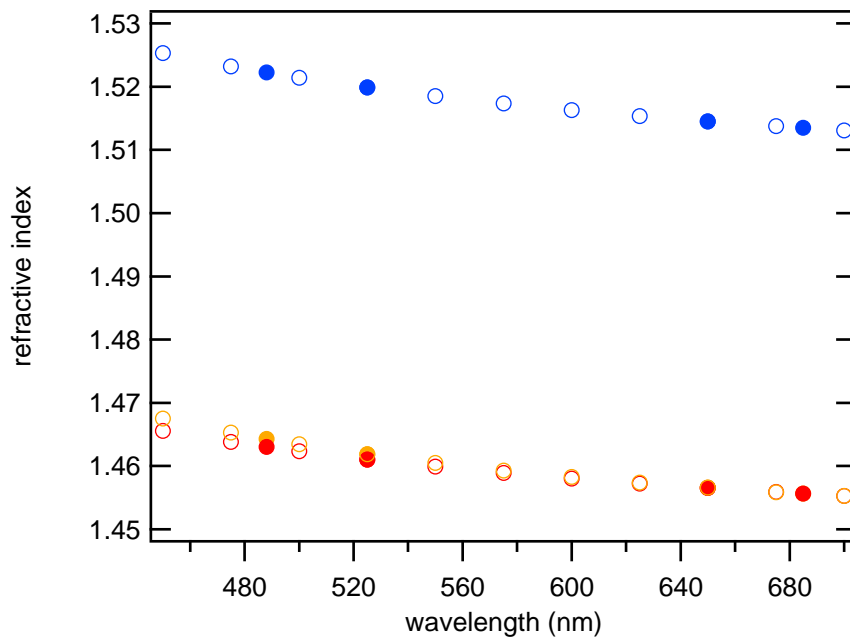


Figure 3.5: Refractive indices of the used materials: Cargille FS 50350 (orange), fused silica (red) and borosilicate (blue). The important values at the donor excitation wavelength (488 nm), the donor channel wavelength (525 nm), the acceptor channel wavelengths (650 nm and 685 nm) are highlighted.

As there is no microscope objective with a high numerical aperture which is made for fused silica, we had to use an objective made for a No. 1 standard borosilicate coverslips. This leads to an offset of the optical path due to the different refractive indices (see figure 3.5) between the capillary and the coverslip (see figure 3.6 a). Additionally, the rays that go through the sidewalls, are strongly distracted (figure 3.6 b).

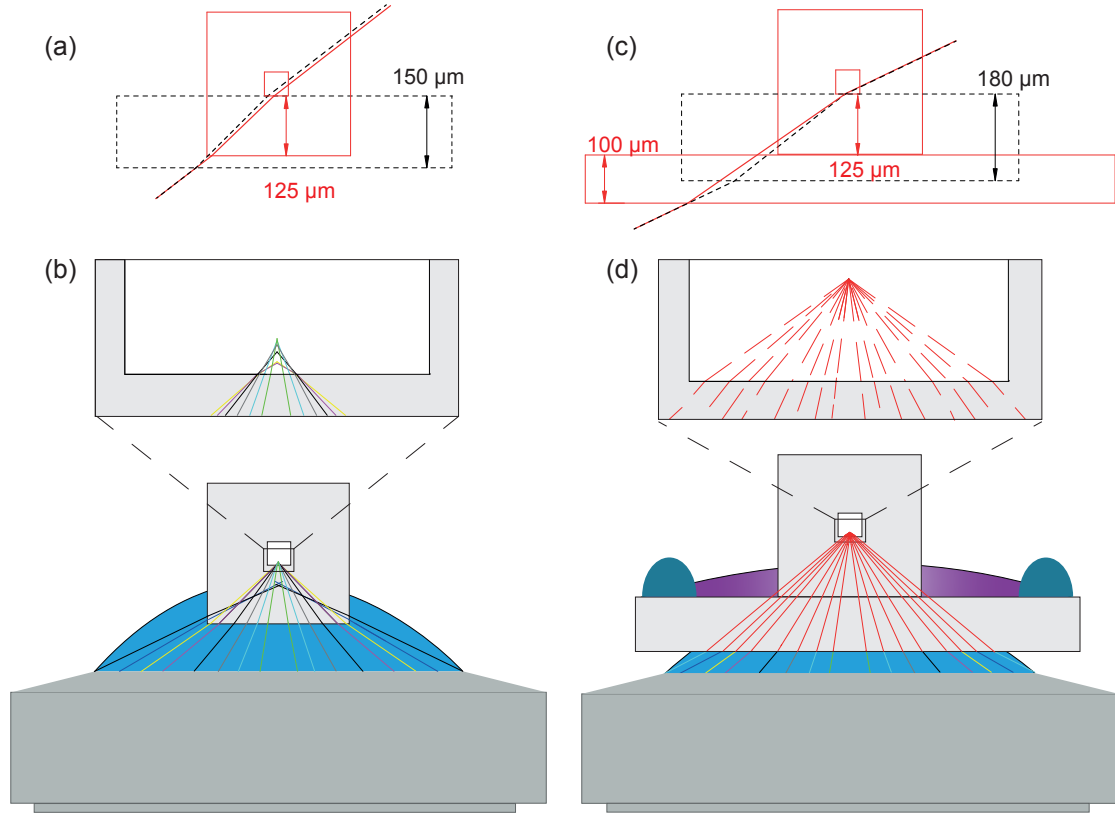


Figure 3.6: (a) Optical path of the capillary (solid, red) and of a No. 1 borosilicate coverslip (dotted, black) showing the different offsets due to different refractive indices and thicknesses. (b) Optical paths while focusing into the capillary with a WI microscope objective with the correction collar set to 150 μm showing optical aberrations. A combination of the capillary, a 100 μm fused silica coverslip and an index matching gel (Cargille FS 50350, dispersion in figure 3.5) is used to reduce the optical aberrations inside the capillary: (c) No deviation for one specific beam angle for a fused silica thickness of 225 μm and an objective correction collar setting of 18. (d) idealized scheme of the optical path in the new arrangement, where the capillary is immersed in an index matching gel (purple) on top of a 100 μm thin fused silica coverslip (grey). The rubber cement (green) serves as a basin for the index matching gel (see figure 3.8) .

To solve the refractive index problem, we addressed the question of a different optimal fused silica thickness, that has the same beam offset as a No. 1 standard borosilicate coverslips, to avoid the diffractions, resulting from a different refractive index. Therefore this optimal fused silica thickness d versus the beam angle β was calculated for different correction collar settings

3.2 Pressure setup

y (see Appendix A.3) :

$$d = y + y \cdot \cos \beta [\tan(\sin^{-1}(\frac{1.33}{1.46} \sin \beta)) - \tan(\sin^{-1}(\frac{1.33}{1.53} \sin \beta))] \frac{\cos(\sin^{-1}(\frac{1.33}{1.46} \sin \beta))}{\sin(\beta - \sin^{-1}(\frac{1.33}{1.46} \sin \beta))} \cos \beta \quad (3.1)$$

The beam angle β can not be eliminated in this equation, so there is not one perfect thickness. Every beam angle needs a different thickness for a perfect alignment.

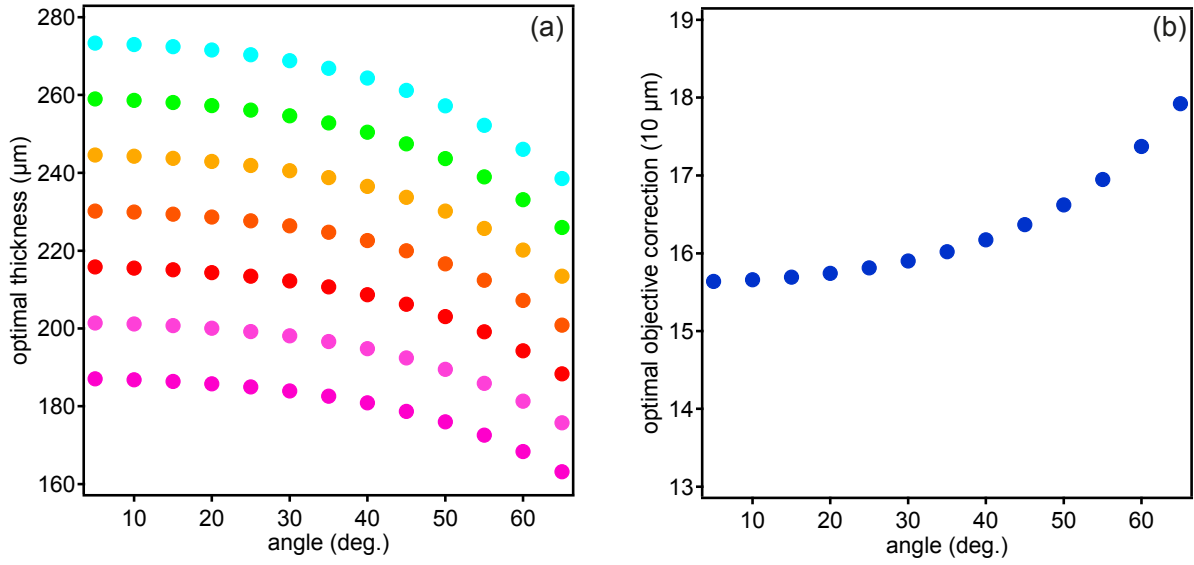


Figure 3.7: (a) Optimal thickness of a fused silica coverslip vs. beam angle calculated according to eq. 3.1. The calculations are based on a WI microscope objective with the correction collar set to 13 to 19 (i.e. objective optimized for a 130 μm (pink) to a 190 μm (cyan) borosilicate coverslip) (b) Optimal objective correction collar setting vs. beam angle calculated for 225 μm fused silica thickness according to eq. 3.1 .

However, we can conclude from figure 3.7a, that the optimal thickness for the different correction collar settings of our objective and the possible beam angles are in the range from 160 μm to 270 μm. We could have chosen every thickness in this range. Unfortunately there are no square fused silica capillaries available with appropriate dimensions and custom made capillaries are very expensive, so we put a thin fused coverslip below the capillary to get the required thickness. Given a wall thickness of 125 μm of our capillary, a fused silica coverslip with a thickness between 35 μm to 145 μm has to be placed under the capillary.

We chose the thinnest available fused silica coverslip of 100 μm (Hellma Optik). This enabled us to also avoid the sidewall-effects by immersing the capillary in an optical gel of suitable refractive index (see figure 3.5) that can be put on top of this coverslip (see figure 3.6

d). A 15 mm diameter circle of rubber cement (Fixogum, Marabu) was put on the capillary and the coverslip. It serves as a bassin for the optical gel to avoid a dripping from the coverslip and at the same time, it fixes the capillary to the coverslip (see figure 3.8).

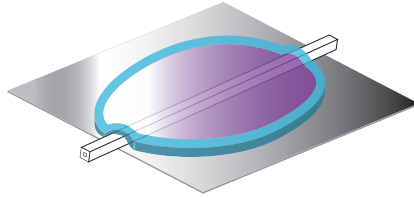


Figure 3.8: **The new arrangement:** The capillary has been fixed with rubber cement (cyan) on top of a fused silica coverslip (grey). The rubber cement also serves as a bassin for an optical gel (purple) that has the same refractive index as fused silica.

Thus, the resulting fused silica thickness totals to about 225 μm (see figure 3.6 c). With the fused silica thickness of 225 μm we could optimize every beam angle, by adjusting the correction collar (see figure 3.7 b) and with the refractive index matching gel a light refraction at the sidewalls can be avoided. Unfortunately, every beam angle is optimized with a different correction collar setting. To find the best correction collar setting, FCS-, microsphere- and FRET-measurements at different collar settings have been carried out (see section 4.1). Nevertheless, the optics will not be perfect. In section 4.2, it has been investigated, how much worse the optics are compared to the coverslip and how much they have been improved compared to the bare capillary.

3.2.3 Theoretical pressure stability

To estimate the stability of the capillary, the maximal stress was calculated and compared with the yield stress of fused silica of $\sigma_{\text{fused silica}} = 5.88 \text{ GPa}$ [71]. The yield stress is the minimal tension, where the material begins to deform plastically. But the material shows reversible deformation at lower stress, which can lead to a breaking of the material. So it is just the maximal stress, that can be theoretically applied without permanent and irreversible deformation. A number of factors can reduce the effective operating limit. These include internal contamination from cutting or cleaving debris, damage to the interior from packing media, the use of aggressive or unfiltered solvents that may attack or damage the internal surface, external handling damage and other cumulative applied stresses such as bending or twisting of the capillary [73].

cylindrical fused silica capillaries The tangential stress σ_t , the radial stress σ_r and the longitudinal stress σ_l on a pressurized cylinder at a distance r of the center is [72]:

$$\sigma_t(r, p) = \frac{r_i^2}{r_o^2 - r^2} \left(1 + \frac{r_o^2}{r^2} \right) \cdot p \quad (3.2)$$

$$\sigma_r(r, p) = \frac{r_i^2}{r_o^2 - r^2} \left(1 - \frac{r_o^2}{r^2} \right) \cdot p \quad (3.3)$$

$$\sigma_l(r, p) = \frac{r_i^2}{r_o^2 - r^2} \cdot p \quad (3.4)$$

where r_i is the inner radius, r_o the outer radius and p the pressure in the cylinder. For stability estimations only the tangential stress matters because:

$$\sigma_t \geq \sigma_r, \sigma_l \quad (3.5)$$

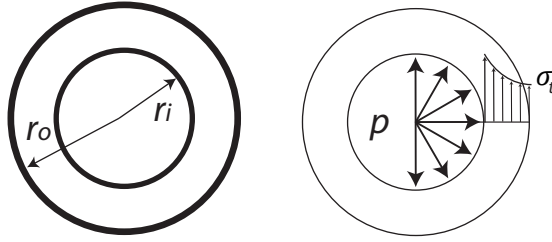


Figure 3.9: Tangential stress distribution

The highest stress occurs where $r = r_i$ which is at the inner wall of the capillary. This equation suggests that if the capillary we used ($r_i = 25 \mu\text{m}$; $r_o = 150 \mu\text{m}$) were cylindrical, this would lead to a tangential stress of:

$$\sigma_{max} = \sigma_t(25 \mu\text{m}, p) = 1.057 \cdot p \quad (3.6)$$

The tangential stress in the capillary is 1.057 times the pressure in the capillary. For a pressure of $4000 \text{ bar} = 0.4 \text{ GPa}$ the tangential stress is $\sigma_t = 0.423 \text{ GPa}$. Hence it is one order of magnitude smaller than the yield stress of fused silica ($\sigma_{fused \text{ silica}} = 5.88 \text{ GPa}$).

square fused silica capillaries For a squared capillary the stress can not be calculated analytically, but had to be calculated with finite elements. In contrast to a cylindrical capillary,

with an evenly distributed stress at the surface, in a square capillary the stress is not homogeneously distributed but is concentrated in the corners because of a higher bending moment (see figure 3.10).

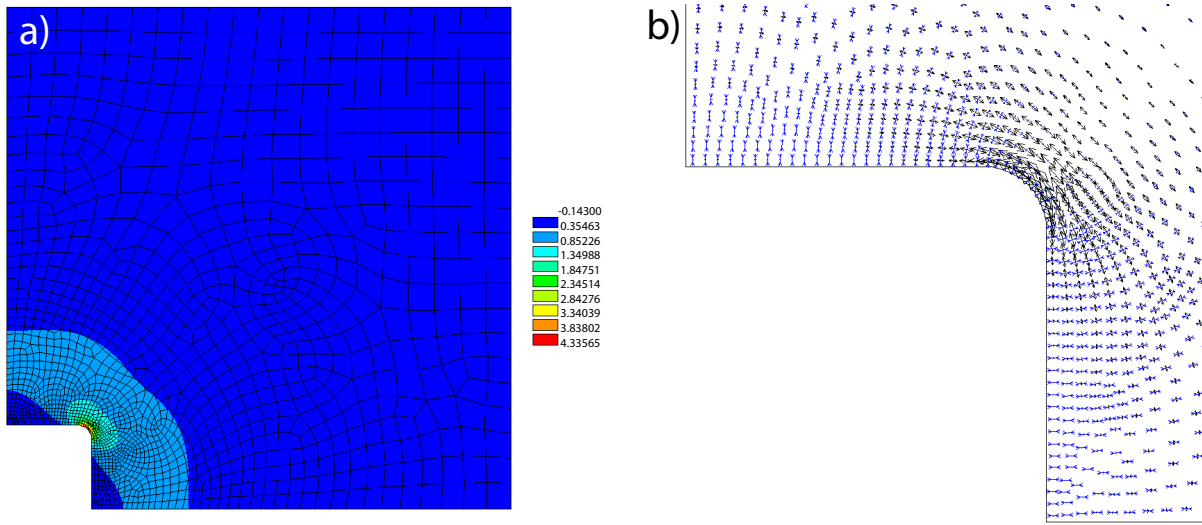


Figure 3.10: a) Maximal tensile stress and b) direction of the tensile stress in the square capillary. Because of the symetry only a quarter of the cross section has been investigated by B. Schieck, Fachhochschule Lübeck, Fachbereich M+W, Lübeck.

The result of the finite element calculation (B. Schieck, Fachhochschule Lübeck, Fachbereich M+W, Lübeck, Deutschland) stated that the maximal stress is 4.3 times the pressure in the capillary.

$$\sigma_{max} = 4.3 \cdot p \quad (3.7)$$

So in the corners of the square capillary the stress is about 4 times higher than at the inner wall of the cylindrical capillary, by applying the same pressure.

For example for a pressure of 4000 bar = 0.4 GPa the maximal stress is $\sigma_{max} = 1.7$ GPa . Hence it is only a factor 3 times lower than the yield stress of $\sigma_{fused\ silica} = 5.88$ GPa [71]

3.3 Temperature control

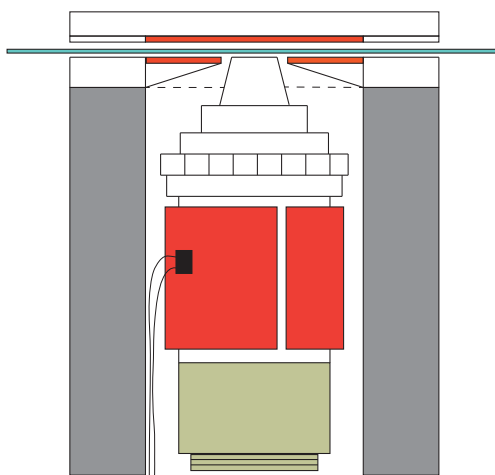


Figure 3.11: Heating plates and objective heating (red), capillary (green) and PEEK-adapter (yellow-green)[74]

We also implemented a temperature-controlled heating unit for determining the p-T phase diagram of a biomolecule. The microscope has been modified according to figure 3.11. Therefore the microscope stage was replaced by a custom built microscope stage that includes two heating plates (Friedrich Freek, Menden Germany). The two plates can heat the capillary from above and from the bottom. The top heating (10 W, $14.4\ \Omega$) and the bottom heating (6 W, $24\ \Omega$) can produce a temperature of up to 65°C and its temperature is controlled by a PT-100 ($100\ \Omega$, Friedrich Freek, Menden Germany) temperature sensor in the top heating plate. To avoid a loss of heat also the objective was heated by a resistance wire in a heat conducting double-faced adhesive tape that was wrapped around the objective. A second PT-100 element controlled the temperature at the objective, that must not exceed 40°C to prevent damage of the objective. Additionally, the objective was thermally isolated from its mount by a custom made adapter made of polyetheretherketon (PEEK). The temperature of the heating plates and the objective heating was regulated by two microprocessor based multifunctional controllers (model 5320, Drews electronic, Kamp-Lintfort Germany).

3.4 Samples

In table 4, all samples are listed.

Table 4: All samples that have been used in the work

sample	fluorescent label	buffer	measurement	manufacture
Alexa Fluor 488	-	water	FCS/lifetime	Invitrogen
Atto 647N	-	water	FCS/lifetime	ATTO-TEC
Rhodamine B	-	water	lifetime	Sigma Aldrich
fl.microspheres	blue/green/orange/dark red	water, 1.5 % Agarose gel	focal volume	Invitrogen
dsDNA	AF488/AF594	Mops (20 mM, PH 7.2)	FRET/FCS	IBA GmbH
dsDNA	AF488/Atto647N	Mops (20 mM, PH 7.2)	FRET/FCS	IBA GmbH
SlyD	AF488/Atto647N	Mops (20 mM, PH 7.2)	FRET	Dana Kahra
CspA	AF488/AF647	Mops (20 mM, PH 7.2)	FRET	Erik Hinze
Fratxin	AF488/AF594	Mops (20 mM, PH 7.2)	FRET	Ben Schuler

3.4.1 Dyes

Five different dyes have been used in this work, Alexa 488, Alexa 594, Alexa 647, Atto 647N and Rhodamine B. Alexa dyes (Molecular Probes, Invitrogen, Darmstadt, Germany) and Atto dyes (ATTO-TEC, Siegen, Germany) have a high quantum efficiency and photo stability. They are water-soluble and their fluorescence is pH-independent. Rhodamine B has been used for the temperature test because of its linear temperature dependence of the fluorescence lifetime (see figure 4.18) .

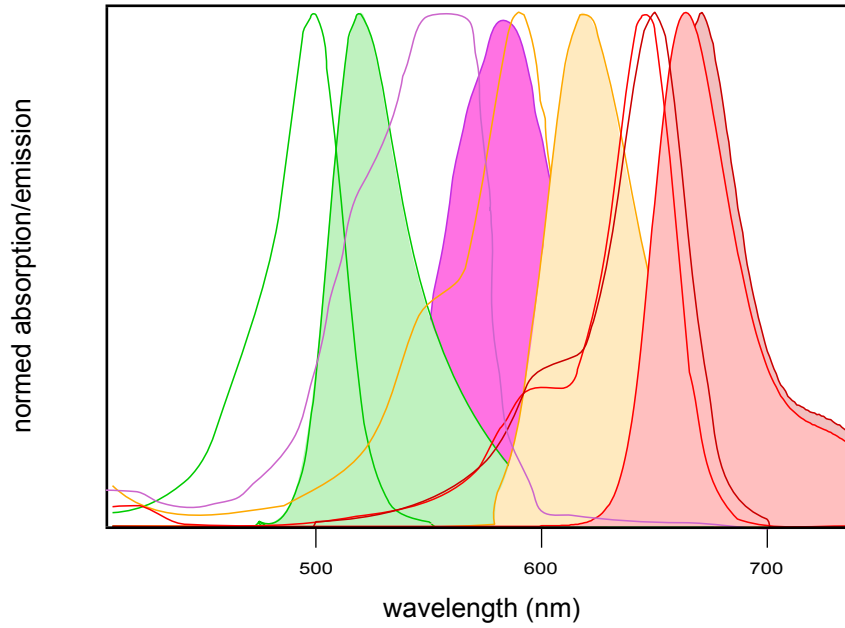


Figure 3.12: Normalized absorption (line) and emission (filled) spectra of alexa 488 (green), Alexa 594 (yellow), Atto 647N (red), Alexa 647 (dark red) and Rhodamine B (magenta) [116, 117, 127]

Pure dyes have been used for the lifetime, FCS and pressure test measurements. Therefore the dyes have been simply diluted in water. For all other experiments the dyes have been linked to dsDNA or to the protein, that was investigated, and diluted in a Mops-buffer (20 mM, PH 7.2) with 0.1% Tween.

Table 5: Important values of the fluorophores: wavelength at the absorption maximum λ_{abs} , wavelength at the emission maximum λ_{em} ; extinction coefficient ε , fluorescence lifetime τ and quantum yield Q

dye	$\lambda_{abs}(\text{nm})$	$\lambda_{em}(\text{nm})$	$\varepsilon(\frac{10000}{\text{cmM}})$	$\tau(\text{ns})$	Q
Alexa Fluor 488 [117]	495	519	73	4.1	0.92
Alexa Fluor 594 [117]	590	617	92	3.6	0.66
Alexa Fluor 647 [117]	650	665	270	1.0	0.33
Atto 647N [116]	646	664	150	3.5	0.65
Rhodamine B [118][121]	562	583	106	1.7	0.70

3.4.2 Fluorescent microspheres

The measurement of the focal volume was carried out using UV/blue/green/orange/dark red Tetraspeck microspheres (T7279, Invitrogen). TetraSpeck microspheres are stained through-

out with four different fluorescent dyes, so that the microspheres display four well-separated excitation/emission peaks determined by a synchronous fluorescence spectrum scan of the microsphere [119] (see figure 3.13). The dyes are BODIPY derivatives and, separated, they have different absorption/emission maxima at 350/440 (UV), 490/515 (blue/green), 545/575 (orange) and 650/680 (dark red) compared to the spectrum of the fluorescent microspheres (figure 3.13 and table 6). A scan of the fluorescent spheres can be used to determine the focal volume, because of their subresolutional size of 100 nm. They have been dissolved in agarose gel to avoid any movement of the spheres during a scan. The refractive index of $n = 1.336$ of 1.5% agarose gel in water has been measured with an abbe refractometer (K7135, Exacta&Optech, Munich, Germany). Hence the gel has a refractive index very close to water.

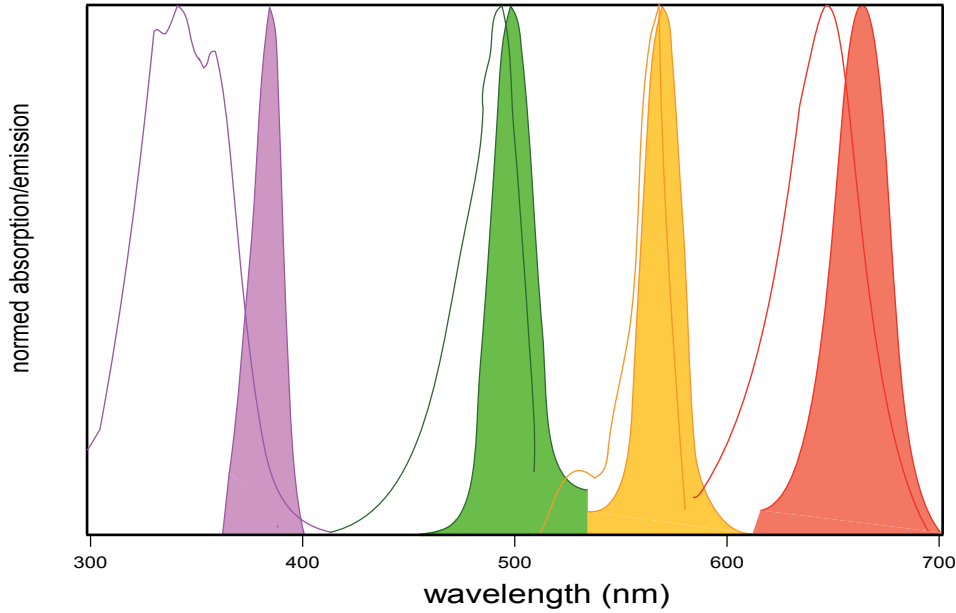


Figure 3.13: Normed absorption (line) and emission (filled) spectra of the dyes contained in the Tetraspeck[119]

Table 6: Important values of the fluorophores in a TetraSpeck microsphere : wavelength at the absorption maximum λ_{abs} , wavelength at the emission maximum λ_{em} [119]

	$\lambda_{abs}(\text{nm})$	$\lambda_{em}(\text{nm})$
UV	341	385
blue/green	497	499
orange	570	572
dark red	648	668

3.4.3 dsDNA

Double stranded DNA (dsDNA), consisting of 23 base pairs, has been labeled with the fluorophores Alexa 488 and Alexa 594 or with Alexa 488 and Atto 647N (IBA GmbH, Göttingen, Germany) at the thymine-bases with a donor(AF 488)-acceptor(AF 594/Atto647N)-distance of 9 base pairs :

5'-TAACACAGG(dt-AF488)CCCATCTGAATCG-3'

3'-ATTGTGTCCAGGGTAGAC(dt-AF594/Atto647N)TAGC-5'

It was dissolved in a Mops-buffer (20 mM, PH 7.2, 0.1% Tween) for the FCS- and the FRET-benchmark to have similar conditions as for a protein measurement.

Labeled dsDNA has been used for FRET-reference measurements to qualify the FRET-measurement quality and because of its high pressure stability it was used for a negative control.

3.4.4 SlyD (PDB ID: 2K8I)



Figure 3.14: Structure of SlyD of *Thermus thermophilus*, alpha helix in pink, β -sheet in yellow[120]

The protein SlyD was produced in *Thermus thermophilus* and cys-tag labeled by Dana Kahra (Institut of Physics, University of Lübeck). Therfor the protein was cystein-mutated. For an unspecific Alexa 488/Atto647N binding, aspartic acid at position 82 and threonin at position 139 have been mutated into cysteins.

The primary structure of the mutated SlyD is

MKVGQDKVVT IRYTLQVEGE VLDQGELSYL HGHRNLIPGL EEALEGREGG

EAFQAHVPAE KAYGPHDPEG VQVVPLSAFP EC(Af488/Atto647N)AEVVPGAQ

FYAQDMEGNP MPLTVVAVEG EEVTVDNFHP LAGKDLDFQV

EVVKVREAC(Af488/Atto647N)P EELLHGHAH

Table 7: Important properties of SlyD

isoelectric point	pI	4.35
average mass	m_{avg}	16303.36 Da
most abundant mass	$m_{monoisotopic}$	16293.02 Da
optical density	OD_{280}	0.32
extinction coefficient	ε	5216.0 $\frac{1}{M \cdot cm}$

SlyD is a two domain-protein which undergoes an open and a closed formation (see figure 4.19). It has been chosen for an investigation of the influence of pressure on the conformational equilibrium of the two conformations.

3.4.5 CspA (PDB ID: 2L15)



Figure 3.15: Structure of Cold-shock protein A of *Escherichia coli*, alpha helix in pink, β -sheet in yellow[120]

The cold shock protein A from *E. coli* was produced in *E. coli* and cys-tag labeled by Erik Hinze (Max-Planck-research-group: Enzymology of protein folding, Halle, Germany). Therefore the protein was cysteine-mutated. At the first stock of CspA (sample 4), serine at position 2 was cysteine mutated for a specific Alexa 647 binding and alanine at position 59 was cysteine mutated for a specific Alexa Fluor 488 binding. The second stock of CspA (sample 3) was shotgun labeled at the same positions (unspecifically).

The primary structure of the mutated CspA is:

MC(AF488)GKNTGIV KWFNADKGF GFITPDDGS KDV FVHFS AI QNDGYKSLDE

GQKVSFTIESG(AF647)K GPAAGNVTSL

Table 8: Important properties of CspA

isoelectric point	pI	5.45
average mass	m_{avg}	7403.34 Da
most abundant mass	$m_{monoisotopic}$	7398.63 Da
optical density	OD_{280}	0.32
extinction coefficient	ε	6970.0 $\frac{1}{M \cdot cm}$

Cold shock protein A was investigated because it is a simple two state folder and a model folding protein.

3.4.6 Frataxin (PDB ID: 2GA5)

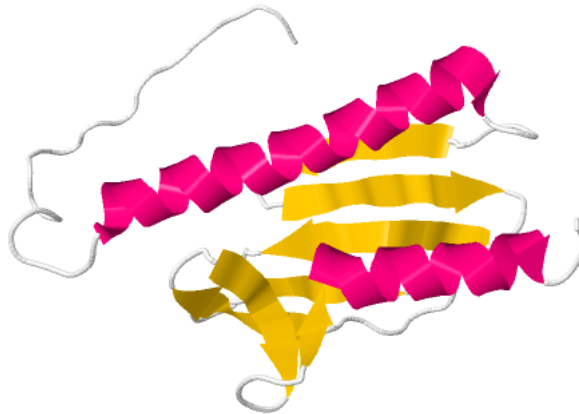


Figure 3.16: Structure of Frataxin of yeast *Saccharomyces cerevisiae* alpha helix in pink, β -sheet in yellow [120]

Gene synthesis and construction of the expression plasmid for recombinant Yhf1 (Frataxin) was carried out by EZBiolab (Carmel, USA). Based on the pFra1 expression plasmid, the

3.4 Samples

group of Benjamin Schuler (Departement of Biochemistry, University of Zurich, Switzerland) constructed a cystein mutated variant with V1M, C47S, N16C and S120C for an unspecific Alexa 488/594 binding. Frataxin, as a recombinant protein, was produced in *E. coli* but its DNA is from *saccharomyces cerevisiae* (yeast).

The primary structure of the mutated Frataxin is:

MESSTDGQVV PQEVL^C(AF488/594)LPLE KYHEEADDYL DHLLDSLEEL SEAHPD^SIPD

VELSHGVMTL EIPAFGTYVI NKQPPNKQIW LASPLSGPNR FDLLNGEWVS

LRNGTKLTDI LTEEVEKA^I^C(AF488/594)KSQ

Table 9: Important properties of Frataxin:

isoelectric point	pI	4.05
average mass	m_{avg}	13772.54 Da
most abundant mass	$m_{monoisotopic}$	13763.82 Da
optical density	OD_{280}	1.11
extinction coefficient	ε	15316.0 $\frac{1}{M \cdot cm}$

Frataxin was investigated because it is also a two state folder and very unstable at room temperature and ambient pressure. Not only that less pressure is needed for an unfolding, for all conditions an unfolded population of proteins remains, enabling an extensive investigation of the unfolded state.

3.4.7 Buffer

Under high pressure, the choice of the sample buffer is limited. Even buffers from the Good's list [112] can be bad pH controllers under high pressure [113]. In particular care must be taken to avoid buffers of high ionization volume such as phosphate buffers. For example the following buffers are suitable for high pressure measurements: CAPS for a pH-range of 9.5–11.5, Tris–HCl for a pH-range of 7–9, MES or Bis-Tris for pH-range of 5.5–7.5, and sodium acetate for a pH-range of 3.8–5.8 [115].

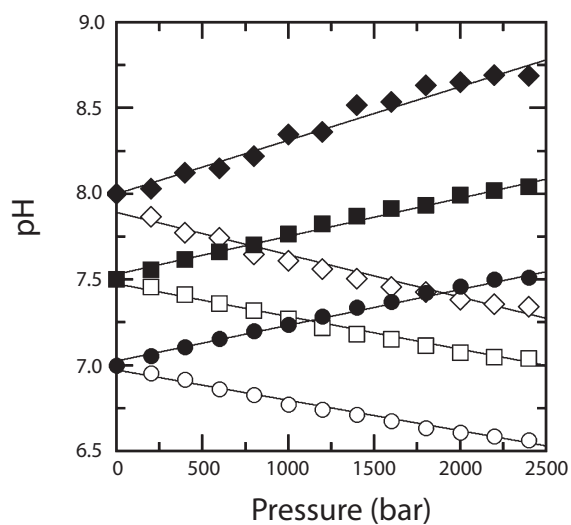


Figure 3.17: pH as a function of pressure. The change in pH with pressure is shown for Mops (closed symbols) and phosphate buffers (open symbols) at pH 7.0 (circles), 7.5 (squares), and 8.0 (diamonds)[113]

A MOPS (3-N-Morpholino-propanesulfonic acid)-buffer (20 mM, PH 7.2) was used with a structure analogous to MES (2-N-Morpholino-ethanesulfonic acid):

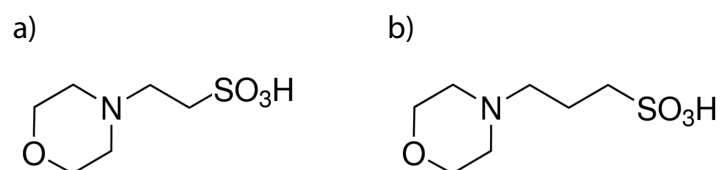


Figure 3.18: Structure of (a) MES and (b) Mops [13]

As can be seen in figure 3.17 the pH is pressure dependent. However, in the pH regime of 7-8, the stability of the investigated proteins remain constant (see figure 3.19)

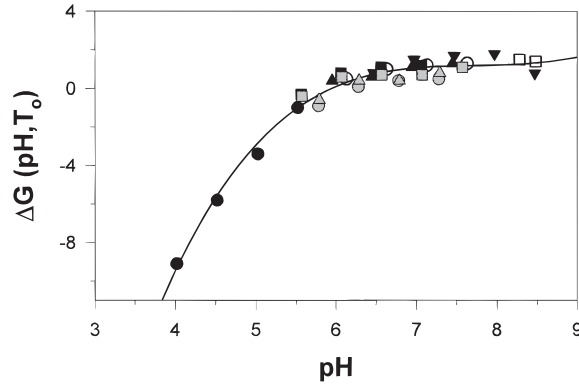


Figure 3.19: Dependence of the gibbs free energy of CspA unfolding at a reference temperature, $T=55^\circ\text{C}$, for different pH values [114].

To avoid adhesion on the big surface inside the capillary 0.1% of the detergent Tween 20 (Carl Roth GmbH, Karlsruhe, Germany) was added to the buffer for all measurements.

3.5 Data Reduction

For all investigations the labview user interface *scan_V5.3.6_aktuell.vi* has been used. With the programm the sample can be scanned in three dimensions and also a timetrace of the signal can be recorded.

With the user interface of the timeharp, the counting board timeharp 200 can record the detected photons into a .t3r file. Thereby the channel number, the arrival time of the photon (resolution: $\Delta t = 100 \text{ ns}$) and the time between the laser pulse and the arrival time (resolution: $\Delta t = 35 \text{ ps}$) are stored. All experimental data was then analyzed with home-written procedures in IGOR Pro (Wavemetrics, Portland, USA).

3.5.1 FCS measurement

For the FCS measurement, the .t3r file was loaded and the number of the detected photons were divided into time-bins of 1 ms with the igor procedure *schnitt_t3r*. The binned data was pseudo autocorrelated, by correlating the signals of the two detectors $I_1(t)$ and $I_2(t)$ to avoid afterpulsing, with the igor procedure *Korrelation*:

$$G(t, \tau) = \frac{\langle I_1(t) I_2(t + \tau) \rangle}{\langle I_1(t) \rangle \langle I_2(t) \rangle} \quad (3.8)$$

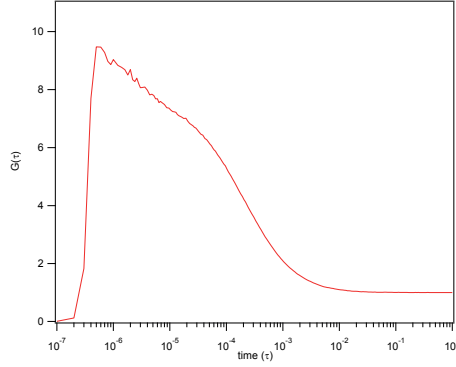


Figure 3.20: Autocorrelation curve

Assuming a three-dimensional Gaussian beam profile, the autocorrelation function depending on the the lag time τ can be fitted with (see section 2.11) :

$$G(\tau) = 1 + \frac{1}{\langle N \rangle} \left[1 + \frac{\tau}{\tau_d} \right]^{-1} \left[1 + S^2 \frac{\tau}{\tau_d} \right]^{-1/2} \left[1 + \frac{T}{1-T} \exp\left(-\frac{\tau}{\tau_T}\right) \right] \quad (3.9)$$

The parameters mean number of fluorescent molecules in the focal volume $\langle N \rangle$, the triplet fraction T , the triplet time τ_T , and the diffusion time τ_d can be determined from this fit. $S = \omega_{xy}/\omega_z$ is the ratio between the lateral radius ω_{xy} and the axial radius ω_z of the focal volume which was held constant at a value of $S = 0.2$ because the influence of the fit parameter is marginal.

Excitation benchmark:

The triplet fraction T and triplet time τ_T were used to calculate the transition rate $k_{isc}^{app} = \frac{T}{\tau_T}$ to the triplet state for the excitation benchmark for each used laserpower P . Then the saturation power P_{sat} was determined by fitting the transition rates with the relation:

$$k_{isc}^{app}(P) = \frac{K_{isc}}{1 + \frac{P_{sat}}{P}} \quad (3.10)$$

where a lower P_{sat} indicates that the laser is focused to a smaller spot, assuming a characteristic excitation intensity. (for further details see section 2.3).

Detection benchmark:

The molecular brightness β for the detection benchmarks can be calculated by:

$$\beta = \frac{\langle I \rangle}{\langle N \rangle} \quad (3.11)$$

$\langle I \rangle$ is the sum of the mean intensities of the two channels that were directly determined from the time trace of the APDs .

$\langle N \rangle$ was obtained from the fit of the crosscorrelation function of the two channels. The brightness was fitted with a four-level system model according to [122]:

$$\beta = \eta_d \sigma_{S01} \frac{K_r}{K_0} \frac{\phi_e}{1 + \frac{\phi_e}{\phi_{S1}} + \frac{\phi_e^2}{\phi_{S2}}} \quad (3.12)$$

The quantum efficiency $Q = \frac{K_r}{K_0}$ of the fluorophores can be found in table 5. The absorption coefficient $\sigma_{S01} = \frac{\ln 10}{NA} \varepsilon_{det}$ can be calculated from the extinction coefficient ε_{det} in the same table, knowing Avogadro's constant $NA = 6.022 \cdot 10^{23} \frac{1}{\text{mol}}$. The flux ϕ_e can be defined as:

$$\phi_e = \frac{2P}{h\nu\pi\omega^2} \quad (3.13)$$

where P is the laser power, the planck constant $h = 6.62610^{-34} \text{Js}$, ν the frequency of the fluorophore, and ω is the lateral diameter of the focal volume that can be found in table 12.

With this fit function, the saturation levels ϕ_{S1} and ϕ_{S2} , and most importantly, the detection efficiency η_d , which quantifies the detection quality, can be determined. ϕ_{S1} corresponds to the absorption of one photon, whereas ϕ_{S2} corresponds to the consecutive absorption of two photons.

3.5.2 Focal volume measurement

Two dimensional scans of the cross section of fluorescent microspheres were analyzed with Gaussian fits to determine the dimensions of the focal volume. Thereby the microspheres have been scanned several times and the biggest area has been taken for the evaluation, to be sure that we are scanning the cross section in the center of the focal volume. The scans have been fitted with

$$f(x, y) = A \exp -\frac{1}{2} \left[\left(\frac{x - x_0}{x_{width}} + \frac{y - y_0}{y_{width}} \right)^2 \right] \quad (3.14)$$

for an xy-cross section of the focal volume and

$$f(y, z) = A \exp -\frac{1}{2} \left[\left(\frac{y - y_0}{y_{width}} + \frac{z - z_0}{z_{width}} \right)^2 \right] \quad (3.15)$$

for an yz-cross section of the focal volume.

x_{width} , y_{width} and z_{width} are half the radii of the focal volume. The radius of a focal volume is defined as the distance from the center x_0 , y_0 and z_0 of the focal volume to the position where the intensity decreased to $1/e^2$ of the maximal Intensity A in the center of the focal volume. An exemplary scan of the cross section of the focal volume can be seen in figure 3.21. The fluorescent microspheres have been scanned with the labview programm *scan_V5.3.6_aktuell.vi* and analyzed in IGOR PRO.

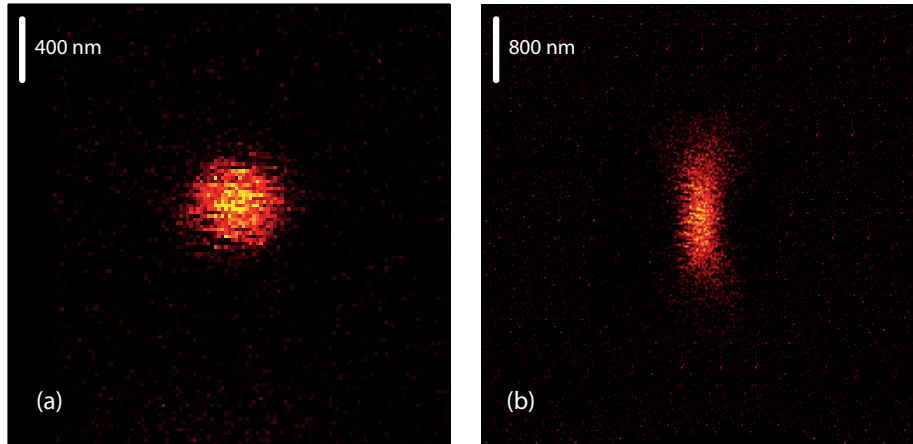


Figure 3.21: (a) xy- and (b) yz-cross section of a focal volume

3.5.3 FRET measurement

Data reduction was performed with home written procedures in IGOR PRO. The .t3r file was loaded and the number of detected photons were divided into time-bins of 1 ms. The transfer efficiency E of each time-bin was calculated with:

$$E = \frac{I_A}{I_A + \gamma I_D} \quad (3.16)$$

where I_A , I_D are the acceptor and donor intensities. The different quantum yields Q of the fluorophores and the detection efficiencies $\xi_{acceptor}$, ξ_{donor} of the different channels, can be considered by a correction factor γ (see table 10) :

$$\gamma = \frac{\xi_{acceptor} Q_{acceptor}}{\xi_{donor} Q_{donor}} \quad (3.17)$$

Table 10: Detection efficiencies ξ , quantum yields Q and correction factors γ of the different fluorophores of the FRET pairs used in this work

FRET pair	ξ_{donor}	$\xi_{acceptor}$	Q_{donor}	$Q_{acceptor}$	γ
donor: AF488/acceptor: AF594	0.30434	0.50929	0.92	0.66	0.833
donor: AF488/acceptor: AF647 [126]	0.28554	0.39750	0.92	0.33	2.003
donor: AF488/acceptor: Atto647N [126]	0.28554	0.34602	0.92	0.65	1.168

To construct a FRET-histogram, the first step is to "bin" the range of fret efficiency values into FRET-bins, dividing the range of one to zero into a series of intervals. Depending on the measurement quality the number of FRET-bins are chosen. For all histograms constructed in this work a FRET-bin number of 30 have been used. Then the number of transfer efficiencies of each time-bin, with a threshold level of 30 cts/ms for the sum of the donor and the acceptor intensity, that fall into a FRET-bin are counted. After adjusting the correction for the fluorophores and the sum threshold in the FRET panel, the panel displays a FRET-histogram of the measurement (see figure 3.22)

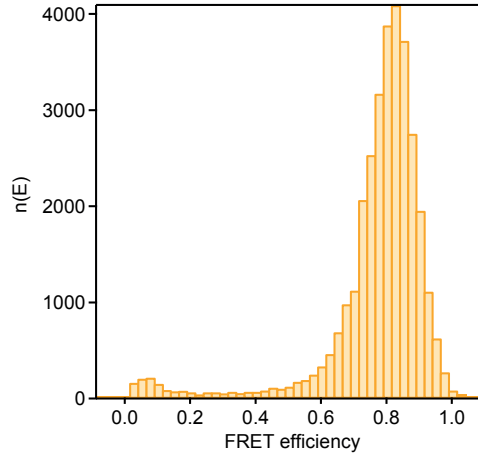


Figure 3.22: FRET-histogram

Since a FRET histogram is always broadened due to shot noise, it was fitted with a Gaussian function to obtain the mean fret-efficiency $\langle E \rangle$ and the *width*:

$$n(E) = A \exp\left[-\left(\frac{E - \langle E \rangle}{width}\right)^2\right] + n_0 \quad (3.18)$$

3.5.4 Fluorescence lifetime measurement

To measure the fluorescence lifetime τ of a fluorophore, a histogram $n(t)$ of the arrival times t of the photons was measured and fitted with an exponential fit:

$$n(t) = n_0 \exp\left(-\frac{t - t_0}{\tau}\right) + B \quad (3.19)$$

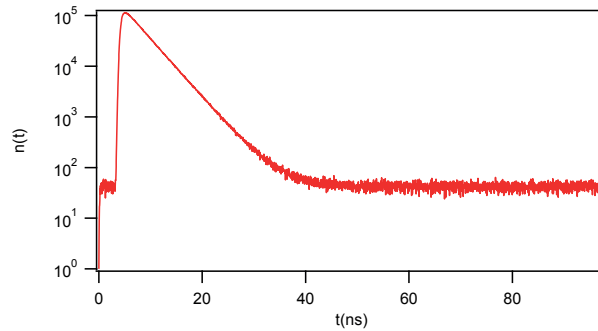


Figure 3.23: Histogram of the arrival times

4 Results and discussion

4.1 Correction collar benchmark

As calculated in section 3.2.2, there is no objective correction collar setting that is perfect for every beam angle. For this reason, we compared several measurement values for the possible correction collar settings to find the best correction collar setting of the objective for every application, and to get a better understanding of the influence of the correction collar on a measurement. Every measurement has been performed with the same sample concentration with varying the correction collar setting from 13 to 19, corresponding to standard borosilicate coverslip glass thicknesses from 130 to 190 μm .

4.1.1 Fret benchmark

First, FRET-measurements of fluorescently labeled dsDNA (see section 3.4.3) have been performed in the bare capillary and with the new arrangement. More events indicate better optics because a smaller focus has a higher power density and is therefore more efficient to excite the dyes. But also the width of the histogram is very important since a very broad histogram will consequently prevent the resolution of different species when the method is applied to heterogeneous samples. These measurements solely serve the purpose to find the optimal correction collar setting for one arrangement and should not be compared with respect to the different arrangements, because different concentrations have been used for the bare capillary and the new arrangement here. A comparison of the different arrangements will follow in section 4.2.

bare capillary: In the bare capillary, the most counts have been measured for the smallest correction collar setting of 13 and it is therefore used in all following measurements in the bare capillary. By increasing the correction collar setting the FRET-histograms show less counts, whereas the width of the histograms remains constant.

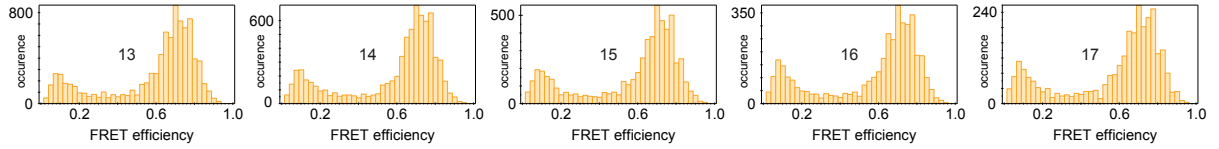


Figure 4.1: Influence of the correction collar for the Alexa Fluor 488/Alexa 594 setup (FRET 1 in figure 3.1) on the bare capillary. FRET measurements with an acceptor/donor channel sum threshold of 30 cts/ms of a dsDNA solution, with increasing correction collar setting from left to right (13-17). Different scaling has been used for every histogram to compare the widths of the histograms

New arrangement: With the new arrangement, a FRET-measurement has been performed with the dsDNA labeled with Alexa488 and Alexa594 and also with the dsDNA labeled with Alexa488 and Atto647N. The best FRET histograms have been measured for a correction collar setting of 16 and 17 because the histograms are symmetric, narrow and show the most counts. With a lower collar setting the histograms show less counts and with a higher setting the histograms broadened and became asymmetric.

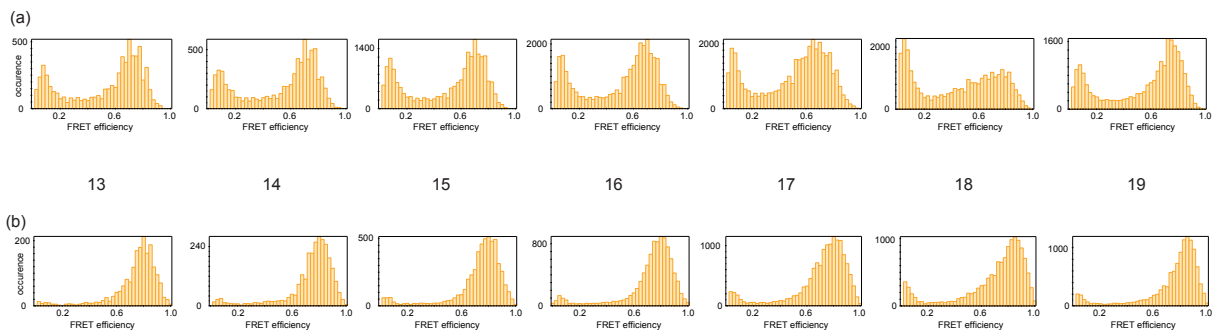


Figure 4.2: Influence of the correction collar for (a) the Alexa Fluor 488/Alexa Fluor 594-setup (FRET 1 in figure 3.1) and (b) the Alexa Fluor 488/Atto647N-setup (FRET 2 in figure 3.1). FRET measurements with an acceptor/donor channel-sum threshold of 30 cts/ms of a 500 pM dsDNA solution, with increasing correction collar setting from left to right (13-19). The samples were excited at a wavelength of 488 nm. Different scaling has been used for every histogram to compare the widths of the histograms

4.1 Correction collar benchmark

To compare the quality of a FRET measurement a quality indicator Q_{FRET} was defined:

$$Q_{FRET} = \frac{\text{number of counts at peak position}}{N \cdot \text{width}} \quad (4.1)$$

where N is the mean number of donor-fluorophores (Alexa 488) in the focal volume, determined from a simultaneous FCS-measurement of the donor channel and *width* is the width of the Gaussian at $\frac{1}{e}$ of the maxima. For the two different dye-couples, respectively setups, a maximal FRET quality indicator has been found at a correction collar setting of 16.

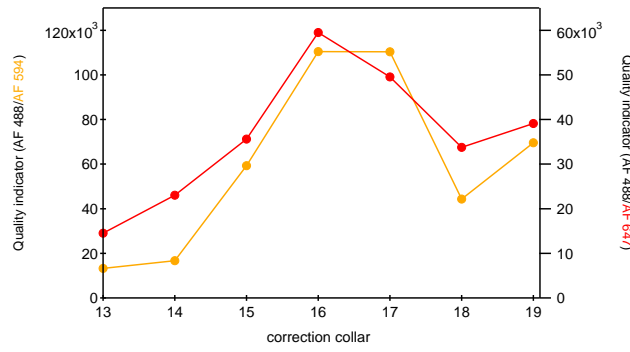


Figure 4.3: Quality indicator of the Alexa Fluor 488/Alexa Fluor 594-setup (FRET 1 in figure 3.1) (orange) and of the Alexa Fluor 488/Atto 647N-setup (FRET 2 in figure 3.1) (red) according to eq. 4.1, against the objective correction collar. The lines are a guide for the eye.

4.1.2 Focal volume benchmark

To explain the differences in the FRET-histograms and to get a better understanding of the influence of the correction collar, two dimensional scans of 100 nm fluorescent microspheres embedded in agarose gel have been performed, varying the correction collar. The beads can nearly be treated as a point source because of their subresolutional size, thus enabling an accurate mapping of the focal volume. As we used Tetraspeck microspheres that fluoresce with the donor and the acceptor wavelength at donor excitation, the focal volume could be imaged in the donor and the acceptor channel, and the focal overlap could be determined. In figure 4.4 and figure 4.5 it can be seen that the focal volumes have a minimum at a collar setting of 17 and the z-shift between the donor and the acceptor focus increases strongly ($> 100\text{ nm}$) for collar settings higher than 16. Whereas the donor foci show the same behavior for the different dye-pairs, the acceptor foci have different volume-minima depending on the setup (Alexa Fluor 488/Alexa Fluor 594-setup or Alexa Fluor 488/Atto647N). This might be a consequence of the different z-shifts, that is influencing the acceptor-focus. The shift between the donor and the acceptor foci in the x-y plane (see Appendix A.4) is negligible ($< 10\text{ nm}$) as expected. Also,

the differences in x-y cross section by changing the correction collar are small compared to the y-z cross section and are therefore not shown (see Appendix A.4).

These findings are in good agreement with the FRET-histograms. They explain why 16 is the best correction collar setting for a multicolor measurement since the focal volume and at the same time the z-shift is small for this setting. Also the broadening of the histograms can be explained by the big z-shift for the higher correction collar settings.

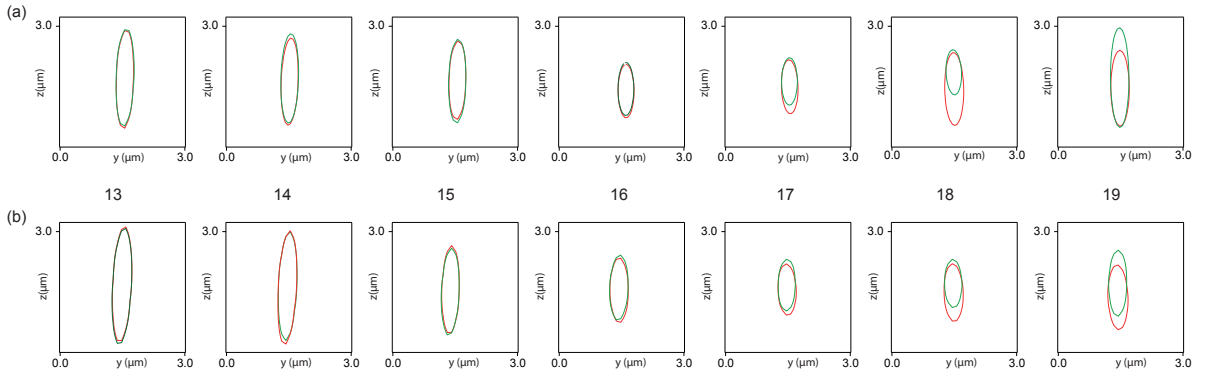


Figure 4.4: Influence of the correction collar (13-19) at the y-z cross section of the focal volume in the donor (green) and the acceptor channel (red) of (a) the Alexa Fluor 488/Alexa Fluor 594-setup (FRET 1 in figure 3.1) and (b) the Alexa Fluor 488/Atto647N-setup (FRET 2 in figure 3.1). The focal volume is defined here as the volume in where the intensity of the fluorescent microsphere is higher than $1/e^2$ of the maximal Intensity. The sample was excited with a laser power of 300 nW at a wavelength of 488 nm.

4.1 Correction collar benchmark

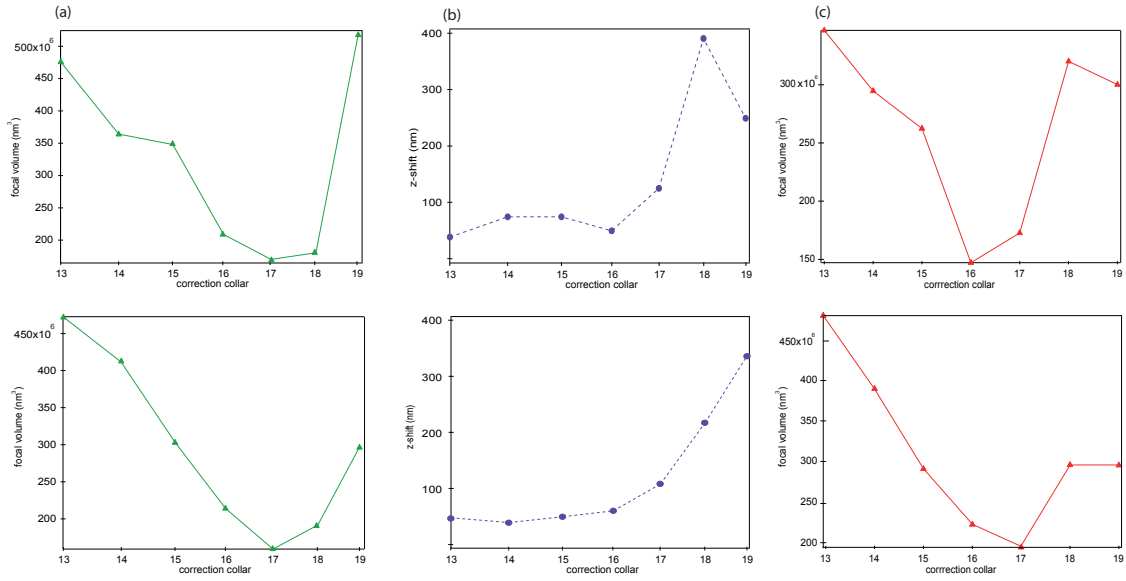


Figure 4.5: Influence of the correction collar at: (a) the donor focal volume (b) z-shift of the acceptor focal position compared to the donor focal position (c) the acceptor focal volume. The fluorescent spheres were excited with the donor excitation wavelength of 488 nm. The upper row was measured with the Alexa Fluor 488/Alexa Fluor 594-setup (FRET 1 in figure 3.1), and the lower row with the Alexa Fluor 488/Atto 647N-setup (FRET 2 in figure 3.1). Lines: guide for the eye.

4.1.3 FCS benchmark

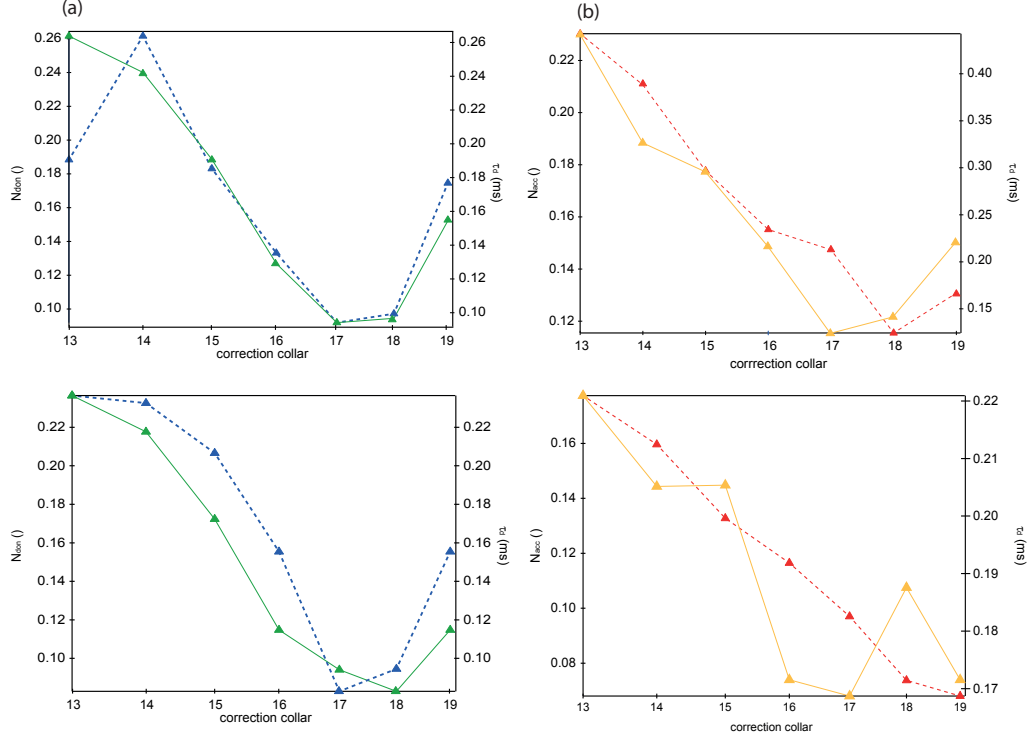


Figure 4.6: Influence of the correction collar at: (a) the mean number (green, line) and diffusion time (blue, dotted) of fluorescent donor-molecules (Alexa 488) in the focal volume (b) the mean number (orange, line) and diffusion time (red, dotted) of fluorescent acceptor-molecules (Alexa 594/Atto647N) in the focal volume. The data of the upper row has been determined of an FCS-measurement of dsDNA labeled with Alexa488 and Alexa 594 (Setup: FRET 1 in figure 3.1), and data of the lower row by an FCS-measurement of dsDNA labeled with Alexa488 and Atto 647N (Setup: FRET 2 in figure 3.1). Lines: guide for the eye.

A triplet saturation measurement (see section 4.2.1) would have been really laborious for every correction collar setting and the different laser powers. Over 200 correlation curves would have to be measured, so FCS measurements have been performed only for a laser power of 40 μW . From the autocorrelation of the previously performed FRET-measurements of two differently labeled dsDNA samples (Alexa 488/Alexa 594 and Alexa 488/Atto647N), the average number of molecules in the focal volume N and the diffusion time τ_d was determined by fitting the donor-and the acceptor-autocorrelation functions of the corresponding setups. The donor-measurements are in good agreement to the focal volume measurement where the smallest focal volume corresponded to a correction collar of 17: The diffusion time τ_d and

the average number of molecules in the focal volume N have a minimum at the correction collar setting of 17. The acceptor-measurements show a peculiar behavior: Albeit N and τ_d of the donor channel are pretty similar, the curves are different in the acceptor channel. This is probably because the z-shift between the acceptor and the donor focus has to be considered here. Perhaps the z-shift leads to different effects for the average number of molecules in the focal volume N and the diffusion time τ_d .

4.1.4 Discussion

The focal volume (figure 4.5) and also the mean number of molecules and the diffusion time (figure 4.6) are with a few exceptions the smallest for a correction collar of 17, hence this setting is optimal for single color experiments since the focus shift does not matter. According to figure 4.3, an objective correction collar of 16 turned out to be the optimal setting and was used for all following two color measurements with the new arrangement. Here, the focus shift (see figure 4.5b) is really important, leading to a different optimal correction collar than for a single color experiment. Hence for FRET and also for other dual-color methods like for example fluorescence cross-correlation (FCCS) [123] the optimal correction collar is 16.

For the coverslip an objective correction collar setting of 15 was used according to the coverslip thickness of 150 μm , whereas for the bare capillary the best results have been found for a setting of 13 (see figure 4.1).

4.2 Comparison of the coverslip, the bare capillary and the new arrangement

In this section, benchmark measurements with the new arrangement, the capillary immersed in an index matching liquid on a fused silica coverslip, are compared to measurements with the bare capillary and on a coverslip.

4.2.1 FCS benchmark

For an evaluation of the focusing conditions of single color experiments in our optical arrangement, we used a correction collar setting of 17 and performed excitation benchmarks by means of FCS varying the excitation power for the three different arrangements. The apparent inter-system crossing rate that can be extracted from these measurements reports on the saturation behavior of the dye molecules, thus providing information on the excitation intensity (see section 2.3). The excitation intensity is the excitation power relative to the illuminated area. A

lower saturation power corresponds to a smaller excitation focus. In the upper three panels of figure 4.7, the saturation curves for the three used dyes are shown for the three experimental setups, the coverslip as the reference (squares), the bare capillary (circles), and the capillary on top of a silica coverslip (our new arrangement, triangles). For all three dyes, the saturation curve of the bare capillary is clearly below the coverslip reference as expected because of significant optical aberrations. Our new arrangement, on the other hand, compares well with the coverslip reference. The slightly better performance of the new arrangement as compared to the coverslip reference might be explained by a non-perfect setting of the correction collar in the coverslip measurements.

4.2 Comparison of the coverslip, the bare capillary and the new arrangement

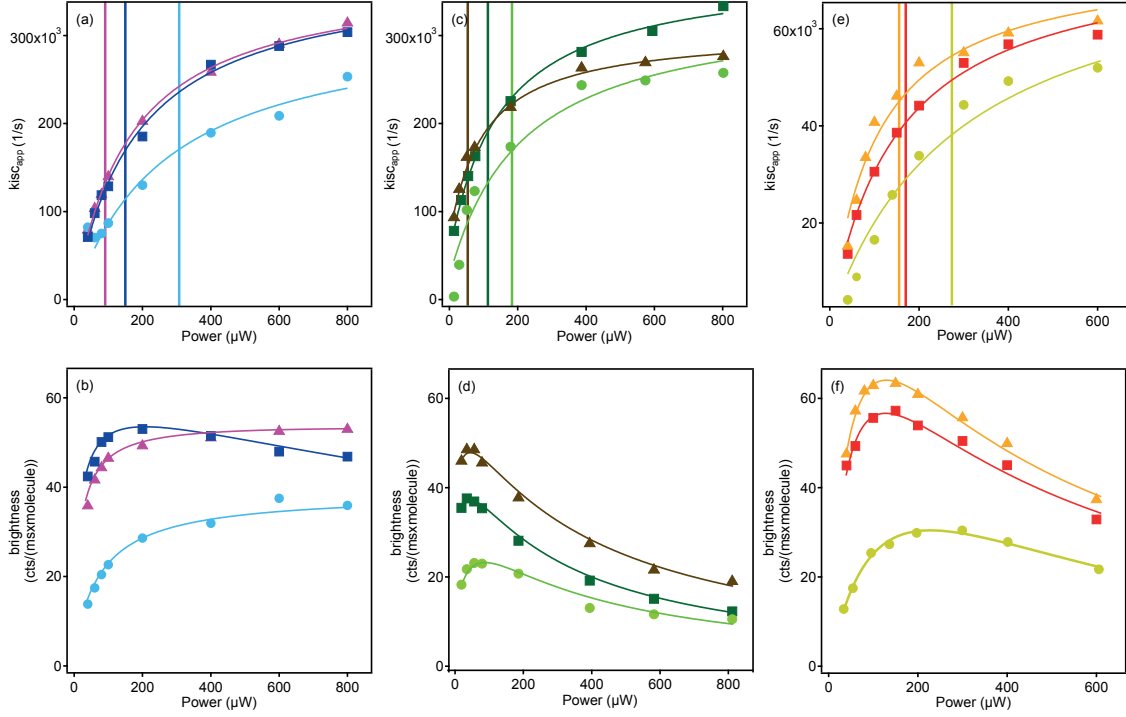


Figure 4.7: (a) excitation and (b) detection benchmark of a 1 nM Alexa Fluor 488 solution on a borosilicate coverslip (blue rectangles), in the capillary (cyan circles), and with the new arrangement (magenta triangles). Alexa Fluor 488 was excited at a wavelength of 488 nm. (c) Excitation and (d) detection benchmark of a 1 nM DNA/Alexa Fluor 594 solution on a borosilicate coverslip (green rectangle), in the capillary (green circle), and with the new arrangement (brown triangle). (e) Excitation and (f) detection benchmark of a 1 nM DNA/Atto 647N solution on a borosilicate coverslip (red rectangle), in the capillary (green circle), and with the new arrangement (orange triangle). Atto 647N and Alexa Fluor 594 were attached to dsDNA that also carried an Alexa Fluor 488 label that was not excited in the experiment carried out with a 594 nm (c,d) and a 640 nm (e,f) laser. The saturation powers result from fits according to eq. 3.10 (solid curves) and can be found in table 11. The molecular brightness was calculated according to eq. 3.11, fitted according to eq. 3.12 and the results can also be found in table 11.

While the apparent intersystem crossing rate is an indicator of the excitation conditions, the detection efficiency can be evaluated by inspection of the molecular brightness shown in the lower three panels in figure 4.7. As for the excitation, the detection efficiency (see table 11) is similar for the coverslip and for the new arrangement, while it is significantly lower for the bare capillary. Interestingly, also the slightly better performance of the new arrangement as compared to the coverslip reference is reproduced for Alexa 594 and Atto 647N. The course

4.2 Comparison of the coverslip, the bare capillary and the new arrangement

of the molecular brightness as a function of the laser power has been fitted with a four-level system according to eq. 3.12. The saturation levels of the different fluorophores were consistent respectively within the measurement error for the measurement on the coverslip and with the new arrangement, whereas the saturation levels of the measurement with the bare capillary were much higher, had a higher fit error and did not always coincide within measurement error.

Table 11: Results of the fluorescence correlation spectroscopy benchmark: saturation power P_{sat} , molecular brightness $\beta_{40\mu W}$ at a laser power of $40\mu W$, detection efficiency η_D and the saturation levels ϕ_{S1} and ϕ_{S2} . ϕ_{S1} corresponds to the absorption of one photon, whereas ϕ_{S2} corresponds to the consecutive absorption of two photons.

Alexa Fluor 488	coverslip	capillary	new arrangement
$P_{sat}(\mu W)$	150 ± 14	307 ± 80	103 ± 16
$\beta_{40\mu W}(\frac{cts}{ms \cdot fl})$	42.42	13.83	35.82
$\eta_D(\%)$	2.12 ± 0.20	0.3367 ± 0.0024	1.74 ± 0.14
$\phi_{S1}(\frac{ph}{m^2 \cdot s})$	$(1.14 \pm 0.13) \cdot 10^{26}$	$(4.5 \pm 3.2) \cdot 10^{26}$	$(1.22 \pm 0.13) \cdot 10^{26}$
$\phi_{S2}(\frac{ph}{m^2 \cdot s})$	$(1.75 \pm 0.13) \cdot 10^{54}$	$(8 \pm 10500) \cdot 10^{57}$	$(42 \pm 80) \cdot 10^{54}$
Alexa Fluor 594	coverslip	capillary	new arrangement
$P_{sat}(\mu W)$	119 ± 05	179 ± 45	69 ± 04
$\beta_{40\mu W}(\frac{cts}{ms \cdot fl})$	36.34	19.49	46.61
$\eta_D(\%)$	2.08 ± 0.33	0.61 ± 0.14	3.32 ± 0.90
$\phi_{S1}(\frac{ph}{m^2 \cdot s})$	$(1.19 \pm 0.25) \cdot 10^{26}$	$(3.0 \pm 1.2) \cdot 10^{26}$	$(0.87 \pm 0.29) \cdot 10^{26}$
$\phi_{S2}(\frac{ph}{m^2 \cdot s})$	$(0.212 \pm 0.028) \cdot 10^{54}$	$(0.59 \pm 0.10) \cdot 10^{54}$	$(0.207 \pm 0.048) \cdot 10^{54}$
Atto 647N	coverslip	capillary	new arrangement
$P_{sat}(\mu W)$	182 ± 13	272 ± 43	164 ± 07
$\beta_{40\mu W}(\frac{cts}{ms \cdot fl})$	44.96	16.34	47.56
$\eta_D(\%)$	0.389 ± 0.050	0.0992 ± 0.0059	0.4041 ± 0.0026
$\phi_{S1}(\frac{ph}{m^2 \cdot s})$	$(3.77 \pm 0.85) \cdot 10^{26}$	$(9.82 \pm 1.37) \cdot 10^{26}$	$(4.33 \pm 0.52) \cdot 10^{26}$
$\phi_{S2}(\frac{ph}{m^2 \cdot s})$	$(1.076 \pm 0.093) \cdot 10^{54}$	$(4.10 \pm 0.28) \cdot 10^{54}$	$(1.098 \pm 0.047) \cdot 10^{54}$

4.2.2 Focal volume benchmark

For an evaluation of the focusing conditions of two color experiments in the new arrangement we used a correction collar setting of 16. In figure 4.8 a and 4.9 a the cross sections of the focal volume in the x-y and the y-z plane are shown for the acceptor (left) and the donor channel (right), measured with donor excitation.

4.2 Comparison of the coverslip, the bare capillary and the new arrangement

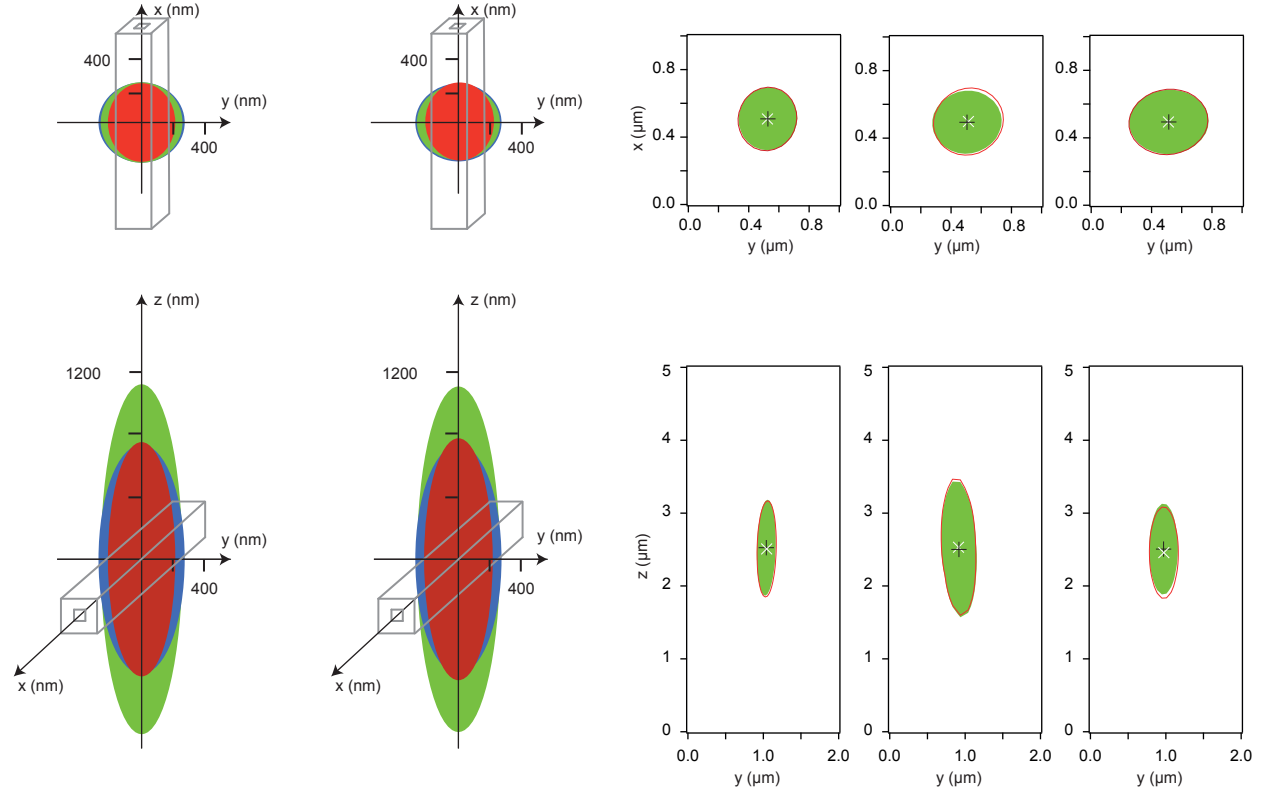


Figure 4.8: (a) Dimensions of the focal volume of the setup for the FRET-measurement of the Alexa Fluor 488/Alexa Fluor 594-dyes (FRET 1 in figure 3.1) of the borosilicate coverslip (red), the capillary (green) and the new arrangement (blue) in the acceptor (left) and the donor channel (right). Top panels: cross section in the x-y plane of the focal volume. Bottom panels: cross section in the y-z plane of the focal volume. (b) Focal overlap of the acceptor (red) and the donor (green) channel on the borosilicate coverslip (left), the capillary (center) and the new arrangement (right). Top panels: x-y plane of the focal overlap. Bottom panel: y-z plane of the focal overlap. For details see tab.12. The fluorescent spheres were excited with a laser power of 300 nW at a wavelength of 488 nm.

4.2 Comparison of the coverslip, the bare capillary and the new arrangement

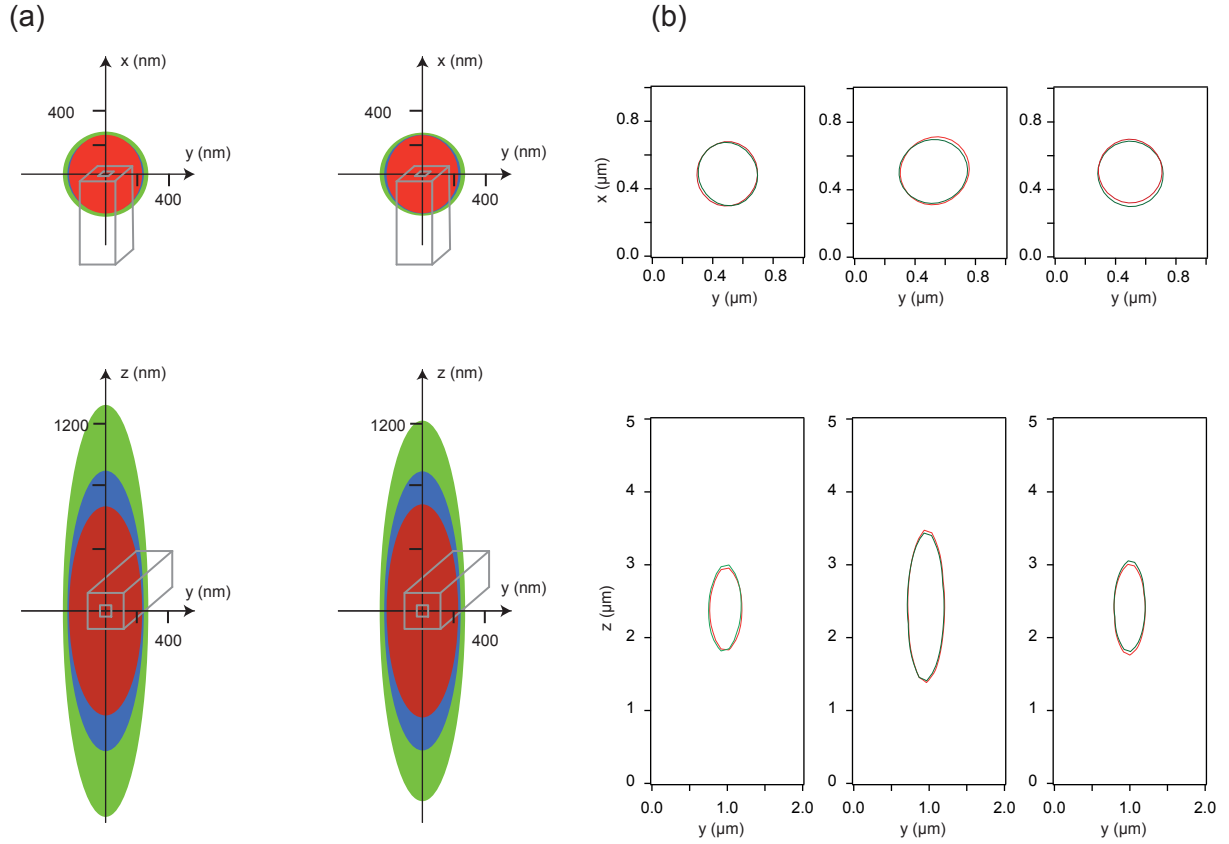


Figure 4.9: (a) Dimensions of the focal volume of the setup for the FRET-measurement of the Alexa Fluor 488/Atto 647N-dyes (FRET 2 in figure 3.1) of the borosilicate coverslip (red), the capillary (green) and the new arrangement (blue) in the acceptor (left) and the donor channel (right). Top panels: cross section in the x-y plane of the focal volume. Bottom panels: cross section in the y-z plane of the focal volume. (b) Focal overlap in the acceptor (red) and the donor (green) channel on the borosilicate coverslip (left), the capillary (center) and the new arrangement (right). Top panels: x-y plane. Bottom panel: y-z plane. For details see tab.12. The fluorescent spheres were excited with a laser power of 300 nW at a wavelength of 488 nm

Interestingly, the different setups for the different acceptor fluorophores (figure 4.8 : Alexa594; figure 4.9: Atto647N) delivered different donor foci. For example, the donor focal volume of the new arrangement, in comparison to the donor coverslip focus, is enlarged in y-direction for the Af488/Af594 setup, whereas for the Af488/Atto647N setup it is enlarged in z-direction. The reasons for this remarkable behavior are not yet identified. Possible reasons are the different filters and dichroics for the two setups but mainly the precision of the two dimensional scans could be not appropriate for the application, even small movements of the microspheres during a scan can lead to deviations. Three dimensional scans would lead to

4.2 Comparison of the coverslip, the bare capillary and the new arrangement

better, more trustworthy results. However, what we can state is that the focus in the bare capillary (green) is significantly enlarged in comparison to the coverslip focus (red) and with the new arrangement (blue) the focal volume can be improved but does not reach the size of the coverslip focus.

In figure 4.8 b and 4.9 b, the focal overlap of the donor (green) and the acceptor (red) emission foci can be seen. Here we can trust the results because both, the acceptor and the donor channel, have been scanned simultaneously. The focal overlap in the x-y plane (upper row) is almost perfect and the shift in x and y is smaller than 10 nm for all arrangements. In contrast, the acceptor focus is shifted up to 39 nm in z-direction with respect to the donor focus with the bare capillary and even 60 nm with the new arrangement (for z-shift values see table 12).

Concluding, a not perfectly matched refractive index in combination with an imperfect shape of the square capillary leads to a focus enlargement and a shift of the acceptor focus in z-direction. With the new arrangement the enlargement can be reduced at the expense of an increasing z-shift of the acceptor focus position compared to the donor focus position.

Table 12: Results of the fluorescent microsphere benchmark of the different setups FRET 1 and FRET 2 (see figure 3.1): x-, y- and z-diameter of the focal volume in the acceptor channel $\omega_{x,y,z}^{acc}$ and in the donor channel $\omega_{x,y,z}^{don}$ and z-shift dz_0 of the acceptor focus compared to the donor focus . An error of 10% was estimated for the precision of the diameters.

FRET1: 488/594	coverslip	capillary	new arrangement
$\omega_x^{acc}(\text{nm})$	504 ± 50	516 ± 52	516 ± 52
$\omega_y^{acc}(\text{nm})$	432 ± 43	524 ± 52	544 ± 54
$\omega_z^{acc}(\text{nm})$	1500 ± 150	2243 ± 224	1468 ± 147
$\omega_x^{don}(\text{nm})$	500 ± 50	501 ± 50	500 ± 50
$\omega_y^{don}(\text{nm})$	440 ± 44	532 ± 53	543 ± 54
$\omega_z^{don}(\text{nm})$	1551 ± 155	2215 ± 222	1464 ± 146
$dz_0(\text{nm})$	17.2 ± 3.7	30.6 ± 3.2	49.5 ± 4.4
FRET2: 488/647	coverslip	capillary	new arrangement
$\omega_x^{acc}(\text{nm})$	504 ± 50	546 ± 55	493 ± 49
$\omega_y^{acc}(\text{nm})$	469 ± 47	548 ± 55	490 ± 49
$\omega_z^{acc}(\text{nm})$	1341 ± 134	2496 ± 250	1798 ± 180
$\omega_x^{don}(\text{nm})$	500 ± 50	532 ± 53	506 ± 51
$\omega_y^{don}(\text{nm})$	459 ± 46	548 ± 55	490 ± 49
$\omega_z^{don}(\text{nm})$	1367 ± 137	2440	1789 ± 179
$dz_0(\text{nm})$	17.6 ± 3.1	38.5 ± 5.4	60.2 ± 2.6

4.2.3 FRET benchmark

a) Measurement of the same sample

As a more application oriented and direct two color benchmark, a FRET-measurement of dsDNA was performed in all three arrangements for the two dye-couples. In this section, the same sample has been used for all measurements. The differences between the capillary-measurements are small and the FRET-histograms of the bare capillary and the new arrangement are a little bit worse than on a coverslip (see figure 4.10a and figure 4.11a).

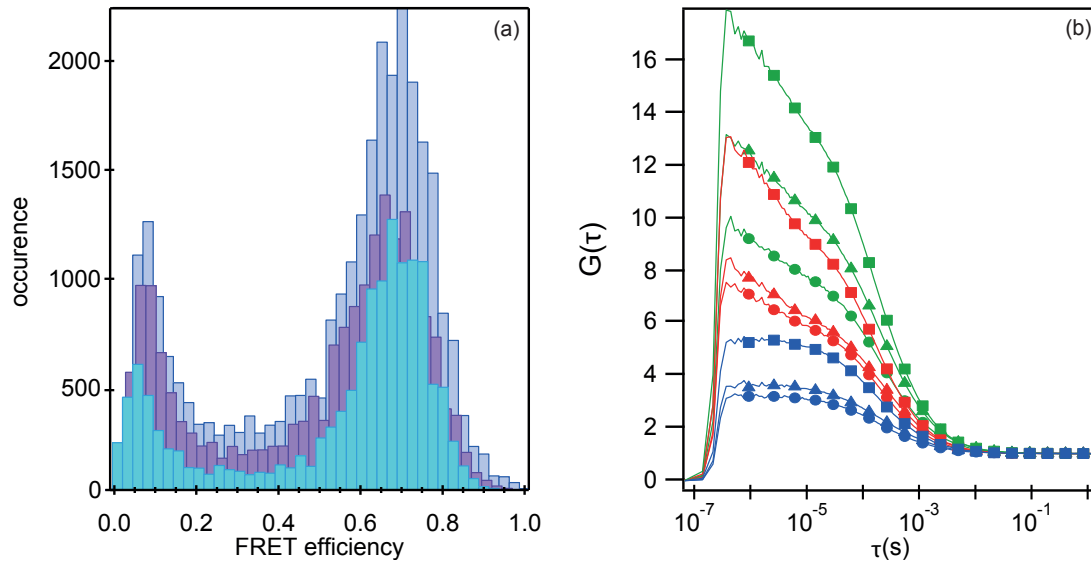


Figure 4.10: (a) Benchmark of FRET measurements of dsDNA labeled with Alexa Fluor 488 and Alexa Fluor 594 dissolved in buffer, on a borosilicate coverslip ($E=0.7008 \pm 0.0028$, width= 0.1069 ± 0.0042 , blue), with the new arrangement ($E=0.6626 \pm 0.0047$, width= 0.1282 ± 0.0087 , purple) and in the capillary ($E=0.6488 \pm 0.0069$, width= 0.126 ± 0.013 , cyan). The fluorophores were excited with a laser power of $40 \mu\text{W}$ at a wavelength of 488 nm. (b) FCS-Measurement of the same samples. Donor-autocorrelation (green), Acceptor-autocorrelation (red) and Donor-Acceptor-crosscorrelation (blue) on a coverslip (rectangles), in the capillary (circles) and with the new arrangement (triangles).

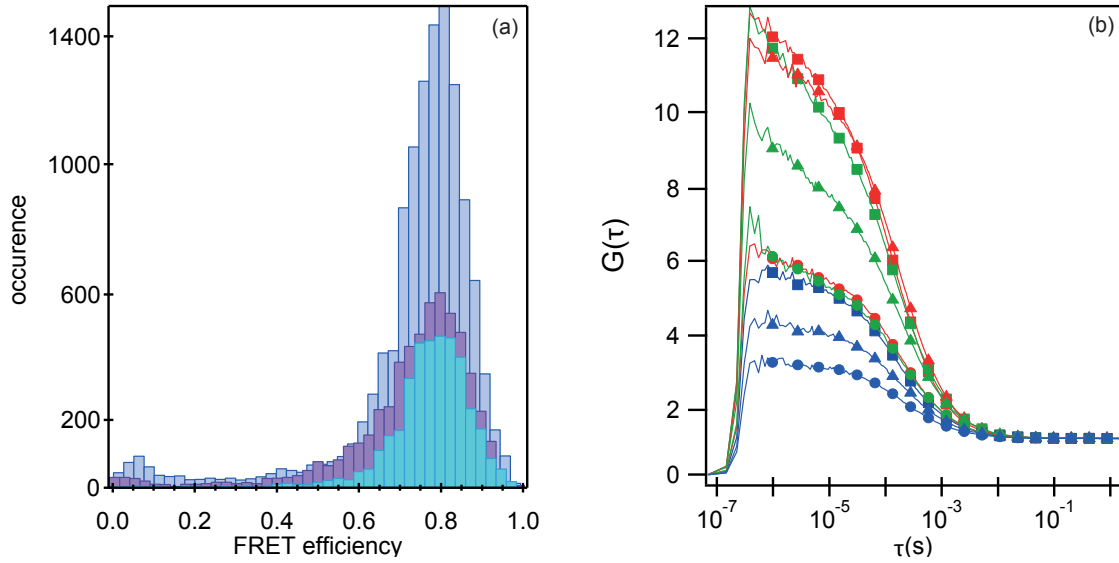


Figure 4.11: (a) Benchmark of FRET measurements of a dsDNA solution labeled with Alexa Fluor 488 and Atto 647N, on a borosilicate coverslip ($E=0.7778 \pm 0.0023$, width= $0,1096 \pm 0,0023$, blue), with the new arrangement ($E=0.7694 \pm 0.0034$, width= $0,1315 \pm 0,0054$, purple) and in the capillary ($E=0.7689 \pm 0.0023$, width= $0,1118 \pm 0,0035$, cyan). The fluorophores were excited with a laser power of 40 μ W at a wavelength of 488 nm. (b) FCS-Measurement of the same samples. Donor-autocorrelation (green), Acceptor-autocorrelation (red) and Donor-Acceptor-crosscorrelation (blue) on a coverslip (rectangles), in the capillary(circles) and with the new arrangement (triangles).

But appearances are often deceiving, unfortunately the difference is only that small because of the bigger focal volumes in the bare capillary and with the new arrangement (see section 4.2.2) compared to the coverslip. For this reason, a FCS-measurement shows that the amplitude of the donor correlation curves (see figure 4.10a and figure 4.11b) are lower of the capillary measurements. This corresponds to a higher number of average number of molecules in the focus, leading to much better histograms. A comparison of the different arrangements with the same sample concentration is not reasonable.

For example, the contradictory result is measured that the arrangement with the most molecules in the focus, the bare capillary (cyan), has the lowest histogram. The FRET-histogram of the new arrangement (purple) shows a marginal increase in counts and the coverslip with the least average number of molecules in the focus, the coverslip (blue), has the most fret-events.

b) Measurement with the same mean number of donor molecules in the focal volume

For this reason the concentrations of the measurement samples have been adapted in a way, that the mean number of donor-fluorophores in the focal volume are the same for all three arrangements. This can be seen in the accompanying correlation curves (figure 4.12b and figure 4.13b), where the green donor correlation curves have the same amplitude for all three arrangements. For this reason, the sample of the coverslip measurement has been reduced for the new arrangement, and it had to be even more reduced for the bare capillary because of the even bigger focal volume. The number of events at the peak position, the value of the FRET-efficiency and the width of the Gaussian peak are the most important values for a comparison and can be found in table 13. If we take a look at the number of events for the FRET-measurement of dsDNA labeled with Alexa 488 and Alexa 594 (figure 4.12a) and for dsDNA labeled with Alexa 488 and Atto647N (figure 4.13a) the new arrangement (purple) can improve the much worse results from the measurement in a bare capillary (cyan) but is still far away from the measurement quality on a coverslip (blue). The width of the FRET-histograms is slightly increased with the new arrangement and the bare capillary, whereas the peak position, i.e. the FRET-efficiency, is in good agreement for all FRET measurements.

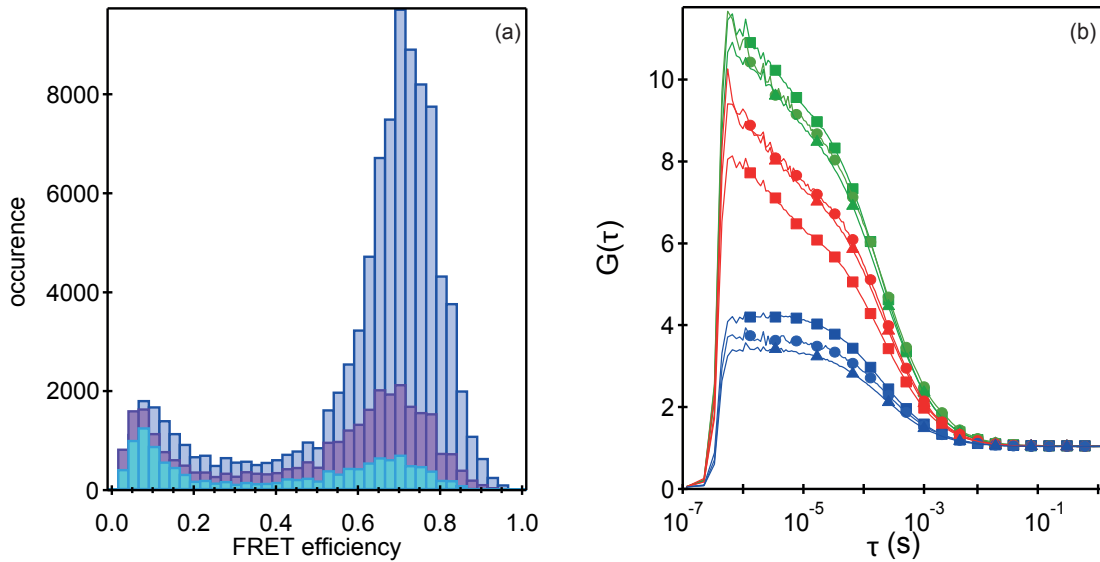


Figure 4.12: (a) Benchmark of FRET measurements of dsDNA labeled with Alexa Fluor 488 and Alexa Fluor 594 dissolved in buffer, on a borosilicate coverslip (blue), with the new arrangement (purple) and in the capillary (cyan). The fluorophores were excited with a laser power of 40 μ W at a wavelength of 488 nm. (b) FCS-Measurement of the same samples. Donor-autocorrelation (green), Acceptor-autocorrelation (red) and Donor-Acceptor-crosscorrelation (blue) on a coverslip (rectangles), in the capillary (circles) and with the new arrangement (triangles).

4.2 Comparison of the coverslip, the bare capillary and the new arrangement

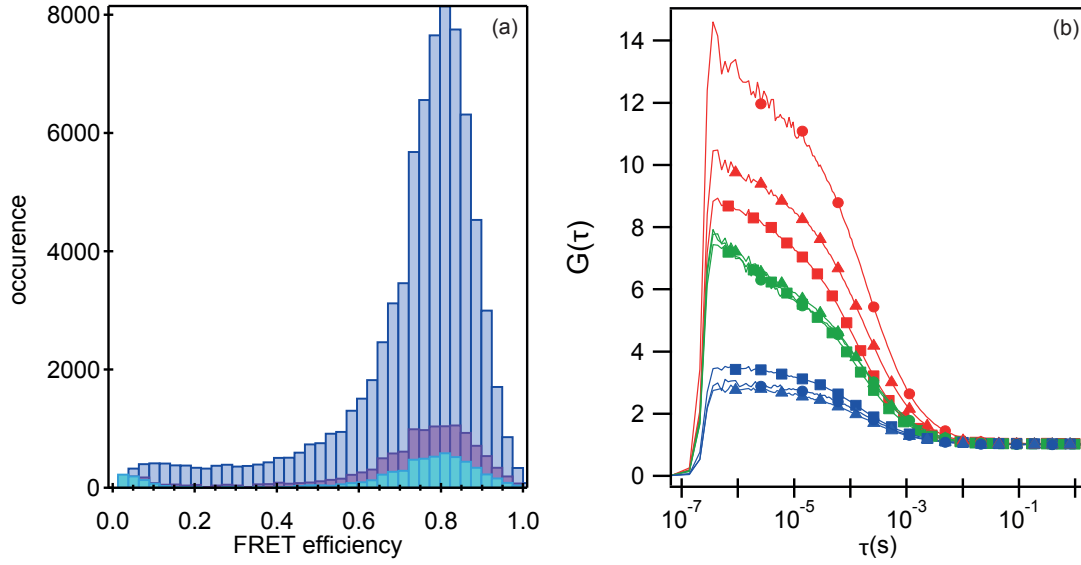


Figure 4.13: (a) Benchmark of FRET measurements of a dsDNA solution labeled with Alexa Fluor 488 and Atto 647N, on a borosilicate coverslip (blue), with the new arrangement (purple) and in the capillary (cyan). The fluorophores were excited with a laser power of 40 μ W at a wavelength of 488 nm. (b) FCS-Measurement of the same samples. Donor-autocorrelation (green), Acceptor-autocorrelation (red) and Donor-Acceptor-crosscorrelation (blue) on a coverslip (rectangles), in the capillary (circles) and with the new arrangement (triangles).

Table 13: Results of the FRET-benchmark: FRET-efficiency E , width of the Gaussian peak $width$, number of events at the peak position $occurrence$ and quality indicator Q_{FRET} (see equation 4.1)

dsDNA (AF488/AF594)	coverslip	capillary	new arrangement
E	0.7008 ± 0.0028	0.6488 ± 0.0069	0.664 ± 0.012
$width$	0.1069 ± 0.0043	0.126 ± 0.013	0.120 ± 0.017
$occurrence$	8711	536	1698
Q_{FRET}	680000	35000	118000
dsDNA (AF488/Atto647N)	coverslip	capillary	new arrangement
E	0.7778 ± 0.0023	0.7689 ± 0.0023	0.7694 ± 0.0034
$width$	0.1096 ± 0.0036	0.1118 ± 0.0035	0.1315 ± 0.0054
$occurrence$	7596	259	1039
Q_{FRET}	347000	12000	40000

c) fused silica coverslip To find out how much the capillary material fused silica is responsible for the worsening of the measurement quality, a Fret measurement on a borosilicate coverslip has been compared to a measurement on a fused silica coverslip. We used a 200

μm fused silica coverslip (Heraeus, Hanau Germany), where we found the best results using a correction collar of 15. The same sample concentration has been used for the two measurements.

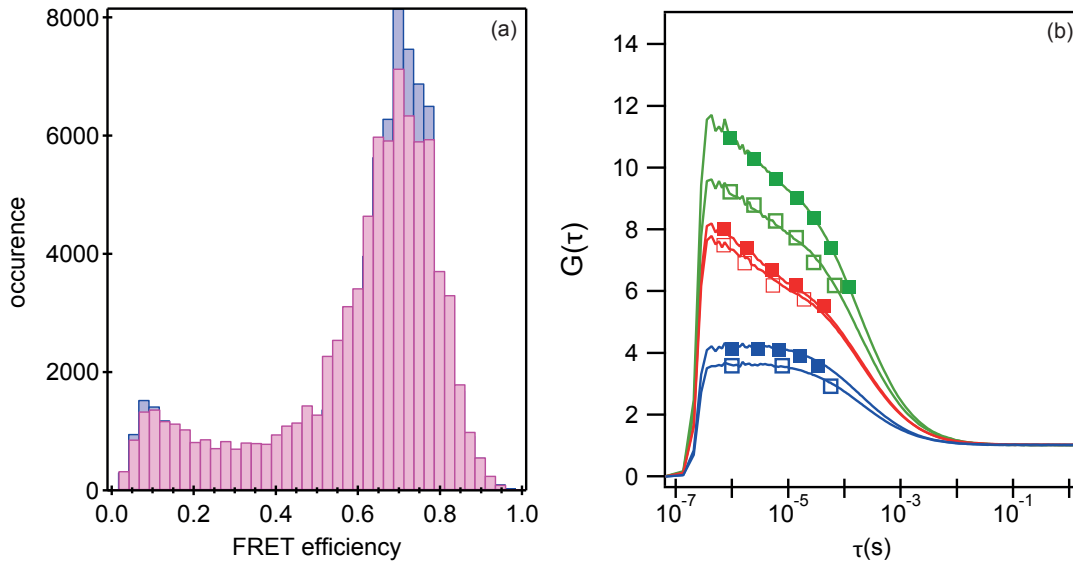


Figure 4.14: (a) Benchmark of FRET measurements of a dsDNA solution labeled with Alexa Fluor 488 and Alexa 594, on a borosilicate coverslip (blue) and on a fused silica coverslip (pink). The fluorophores were excited with a laser power of $40 \mu\text{W}$ at a wavelength of 488 nm. (b) FCS-Measurement of the same samples. Donor-autocorrelation (green), Acceptor-autocorrelation (red) and Donor-Acceptor-crosscorelation (blue) on a borosilicate coverslip (filled rectangles) and on a fused silica coverslip (open rectangles).

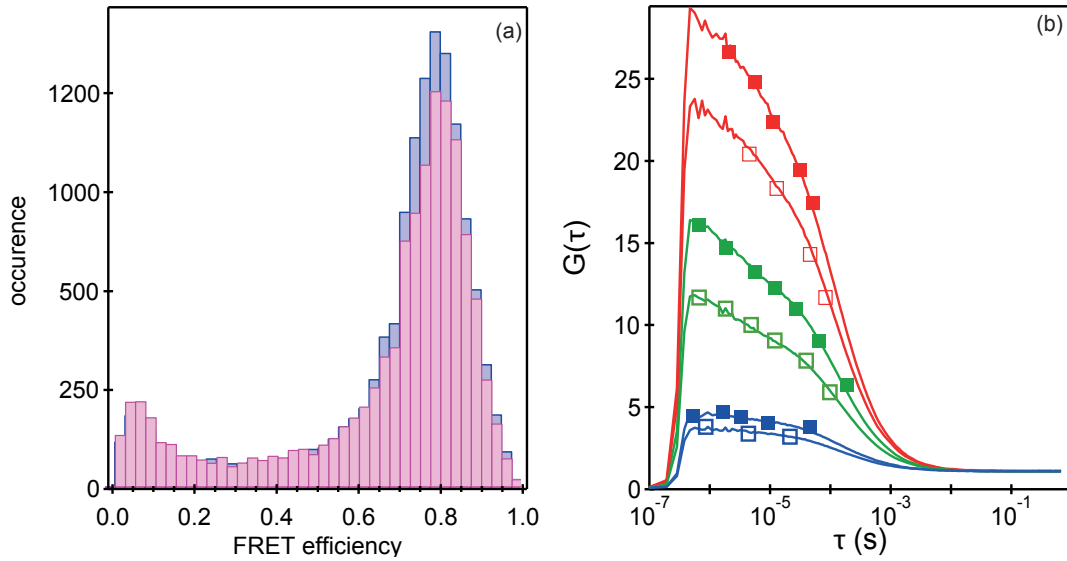


Figure 4.15: (a) Benchmark of FRET measurements of a dsDNA solution labeled with Alexa Fluor 488 and Atto 647N, on a borosilicate coverslip (blue) and in on a fused silica coverslip (pink). The fluorophores were excited with a laser power of 40 μ W at a wavelength of 488 nm. (b) FCS-Measurement of the same samples. Donor-autocorrelation (green), Acceptor-autocorrelation (red) and Donor-Acceptor-crosscorelation (blue) on a borosilicate coverslip (filled rectangles) and on a fused silica coverslip (open rectangles)

Comparing the FRET histograms and the autocorrelation curves it can be seen that the FRET measurement quality is also worse on a fused silica coverslip. By measuring on a borosilicate coverslip, we get more FRET-events from less molecules in the focal volume. However, we can conclude that the material is not the only reason for the worse measurement quality in the fused capillary since the results here are better than with the new arrangement (for a better comparison see figure 5.2 in the conclusion).

4.2.4 Discussion

For a single color experiment good results have been achieved for the new arrangement with the correction collar setting 17. The excitation and detection quality is much better than with the bare capillary and comparable to a measurement on a coverslip (see figure 4.7).

With the correction collar setting 16 for two color experiments, the focal volume of a coverslip measurement could not be achieved but with the new arrangement a smaller focal volume than in the bare capillary has been achieved (see figure 4.8 a and figure 4.9 a). There is a spectral shift for the focal volume position, so the acceptor focus is shifted respective to the donor focus in z-direction (see figure 4.8 b and figure 4.9 b). This is the reason for worse results

for two color experiments like FRET: With the new arrangement the FRET-measurement could be improved but is not as good as on a coverslip (see figure 4.12 and figure 4.13) The material of the capillary, fused silica, is one of the reasons for the worse measurement-quality of two-color experiments (see figure 4.14 and figure 4.15). Additionally, non-flat surfaces of the capillary (see figure 3.3) lead to optical aberrations.

4.3 Pressure evaluation

The glue procedure has been optimized and the glue connection is stable up to 2000 bar. Despite all efforts to also optimize the handling routine and best care and attention, the fused silica capillary can hold pressure of 2000 bar roughly with a 50% chance. The stability of the capillary at 1500 bar is guaranteed with a chance of about 80% and a stability at 1000 bar can be guaranteed for every experiment. These values are estimated from the experiences, made during the pressure fluorescence experiments performed in this work. Even alternative techniques, than the flame of propane blowtorch, to remove the protection layer for the observation window have been tried. With a high-power laser carried out by Norbert Koop (Institut of Biomedical Optics, Lübeck) the protection layer was burned away. Besides that it was not a really clean method, because it was also influencing the surface of the capillary glass, the pressure stability was not improved. Removing the protection layer with acid sulfur, is much cleaner but also very laborious because of the highly acidic substance that also has to be removed afterwards. This procedure neither led to a better pressure stability.

Fluorescence lifetime measurement at high pressure: An application of a fluorescence measurement in fused silica capillaries, is to perform fluorescence measurements under pressure. As a first pressure test, we measured the fluorescence lifetime of Alexa 488 at varying pressure conditions. The results are shown in figure 4.16 a) and are in good agreement with the literature [56]. For an increase of pressure of 2 kbar a decrease of the fluorescence lifetime of 3% is expected. This change of fluorescence lifetime has been confirmed for Alexa 488 by the lifetime measurement and thereby confirms the pressure reading of the manometer. Also the pressure dependent fluorescence lifetime of Atto 647N has been investigated. The pressure dependency with a decrease of more than 4% for an increase of 2 kbar is higher. There is no report on the pressure dependent fluorescence lifetime of this dye in the literature.

4.3 Pressure evaluation

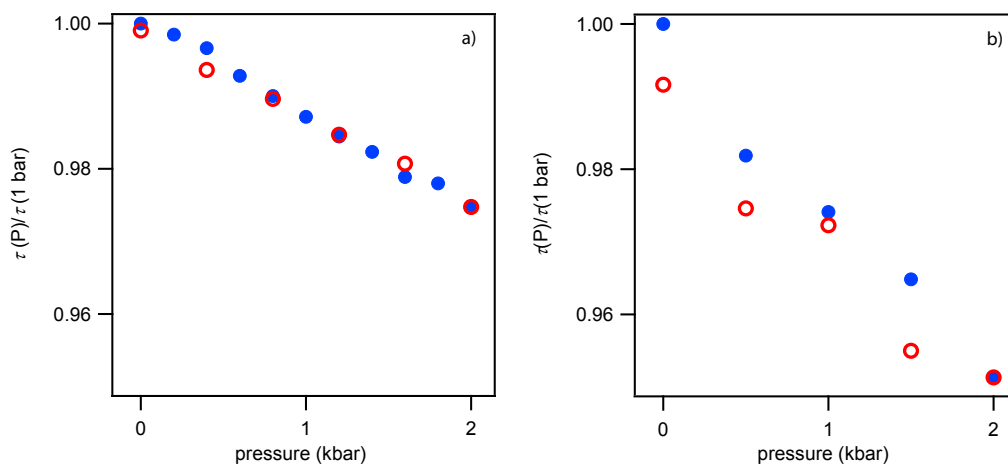


Figure 4.16: Normalized fluorescence lifetime of 1 μM (a) Alexa Fluor 488 and (b) Atto 647N as a function of increasing pressure (filled circles, blue) and decreasing pressure (open circles, red). The fluorophores were excited with 100 nW laser power at a wavelength of 470 nm with 100 ps pulses at a repetition rate of 10 MHz and 635 nm with 400 ps pulses at a repetition rate of 4 MHz.

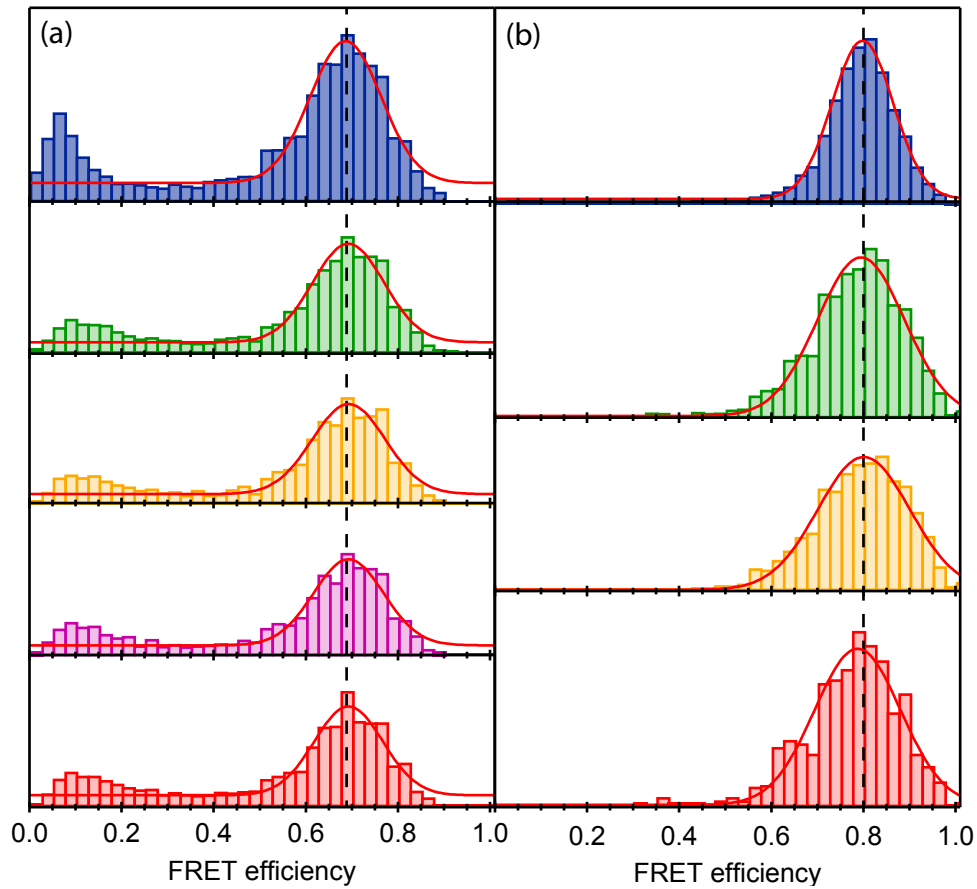


Figure 4.17: (a) Pressure dependence of FRET measurements of a 500 pM dsDNA solution labeled with Alexa Fluor 488 and Alexa Fluor 594 at different pressures: 1 bar on a coverslip (blue), 1 bar in the capillary (green), 300 bar in the capillary (yellow), 600 bar in the capillary (magenta) and 900 bar in the capillary (red). (b) Pressure dependence of FRET measurements of a 500 pM dsDNA solution labeled with Alexa Fluor 488 and Atto 647N at different pressures: 1 bar on a coverslip (blue), 1 bar in the capillary (green), 1000 bar in the capillary (yellow) and 2000 bar in the capillary (red).

FRET measurement under pressure: A next approach was a single molecule FRET measurement under pressure to exclude pressure artifacts on FRET-measurements. Therefore the pressure stable dsDNA labeled with the fluorophores Alexa 488 and Alexa 594 (figure 4.17 a) and with Alexa 488 and Atto 647 (figure 4.17b) respectively, have been investigated under pressure. Not surprisingly pressure has no influence on the FRET-histograms of the two samples. The FRET-efficiency and the width of the Gaussian fit stays constant with increasing pressure (see table 14). Whereas the width of the Gaussian fit is comparable to the coverslip measurement for the dsDNA labeled with Alexa 488 and Alexa594, the histogram is slightly broader for the measurement of the dsDNA labeled with Alexa 488 and Alexa 647N. It should

4.4 Temperature evaluation

be noted that this was not the case in the FRET-benchmark (see section 4.2.3) , where the histograms broadened for both dsDNA samples by measuring in a capillary (see table 13). This could be a consequence of using the same sample for the pressure test, in contrast to the FRET-benchmark where different sample concentrations have been used.

Table 14: important results of the FRET-measurement of dsDNA under pressure: FRET-efficiency E and width of the gaussian fit $width$

<i>sample</i>	<i>p(bar)</i>	<i>E</i>	<i>width</i>
dsDNA (Af488/Af594) (coverslip)	1	0.6864 ± 0.0066	0.1094 ± 0.0010
dsDNA (Af488/Af594)	1	0.6923 ± 0.0049	0.1096 ± 0.0076
dsDNA (Af488/Af594)	300	0.6932 ± 0.0055	0.1092 ± 0.0085
dsDNA (Af488/Af594)	600	0.6927 ± 0.0055	0.1075 ± 0.0085
dsDNA (Af488/Af594)	900	0.6927 ± 0.0058	0.1052 ± 0.0088
dsDNA (Af488/Atto647N) (coverslip)	1	0.7982 ± 0.0009	0.0939 ± 0.0014
dsDNA (Af488/Atto647N)	1	0.7948 ± 0.0026	0.1337 ± 0.0041
dsDNA (Af488/Atto647N)	1000	0.8009 ± 0.0026	0.1410 ± 0.0041
dsDNA (Af488/Atto647N)	2000	0.7873 ± 0.0037	0.1321 ± 0.0058

4.3.1 Discussion

The high-pressure-FRET setup is ready to use up to a pressure of 2000 bar, although it is elaborate, because the pressure stability is only guaranteed with a chance of 50%. Single molecule FRET measured, based on fluorescence intensity, is not influenced by pressure. For a lifetime-FRET measurement, it has to be considered that the fluorescence lifetime itself is pressure dependent.

4.4 Temperature evaluation

To also test the temperature setup, the temperature dependent relative fluorescence lifetime $\tau_{rel} = \tau(T)/\tau(26.5^\circ\text{C})$ of Rhodamin B (Sigma Aldrich, St. Louis, Missouri, USA) has been measured with increasing temperature. As a reference, the fluorescence lifetime was measured with a commercial TCSPC spectrometer (Fluorocube device, Horiba, Kyōto, Japan). For an increase of temperature of 20 Kelvin a decrease of the fluorescence lifetime of 55% has been found (blue, figure 4.18 a). Thereby the temperature could be directly measured with a thermometer in the sample volume, allowing for calibrating the lifetime-temperature relation.

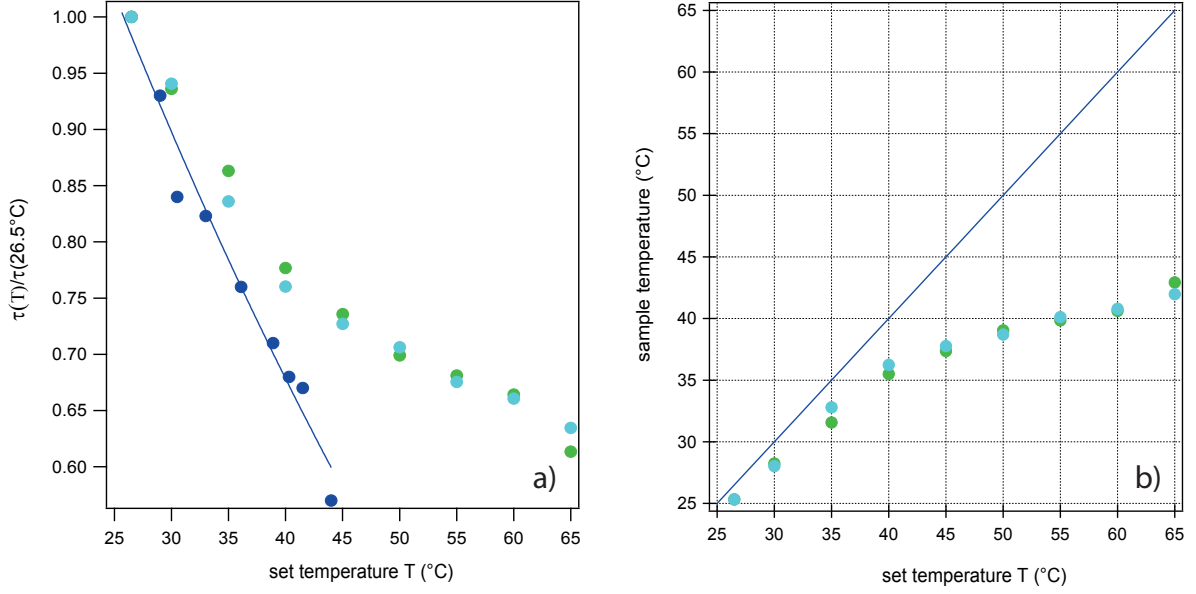


Figure 4.18: (a) Relative fluorescence lifetime of Rhodamine B in water measured with the reference fluorocube device (blue), on a coverslip with our temperature setup (cyan) and in the capillary with our temperature setup (green) vs. set temperature (b) real temperature vs. set temperature in the reference fluorocube device (blue), on a coverslip with our temperature setup (cyan) and in the capillary with our temperature setup (green)

The lifetime measured on the coverslip (cyan) and inside the capillary (green) (figure 3.11 a) , however, deviates from that in the cuvette for a set temperature. Consequently in our heating stage, the temperature in the sample is lower than at the position of the temperature sensor.

$$T_{sample}^{our\ setup} \neq T_{set}^{our\ setup} \quad (4.2)$$

With the calibration curve from the cuvette measurement, we can deduce the sample temperature, which is plotted in figure 4.18 b :

$$T_{sample} = f^{-1}[\tau(T_{set})/\tau(26.5^\circ\text{C})] \quad (4.3)$$

We see a lost of heat with our temperature setup. The difference between the set and the sample temperature increases above temperatures of 40°C , since the objective heating is limited to this temperature. The difference between the temperature on the coverslip and in the capillary are negligible.

4.4.1 Discussion

The temperature setup needs optimization. With the present setup the temperature gradient above the maximal temperature of the objective heating is significant. Nevertheless, it could be used for a temperature measurement up to 40°C, considering the temperature difference between the set and the sample temperature. A custom-built temperature-controlled sample holder employing Peltier elements used by Ben Schuler [77] could be more efficient and also enables a cooling of the sample. The temperature test itself by the temperature dependence of the fluorescence lifetime is straightforward and easily performed with the Fluorocube device.

4.5 Protein unfolding

The idea behind using FRET to investigate protein unfolding is that the average distance between two fluorophores, that have been attached to different positions of the protein, changes if the protein unfolds. The unfolding process can be investigated, because the energy transfer rate is highly distance dependent. Single molecule FRET, i.e. FRET measured with a single molecule concentration, allows to investigate the unfolded and the folded population separately. Thereby one peak in a FRET-histogram corresponds to the folded, whereas the other peak corresponds to the unfolded population. If the FRET-efficiency increases or decreases upon unfolding, depends on the labelling position. The area under the peaks of the histogram delivers the fractions of the populations and the position of the peak corresponds to the distance of the fluorophores, and consequently to the dimension of the protein.

The pressure unfolding experiments have been performed with the pressure setup, that was previously described. The denaturant unfolding experiments have been performed on a standard coverslip.

4.5.1 SlyD

SlyD is a two-domain protein. The FKBP-domain is the active centre for the catalysation of the isomerization (orange, figure 4.19), whereas the IF-domain (green, figure 4.19) is binding unspecifically with hydrophobic surfaces of unfolded proteins and shows a high chaperone activity [124, 125]. The protein shows an open and a closed conformation. It was chosen to investigate the influence of pressure on the conformational equilibrium of the two conformations.

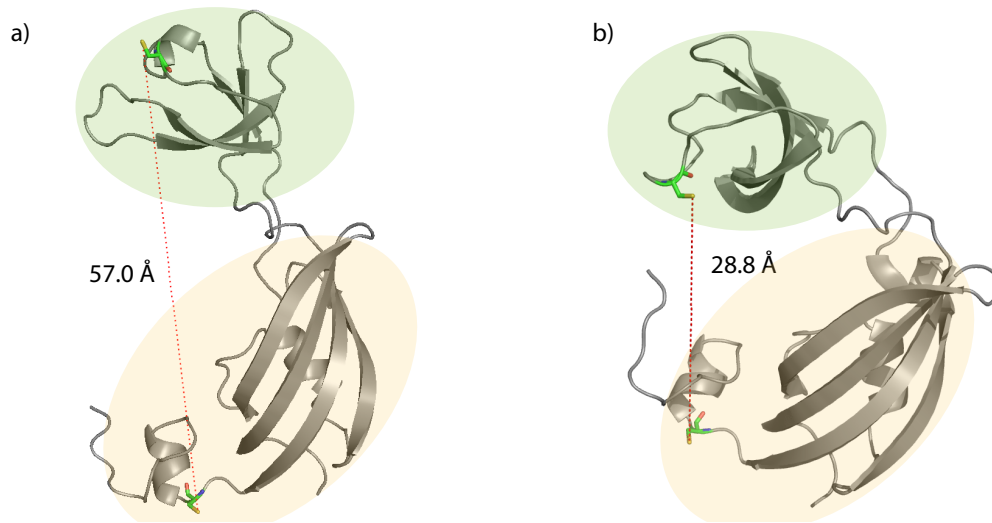


Figure 4.19: Secondary structure of the mutated protein TtSlyD: (a) open conformation (b) closed conformation. Two amino-acids are cysteine mutated (green) for an unspecific fluorescence labeling of Alexa 488 and Atto 647N. The distance between the cysteines has been calculated with the software Pymol (DeLano Scientific LLC, San Carlos, USA) from the crystal structure [128].

As a first unfolding experiment the protein SlyD has been investigated under pressure up to 2000 bar. To be sure that the protein will unfold, 2 M of Gdmcl was added to the solution. FRET-histograms at atmospheric pressure, 1000 and 2000 bar have been measured (figure 4.20 a). For comparison, also the FRET-histograms of a denaturant unfolding experiment, performed by Dana Kahra (University of Luebeck), are shown in figure 4.20 b, where the concentration of Gdmcl (Guanidiumhydrochloride) has been increased from 2 to 4 M Gdmcl.

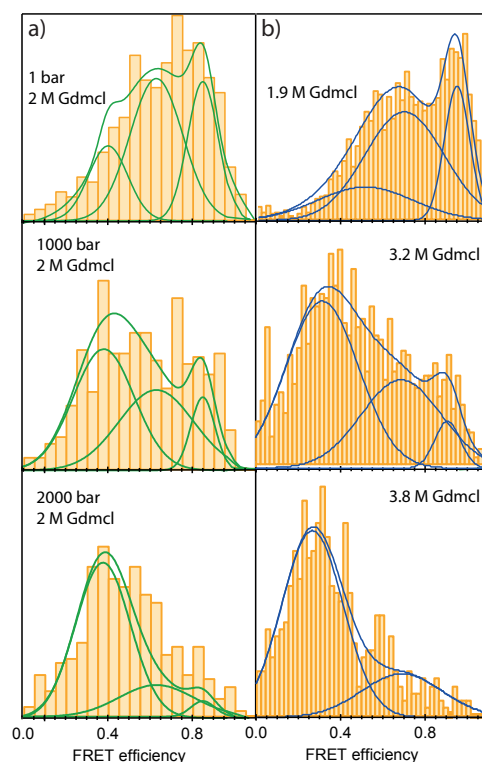


Figure 4.20: FRET-efficiency histograms 200 pM SlyD with increasing pressure and the addition of 1.3 M Gdmcl

For the experiment in the pressurized capillary, the quality of the FRET-histograms is not as good as on a coverslip, preventing a clear resolution of the three expected conformations (see figure 4.19). This is highlighting the importance of a good measurement quality, especially for a measurement with three different populations. The histogram of the denaturant experiment performed on a coverslip could be constructed with 50 instead of 30 FRET-bins (see section 3.5.3) because of the better measurement quality. Fitting the histograms with a three-peak Gaussian, the FRET-efficiencies had to be held constant for the pressure unfolding experiment, whereas for the denaturant unfolding experiment this was not necessary.

Still, a decrease of the two high-FRET peaks belonging to the native states and an increase of the low-FRET peak belonging to the unfolded state, can be observed in the FRET-histograms with increasing pressure or denaturant. Hence, an unfolding of the protein SlyD could be demonstrated, but because of the measurement quality, a quantitative evaluation of the measurement was not possible.

4.5.2 CspA

The Cold-shock protein A (CspA) is much more appropriate for a FRET-unfolding experiment. As a model folding protein, it is very well investigated and was selected because it is a simple two-state folder. Hence, only two populations are expected to be observed, an unfolded and a folded one. The protein has been labeled according to section 3.4.5.

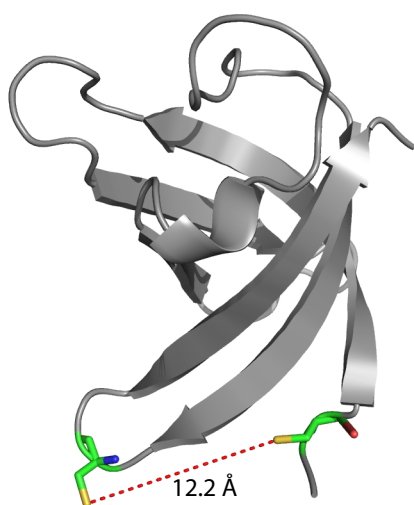


Figure 4.21: Secondary structure of the mutated protein CspA: Two amino-acids are cysteine mutated (green) for the fluorescence labeling of Alexa 488 and Alexa 647. The distance between the cysteines has been calculated with the software Pymol (DeLano Scientific LLC, San Carlos, USA) from the structure in solution [129].

FRET-histograms Results from smFRET unfolding experiments of CspA under the application of pressure (red) are compared with an unfolding with the denaturant guanidinium chloride (blue) (Sample 4, figure 4.22). With increasing pressure we see the same behavior as for an increasing denaturant concentration. The folded population with the higher FRET-efficiency of $E = 0.9$ decreases and the unfolded population with the lower FRET-efficiency at $E = 0.65$ increases. Unfortunately, 3000 bar was not sufficient for a complete unfolding. So in a third experiment 1.3 M Gdmcl was added to slightly destabilize the protein and the pressure has been increased up to 2000 bar for a complete combined denaturant/pressure unfolding (green). Still, increasing pressure leads to a shift of the populations towards the unfolded state as expected.

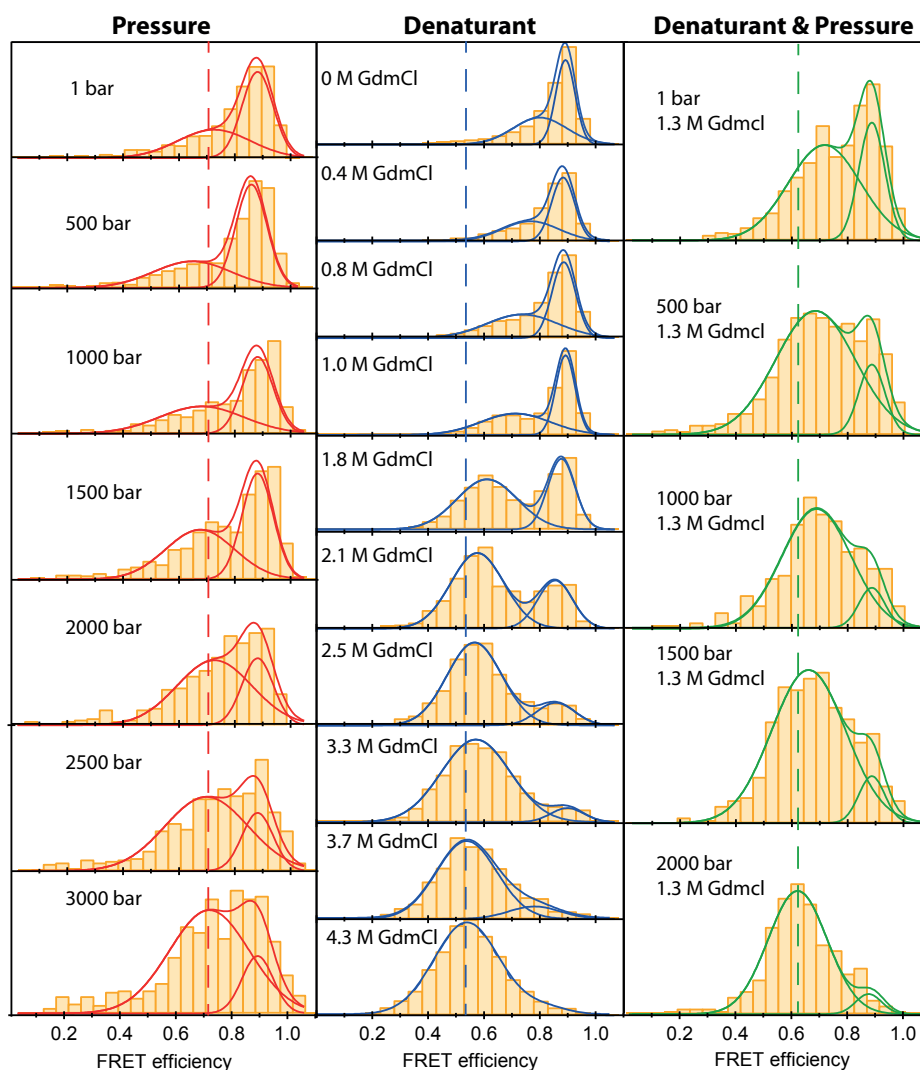


Figure 4.22: Sample 4: Comparison of the FRET-efficiency histograms of 100 pM cold-shock protein A, with increasing pressure, increasing denaturant concentration of guanidinium chloride (GdmCl) and increasing pressure with the addition of 1.3 M Gdmcl. The Fret efficiency of the unfolded state is highlighted with a dashed line.

The high number of unfolded proteins at 0 M Gdmcl should not occur since all proteins should be folded at atmospheric pressure and without denaturant. To avoid unrefolded proteins, that could cause the low fret peak at native conditions, the experiment has been repeated (Sample 4', figure 4.23), but now the sample has been diluted in a 6 M Gdmcl buffer to completely unfold the protein. Then it was diluted in a 0 M Gdmcl buffer to completely refold the protein before the actual unfolding experiment started. Whereas the folded peak completely vanishes in the following denaturant unfolding experiment on a coverslip, it can still be seen

in the pressure unfolding experiment in the capillary but it is much smaller. Additionally, the protein is less pressure stable and almost the complete unfolding process can be followed by increasing the pressure up to 2000 bar. The denaturant unfolding shows almost the same behavior for the two measurements. Since there are no unfolded proteins visible in the coverslip measurement anymore, the low FRET peak in the capillary should be an artifact of the capillary and will be subtracted for the quantitative evaluation.

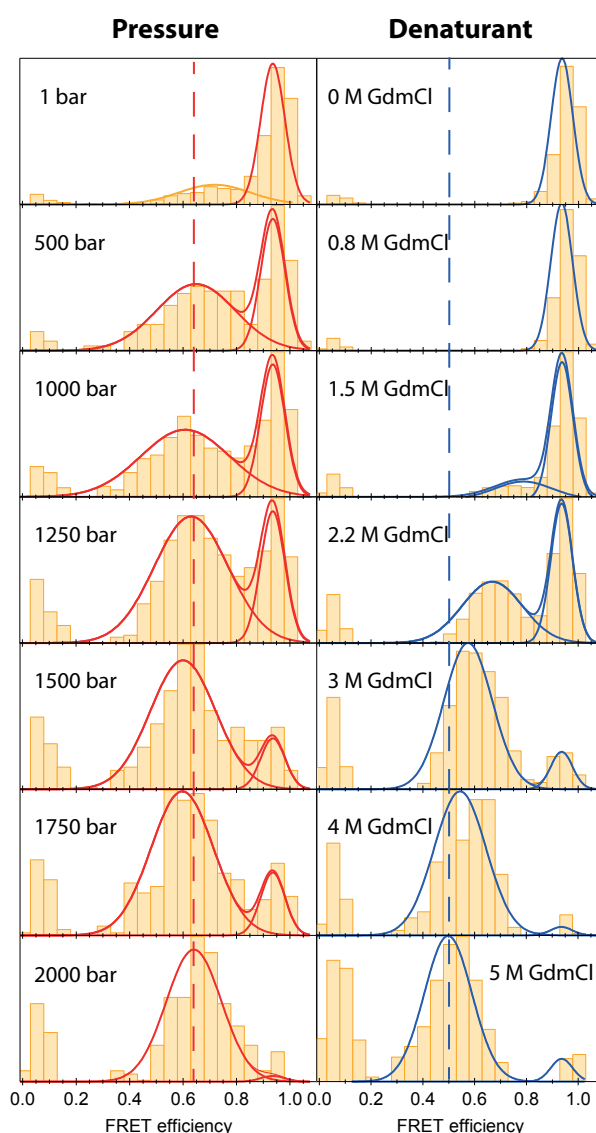


Figure 4.23: Sample 4': Comparison of the FRET-efficiency histograms of 100 pM cold-shock protein A, with increasing pressure and increasing denaturant concentration guanidinium chloride (GdmCl). The FRET efficiency of the unfolded state at the highest pressure or the highest denaturant concentration respectively, is indicated with a dashed line.

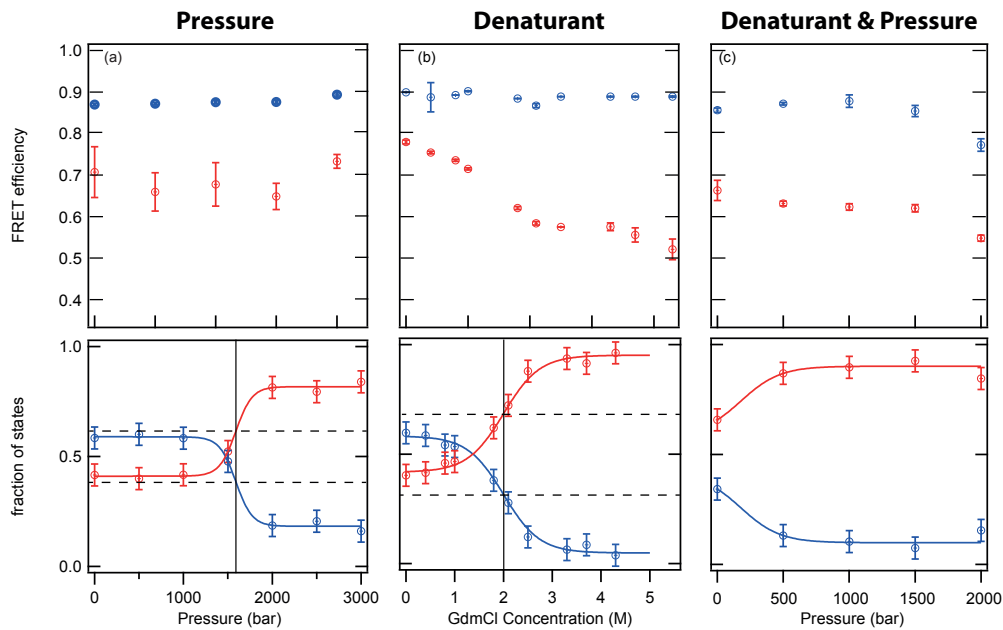


Figure 4.24: Sample 4: Comparison of the FRET-efficiency and the fraction of the unfolded (red) and the native state (blue) of 100 pM cold-shock protein A with (a) increasing pressure, (b) increasing denaturation concentration and (c) increasing pressure with the addition of 1.3 M Gdmcl

Equilibrium transitions The mean FRET-efficiency of the native and the unfolded population have been plotted versus the increasing pressure or increasing Gdmcl concentration (see figure 4.24 and figure 4.25). Comparing the FRET efficiencies obtained by applying pressure with those under increasing denaturant concentration, reveals a striking difference in the FRET peak corresponding to the denatured protein (red): While this peak is shifting to lower FRET efficiencies under increasing denaturant concentration (from $E = 0.78$ to $E = 0.52$ for sample 4 and from $E = 0.79$ to $E = 0.50$ for sample 4'), its position remains almost constant ($E = 0.68$ (sample 4) and $E = 0.61$ (sample 4')) when the pressure is increased. In contrast, the FRET-efficiency corresponding to the native protein (blue) is constant for all experiments ($E = 0.90$ (sample 4) and $E = 0.95$ (sample 4')) except for one outlier in the pressure unfolding with the addition of 1.3 M Gdmcl.

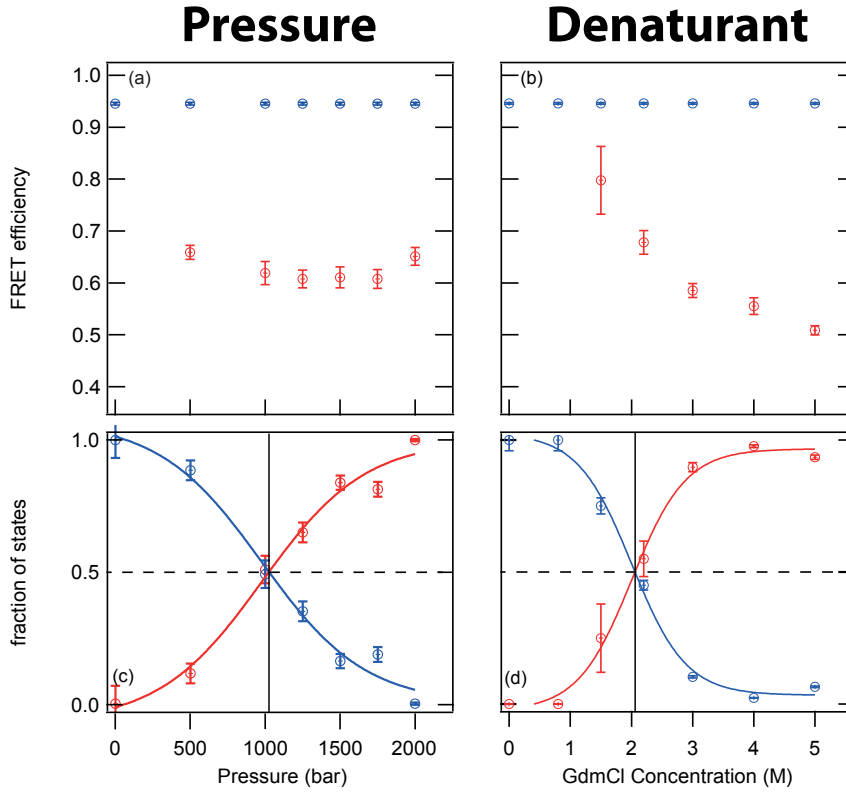


Figure 4.25: Sample 4': Comparison of the FRET-efficiency and the fraction of the unfolded (red) and the native state (blue) of 100 pM cold-shock protein A with (a) increasing pressure and (b) increasing denaturation concentration. The black lines represents the unfolding transition

The fractions of the native and the unfolded state giving the transition curves can be determined by calculating the area under the FRET-peaks of the different populations. Since unfolded proteins in sample 4' can be excluded the low fret peak at atmospheric pressure is an capillary artifact and is substracted. The transition curve fit functions have been calculated according to equation 2.65:

$$K_{DN} = \frac{c_D}{c_N} = \exp\left(-\frac{\Delta\mu}{RT}\right)$$

So for the unfolded $Fraction_D$:

$$Fraction_D(\Delta\mu) = \frac{c_D}{c_D + c_N} = \frac{1}{1 + \left(\frac{c_D}{c_N}\right)^{-1}} = \frac{1}{1 + \exp\left[\frac{(\Delta\mu)}{RT}\right]} \quad (4.4)$$

and for the native $Fraction_N$:

$$Fraction_N(\Delta\mu) = \frac{c_N}{c_N + c_D} = \frac{1}{1 + \frac{c_D}{c_N}} = \frac{1}{1 + \exp[-(\Delta\mu)/RT]} \quad (4.5)$$

As we consider only a two-state transition from a completely folded population to a completely unfolded we can simplify $\Delta\mu$ from equation 2.73 by stopping the Taylor series at the linear term. So for the pressure unfolding measurement $\Delta\mu$ can be simplified to $\Delta\mu(p) = \Delta\mu_0 + p\Delta V_0$:

$$Fraction_{D/N}(p) = \frac{1}{1 + \exp[\pm(\Delta\mu_0 + p\Delta V_0)/RT]} \quad (4.6)$$

and also for the denaturant unfolding experiment $\Delta\mu$ can be simplified to $\Delta\mu([D]) = \Delta\mu_0 - m \cdot [D]$:

$$Fraction_{D/N}([D]) = \frac{1}{1 + \exp[\pm(\Delta\mu_0 - m \cdot [D])/RT]} \quad (4.7)$$

The unfolded proteins in sample 4 have been considered with the introduction of the constants a and y_0 :

$$Fraction_{D/N}() = \frac{a}{1 + \exp[\pm(\Delta\mu)/RT]} + y_0 \quad (4.8)$$

Whereas the low FRET events of sample 4' at native conditions, which should be artifacts, have been subtracted.

The unfolding transition $[D]_H$ and p_H , where $\Delta\mu$ equals zero and 50% of the proteins have been unfolded, is at a denaturant concentration of:

$$[D]_H = \frac{\Delta\mu_0}{m} \quad (4.9)$$

or at a pressure of:

$$p_H = -\frac{\Delta\mu_0}{\Delta V} \quad (4.10)$$

Table 15: Thermodynamic parameters of CspA for the different samples: (1) Tryptophan fluorescence experiment of the wild-type performed by Erik Hinze (2) Tryptophan fluorescence experiment of the unlabeled but mutated CspA performed by Erik Hinze (3) Ensemble FRET and single molecule FRET denaturant unfolding experiments of the unspecifically labeled CspA performed by Erik Hinze (4) Single molecule FRET denaturant and pressure unfolding experiments of the specifically labeled CspA (4') Same as sample 4 but it has been completely unfolded and refolded before the unfolding experiment

sample (investigation-, unfolding-method)	$\Delta\mu_0$ (kcal/mol)	ΔV_0 (ml/mol)	m (kcal/(Mol · M))	$[D]_H$ (M)/ p_H (bar)
1: wt (tryptophan fl., Gdmcl)	3.10 ± 0.25		1.70 ± 0.08	1.82 ± 0.03
2: S2C/A59C (tryptophan fl., Gdmcl)	2.75 ± 0.22		1.63 ± 0.08	1.69 ± 0.04
3: S2C/A59C ^{488/647} (eFRET, Gdmcl)	2.56 ± 0.33		1.11 ± 0.21	2.31 ± 0.13
3: S2C/A59C ^{488/647} (smFRET, Gdmcl)	2.88 ± 0.72		1.16 ± 0.25	2.49 ± 0.24
4: S2C ⁶⁴⁷ /A59C ⁴⁸⁸ (smFRET, Gdmcl)	(3.3 ± 0.5)		(1.7 ± 0.2)	1.95 ± 0.53
4: S2C ⁶⁴⁷ /A59C ⁴⁸⁸ (smFRET, pressure)	(10.1 ± 9.3)	(-260 ± 260)		(1600 ± 3000)
4': S2C ⁶⁴⁷ /A59C ⁴⁸⁸ (smFRET, Gdmcl)	2.6 ± 0.5		1.4 ± 0.2	2.00 ± 0.67
4': S2C ⁶⁴⁷ /A59C ⁴⁸⁸ (smFRET, pressure)	1.7 ± 0.7	-71 ± 27		980 ± 780

The unfolding transition $[D]_H$, for the denaturant unfolding of the specific labeled sample 4 and sample 4' are in good agreement to a single molecule and an ensemble FRET-measurement of the unspecifically labeled sample 3, that has been done by Erik Hinze (Max-Planck-research-group: Enzymology of protein folding, Halle, Germany). Also performed tryptophan fluorescence experiments of the wild-type and a non labeled but mutated CspA needed less denaturant for a 50% unfolding (see table 15). The m-values for sample 3 and 4' are in good agreement within the error margins and higher then for the wildtype and the unlabeled CspA.

The unfolding transition of the pressure unfolding experiment is at $p_H = 980$ bar for sample 4'. The negative change in volume of sample 4' is about $\Delta V = 71$ ml. Unfortunately there is no literature of an pressure unfolding experiment of CspA.

The difference in chemical potential between the unfolded and the native state at room temperature $T = 293$ K, atmospheric pressure $p = 1$ bar and in the absence of denaturant is $\Delta\mu_0$, the conformational stability at atmospheric pressure without denaturant. For the denaturant unfolding and the pressure unfolding of sample 4' and sample 3 it is in agreement within the error range. Also the investigation of the wildtype and the unlabeled CspA show similar results but are a bit more stable. The thermodynamic parameters of sample 4 can not be compared because of the unrefolded proteins.

4.5.3 Frataxin

Another interesting two state folder is yeast frataxin because it is rather unstable at room temperature. Even at the temperature of maximal stability a fraction of unfolded proteins remains. Beside the consequence that it is not really pressure stable it is one of the very few available systems where cold and heat unfolding is measurable in a narrow and easily accessible temperature region (274 K – 324 K). The temperature unfolding experiment performed by the group of Ben Schuler [77] has been compared to a pressure unfolding measurement where the same sample has been used.

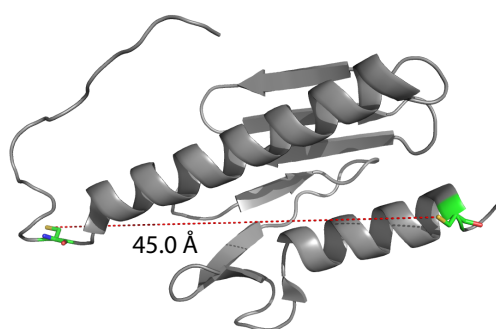


Figure 4.26: Secondary structure of the mutated protein Frataxin: Two amino-acids are cysteine mutated (green) for the unspecific fluorescence labeling of Alexa 488 and Alexa 594. The distance between the cyteins has been calculated with the software Pymol (DeLano Scientific LLC, San Carlos, USA) from the structure in solution [130].

FRET-histograms With a calculated fluorophore distance of $d = 45 \text{ \AA}$ the energy transfer rate is much smaller for the native protein than in the CspA experiment. As mentioned before, there is an unfolded population at room temperature and even at the temperature of maximal stability where the folded population is maximal. A small amount of pressure of 400 bar or a temperature increase of 31 K are enough that the folded population vanishes completely. Also cold denaturation can be seen as the folded population decreases by decreasing the temperature under the temperature of maximal stability $T_M = 289.7 \text{ K}$.

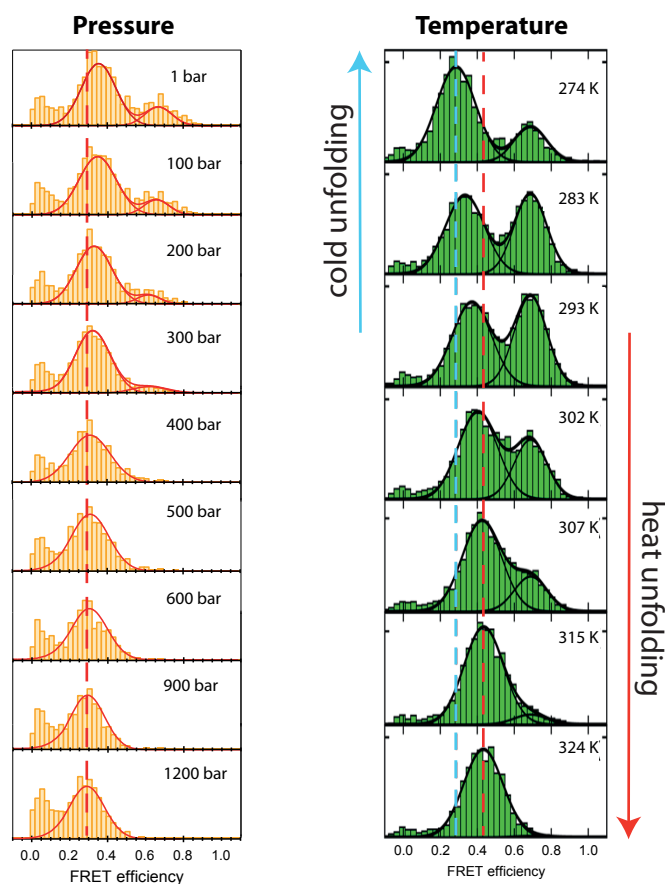


Figure 4.27: Comparison of the FRET-efficiency histograms of 100 pM Frataxin with increasing pressure and increasing temperature. The FRET efficiency of the unfolded state is highlighted with a dashed line. Temperature data taken from [77].

Unfortunately the FRET-histogram at room temperature on a coverslip is different to the histogram in our pressure experiment in a capillary (see figure 4.28) because the native population is smaller in the capillary measurement. This could be a consequence of capillary inner wall effects because the protein is conformationally very unstable.

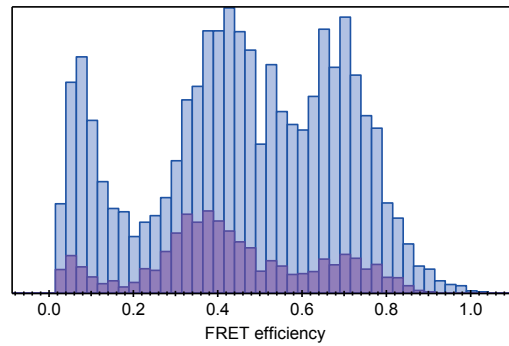


Figure 4.28: Comparison of the FRET-measurements of Frataxin at room temperature on a coverslip (blue) and in the capillary (purple): The native population is smaller in the capillary

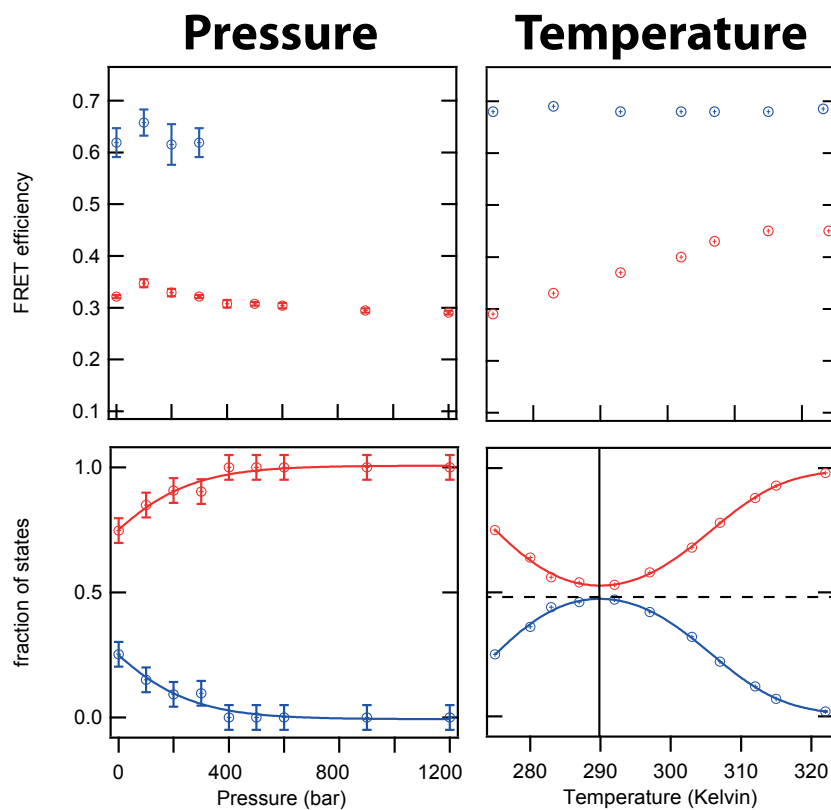


Figure 4.29: Comparison of the FRET-efficiency and the fraction of the unfolded (red) and the native state (blue) of 100 pM Frataxin with increasing pressure and temperature. The black line represent the point of maximal stability of the folded state. . Temperature data taken from [77].

Equilibrium transitions As expected, the structure of the native state stays stable both with increasing pressure and temperature with a FRET-efficiency around $E = 0.65$. The FRET-efficiency of the unfolded state is increasing with increasing temperature, whereas it is slightly decreasing with increasing pressure. Whereas cold and pressure unfolded states in our experiments expands with increasing pressure and decreasing temperature, heat unfolded states become more compact with increasing temperature.

The fractions of the populations are calculated in the same way as before in the CspA-experiment and are fitted for the pressure unfolding with the model function:

$$Fraction_{D/N}(p) = \frac{1}{1 + \exp[\pm(\Delta\mu/RT)]} \quad (4.11)$$

For Frataxin the difference of the chemical potential can not be simplified as before since there are unfolded proteins for every condition, and also cold denaturation has to be taken into account. For the chemical potential of temperature unfolding at constant pressure of $p = 1$ bar, equation 2.84 at a reference point of maximal stability T_M was used:

$$\Delta\mu(T, 1bar) = \Delta H_M - \frac{1}{2} \frac{\Delta C_P (T - T_M)^2}{T_M} \quad (4.12)$$

Hence the native and the denatured fraction is fitted by:

$$Fraction_{D/N}(T) = \frac{1}{1 + \exp[\pm[\Delta H_M - \frac{1}{2} \frac{\Delta C_P (T - T_M)^2}{T_M}]/RT]} \quad (4.13)$$

For the chemical potential of pressure unfolding at constant temperature of $T_R = 293$ K , equation 2.86 at a reference point of maximal stability p_M was used:

$$\Delta\mu(293 \text{ K}, p) = \Delta G_{M,293K} - \frac{1}{2} \cdot \Delta\beta_T (p - p_M)^2 \quad (4.14)$$

The native and the denatured fraction is fitted by:

$$Fraction_{D/N}(p) = \frac{1}{1 + \exp[\pm[\Delta G_M - \frac{1}{2} \cdot \Delta\beta_T (p - p_M)^2]/RT]} \quad (4.15)$$

The results are summarized in table 16.

Table 16: Thermodynamic parameters of Frataxin by pressure and temperature unfolding

unfolding method	$\Delta G_M, \Delta H_M (\frac{\text{kcal}}{\text{mol}})$	$\Delta C_P (\frac{\text{kcal}}{\text{mol} \cdot \text{K}})$	$\Delta\beta_T (\frac{\text{ml}}{\text{mol} \cdot \text{bar}})$	$p_M (\text{bar}), T_M (\text{K})$
pressure	-0.057 ± 0		0.298 ± 0.066	-467 ± 84
temperature	-0.0570 ± 0.0096	$1.411 \pm 0,038$		289.94 ± 0.15

The difference in chemical potential at the temperature of maximal stability $\Delta\mu(T_M) = \Delta H_M$, the isobaric heat capacity $\Delta C_p = T \frac{\partial \nabla S}{\partial T}$, the isothermal compressibility $\Delta\beta_T = -\frac{\partial \nabla V}{\partial p}$, the pressure p_M and the temperature T_m of maximal stability of the native state have been determined from a fit of the fraction curves in figure 4.29. At the point of maximal stability the chemical potential is maximal, e.g. the folded population reaches its maximum. At this point the difference in chemical potential between the folded and the unfolded state are almost the same for the pressure and the temperature experiment $\Delta\mu(T_M, 1 \text{ bar}) = \Delta H_M \approx \Delta\mu(293 \text{ K}, p_M) = \Delta G_M$. Therefore the maximal difference in chemical potential of the pressure experiment ΔG_M could be held constant at the value of ΔH_M , that has been determined from the fit of the temperature unfolding curve, during the fit of the pressure unfolding curve. This was necessary because only at the onset of the whole unfolding transition could be followed with the pressure unfolding experiment of frataxin. Otherwise the error of the thermodynamic parameters of the pressure experiment would have become too big. Unfortunately, there is no literature of a pressure unfolding experiment of yeast-frataxin.

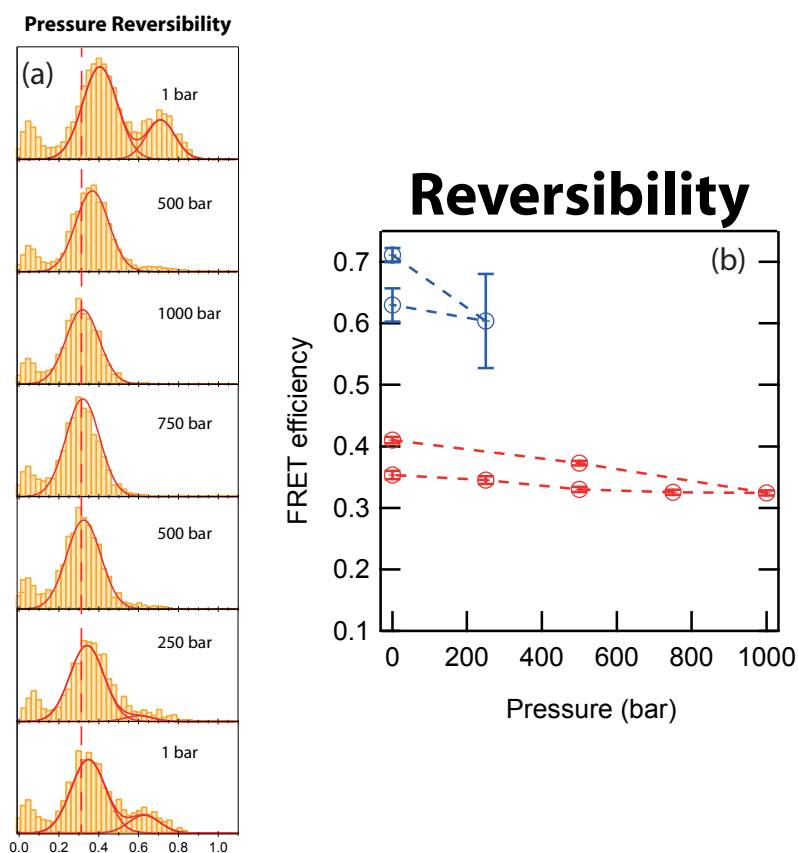


Figure 4.30: Pressure reversibility experiment: (a) FRET-efficiency histograms of Frataxin at increasing and decreasing pressure (b) FRET-efficiency of the native (blue) and the unfolded population (red)

Reversibility The reversibility of the unfolding by pressure can easily be tested by lowering the pressure after the increase. After increasing the pressure up to 1000 bar, which is sufficient to completely unfold frataxin, the pressure was decreased again. The folded population was recovered almost completely. The FRET-efficiency of the folded population decreased slightly, which is more a consequence of the worse fitting since the error is also significant at $p = 250$ bar. The FRET-efficiency of the unfolded population is also slightly decreasing with pressure, confirming the results of the preceding experiment. There is a weak hysteresis effect visible, which is probably a consequence of the weakening of the fluorophores rather than an expansion of the protein.

5 Conclusion

5.1 The quality of a fluorescence measurement in the high-pressure capillary

The curved surface of cylindrical capillaries, that have been used so far for fluorescence measurements under pressure, refracts the light, which leads to an enormous change of the focal volume and chromatic aberrations. Square bore capillaries are much more suited for single molecule fluorescence measurements. With the new arrangement introduced in this work, fluorescence measurements could be even further improved. FCS-benchmarks attested a measurement quality for single color experiments comparable to a measurement on a coverslip.

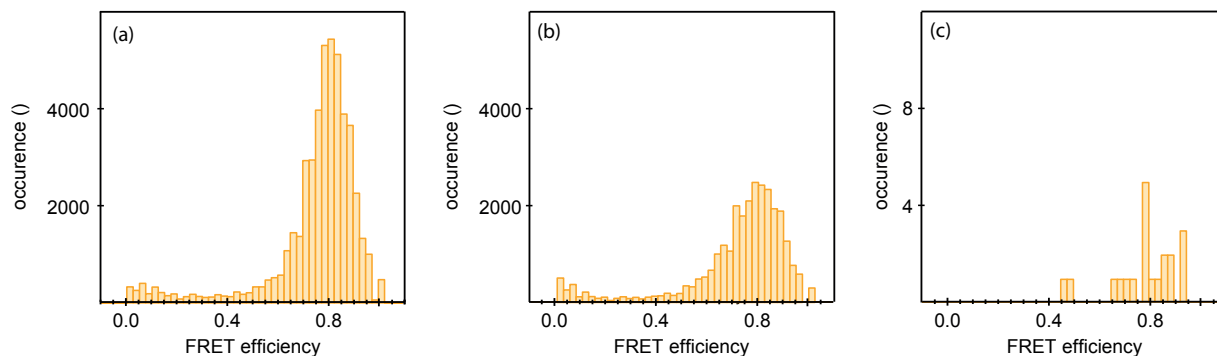


Figure 5.1: FRET measurement of a dsDNA solution labeled with Alexa Fluor 488 and Atto 647N (a) on a coverslip (b) with a square and (c) with a cylindrical capillary. The same sample has been used for all three measurements.

As can be seen in figure 5.1 FRET-measurements became possible, with the use of a square instead of a cylindrical capillary. Unfortunately the strong improvement for single color fluorescence measurements (see section 4.2.1) that comes with the new arrangement does not hold for multicolor measurements like FRET. An improvement with the new arrangement compared to a bare capillary can be seen, but it is not as powerful as expected from the FCS benchmark because of chromatical aberrations, resulting in a z-shift between the donor and the acceptor foci, that has been measured with a focal volume benchmark (see figure 4.9 and figure 4.8). One reason is the different material of fused silica, as could be stated from a fused silica coverslip measurement, that lies qualitatively between the new arrangement and the standard coverslip (see figure 5.2). Also, the imperfect shape of the inner and outer wall

of the capillary (see figure 3.3 and Appendix A.2) is contributing to this result. Other possible reasons are the glass quality of the capillary and the refractive index matching gel.

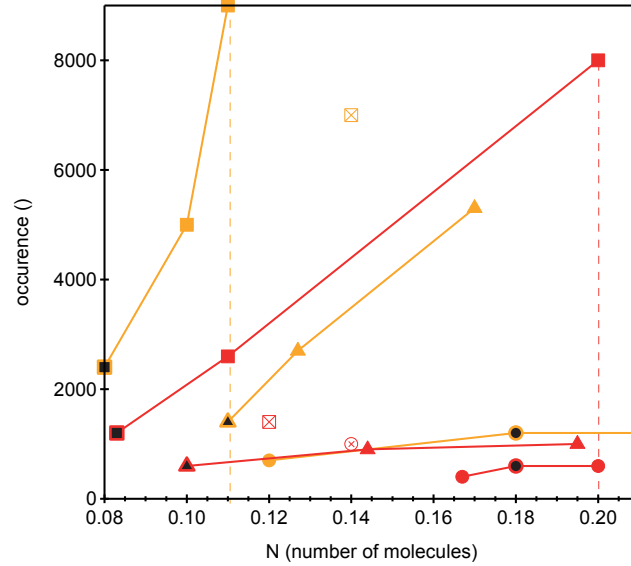


Figure 5.2: Maximal number of events of a FRET-histogram versus mean average number of molecules in the focal volume on a coverslip (rectangles), the bare capillary (circles), the new arrangement (triangles), a fused silica coverslip (cross-rectangles) and the new arrangement with a cylindrical capillary (cross-circle). The results of the dsDNA labeled with Alexa488/594 are shown in orange and the results of the Alexa488/Atto 647N labeled dsDNA in red. The FRET-benchmark with the same sample are filled black and the benchmark measurements with the same mean number of donor molecules are on the dashed lines.

To give an overview, in figure 5.2 the maximal number of events of a histogram versus the mean average number of molecules in the focal volume are plotted for different arrangements and for the two dye-couples. Here one can also see that the differences between the arrangements vary dramatically with the sample concentration and the used dye-pair. For all used concentrations and samples, the measurement quality could be improved with the new arrangement but is not as good as on a coverslip.

5.2 Protein unfolding by pressure

After reproducing the preparation methods and the handling of the capillary according to the work of Gratton et al. [56, 60], but using a square instead of a cylindrical capillary, 50% of

all pressure tests of the capillary up to 2000 bar have been successful. Then the amount of pressure in the capillary has been approved by measuring the pressure dependent fluorescence lifetime of Alexa 488 and compared to literature. As a negative control, the FRET-efficiency of a pressure stable fluorescently labeled dsDNA has been measured and no pressure artifacts have been found.

Three different proteins have been investigated under pressure: The multidomain protein SlyD, the two state folder CspA and the intrinsically unfolded yeast-Frataxin.

SlyD was chosen to investigate the influence of pressure on the conformational equilibrium of the two conformations: open and closed. An unfolding by pressure with the addition of 2 M GdmCl has been successful, but unfortunately the FRET measurement quality was not sufficient to separate and fit the different conformations in the FRET-histograms.

CspA has been investigated because it is a simple two state folder and as such a well investigated folding model protein. Only one folded population needs to be separated from an unfolded population in a fit of the FRET-histograms. 2 kbar has been sufficient to completely unfold the protein. Comparing the FRET efficiencies obtained by applying pressure with those under increasing denaturant concentration reveals a striking difference in the behaviour of the denatured protein: whereas the unfolded chain is expanding by increasing the denaturant concentration, its size remains almost constant when the pressure is increased. This expansion of the denatured state by increasing denaturant concentration is a consistent finding in all of the free diffusing experiments, first unequivocally demonstrated for CspTm [133], has been observed in chymotrypsin inhibitor 2 [134, 29], acyl-CoA binding protein [29], RNase H [135, 136], protein L [137, 138], the B domain of protein A [139], the immunity protein Im9 [140], and the prion-determining domain of Sup35 [141]. No literature has been found about the behaviour of the unfolded protein CspA with increasing pressure. The difference in chemical potential between the native and the unfolded state at atmospheric pressure and without denaturant coincide within the error range for the denaturant and the pressure experiment and is about $\Delta\mu_0 = 2 \text{ kcal/mol}$. The difference in volume between the native and the unfolded state, determined by pressure unfolding, is about $\Delta V = -70 \text{ ml}$, and the unfolding transition is at $[GdmCl]_H = 2 \text{ M}$ and $p_H = 1 \text{ kbar}$.

Frataxin was chosen because of its conformational instability, which makes it perfect to study the unfolded state. The protein is never completely folded, hence an unfolded population always remains. Comparing the FRET efficiencies of a pressure unfolding experiment with a cold and heat denaturation experiment performed by the group of Ben Schuler, a different behaviour of the unfolded state can be seen. Whereas the extension (size) of the unfolded

chain is decreasing constantly with temperature, it is only slightly increasing with pressure. So whereas cold and pressure unfolded states in our experiments expands with increasing pressure and decreasing temperature, heat unfolded states become more compact with increasing temperature. Explicit investigations of the size of the pressure unfolded state do not exist yet, an investigation of the heat, cold and pressure unfolding of ribonuclease A by NMR spectroscopy by Jonas et al. [143]. On the basis of the hydrogen-deuterium exchange rates it was concluded that the cold and pressure denatured RNase A molecules contain some partial secondary structure, in contrast to the thermally denatured one. Analyzing the secondary structure sensitive amide I region of the FTIR spectrum of myoglobin, a similar conclusion has been found [144]. Griko and Kutysenko also found that the cold and heat denatured phases of L-lactoglobulin are different [145]. By a NMR measurements they concluded that the network of residual interactions is more extensive in the cold denatured state than in the heat unfolded one.

Because only a small portion of the whole unfolding behaviour could be followed with the pressure unfolding experiment of frataxin, the value of the maximal difference of the chemical potential $\Delta H_M = -0.06 \frac{\text{kcal}}{\text{mol}\cdot\text{K}}$ of the temperature unfolding experiment was used and held constant for the fit of the pressure unfolding curve. Otherwise the error of the thermodynamic parameter of the pressure experiment would have become to big. The compressibility is $\Delta\beta_T = 0.3 \frac{\text{ml}}{\text{mol}\cdot\text{bar}}$ and the pressure of maximal stability is $p_M = -470 \text{ bar}$. No literature has been found about the behaviour of the unfolded protein Frataxin with increasing pressure. For a next pressure unfolding experiment Frataxin should be stabilized with the addition of 50–100 mM sodium phosphate to cover the complete unfolding transition with the experiment.

6 Outlook

Either the reduction of the pressure range by the use of a coverslip-based arrangement as in the work of Vass et al. [131], where the pressure is limited to 1200 bar or a custom made square capillary which is very expensive (10.000 \$) will improve the optical conditions. An other approach was made by Haver et. al. [132], where they improved the image contrast of a cylindrical capillary by spatial deconvolution. Although this was an approach to improve the imaging, spatial deconvolution could be also used for single molecule fluorescence. To find a compromise between price, optical quality, and pressure stability, an arrangement where the optics of a cylindrical capillary were improved by the same arrangement, that we used in our work for the square capillary, has been used and surprisingly showed as good FRET-histograms as with the square capillary (crossed circle in figure 5.2). So for two color experiments, the cylindrical capillary immersed in a refractive index matching liquid on a fused silica coverslip

could be a good compromise between optics and pressure stability because the cylindrical capillary can hold much higher pressure up to 4 kbar.

A better pressure stability would also facilitate the unfolding experiments, making it possible to measure at much more pressure steps. More measurement points results in better, more trustworthy, values with a smaller error range. Also the measurement time can be expanded with more stable capillaries, leading to histograms with more FRET-events, allowing a better separation of different populations.

The temperature setup can be used for temperature experiments below $T = 40^{\circ}\text{C}$. A combined pressure and temperature experiments is the next step, enabling to determine a p-T-phase diagram of a protein. Also the investigation of the effect of a combined change of pressure and temperature is of great interest onto the size of the unfolded chain. (For example, what is the behaviour of the pressure unfolded state by increasing temperature or vice versa) The main reason for the limited temperature range is the loss of heat via the objective because the objective must not be exposed to temperatures above $T = 40^{\circ}\text{C}$. With a more durable and better isolated objective the temperature regime can be expanded. A custom-built temperature-controlled sample holder employing Peltier elements used by Ben Schuler [77] could also enable a cooling of the sample.

There are also many other biochemical applications beyond protein unfolding for a single molecule detection under pressure because of the low concentration needed and the differentiation ability of the method. Fluorescence correlation spectroscopy (FCS) for example is very sensitive and demands only low concentration. This reduces aggregation and allows to investigate the effect of pressure on binding equilibria with nanomolar and subnanomolar dissociation coefficients. Also to visualize local and morphological changes of the membrane of lipid vesicles due to high pressure, single molecule fluorescence under pressure can be used [142], to gain a better understanding of biological membranes.

A Appendix

A.1 Capillary handling

The capillary should be handled with special care. Any bending or other mechanical shock leads to a capillary that will not hold the pressure and is making the capillary useless for a pressure experiment.

1. Cut a 20 cm long piece of the capillary with scissors.

2. Clean the capillary with acetone

3. Preparation of the glue:

-Latex or Nitrile gloves are required in order to reduce any dermal exposure

-Check if the epoxy resin (part A) is not crystallized. Subjecting the resin to a temperature of 40-50°C for a 4 hours is sufficient to remelt the crystals.

-Add 100 parts (weight: 2.85 g) of Epotek 301-2 part A and mix it with 35 parts of Epotek 301-2 part B (weight: 1.00 g). Be sure to mix it slowly with a stirring staff to avoid air entrapment.

-Centrifuge the mixture

4. Put the pressure plug in the capillary holder, the capillary in the pressure plug and then the capillary holder in the oven

5. Fill in the prepared glue with a syringe into the pressure plug. Use a cut pipette tip on top of the syringe to have a clean and sensitive syringe.

6. Bake the capillary for 3.5 hours at 80°C

7. Remove a 2 cm long area of the protection layer by the flame of a blowtorch (only propane) to form an observation window. Be sure that the window will be at the right position before you start and clean the observation window with acetone.

8. Remove a 1 cm long area of the protection layer by the flame of a blowtorch (only propane) at the tip of the capillary and clean it with a dry tissue

9. Fill in the sample solution of interest by capillary force, dipping the end of the capillary into the solution

10. Check the filling by a microscope. There must be two sample liquid surfaces bended in the direction of the sample liquid and the capillary should be at least 50% filled. If the filling failed, try to remove the sample with compressed-air and start again.

11. Close the capillary, by touching the very end of the capillary by the flame of a blowtorch (propane and oxygen)

A.2 Pictures of the square fused silica capillary taken with a Koyence VHX5000 digital microscope

12. Dip the other end of the capillary in silicon oil to separate the sample from the pressurizing liquid
13. Connect the pressure plug to the pressure gland and use it to connect the capillary to the screw piston pump
14. Do not use much power to tighten the gland. Fasten the screw with two fingers and a screw wrench only!
15. Good luck!

A.2 Pictures of the square fused silica capillary taken with a Koyence VHX5000 digital microscope

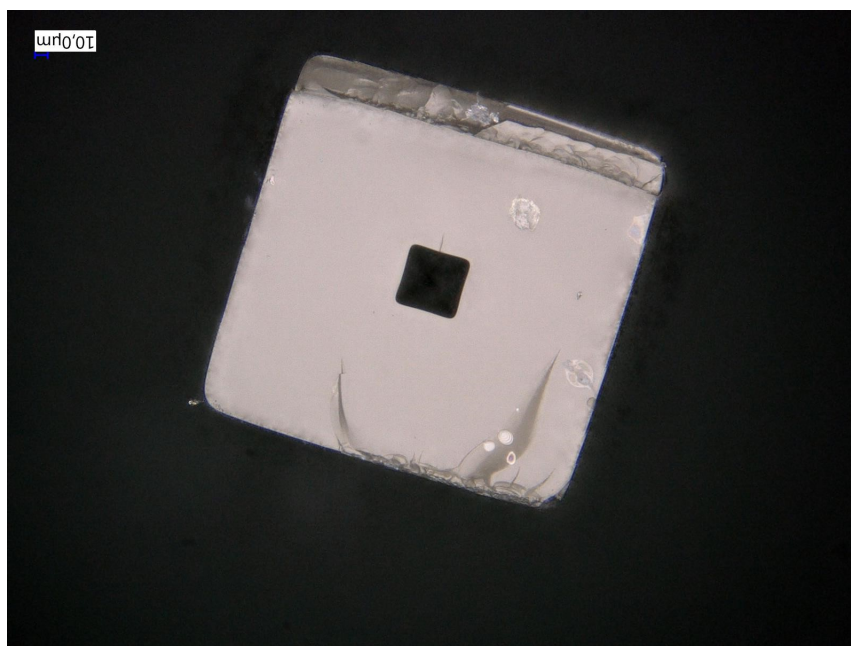


Figure A.1: Cross section of the capillary

A.2 Pictures of the square fused silica capillary taken with a Koyence VHX5000 digital microscope

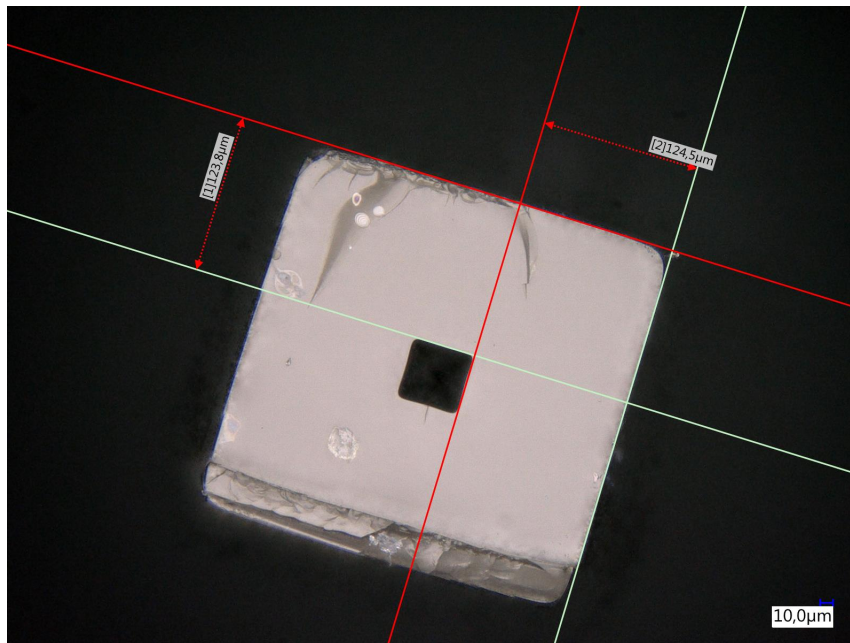


Figure A.2: Cross section with measured wall thickness

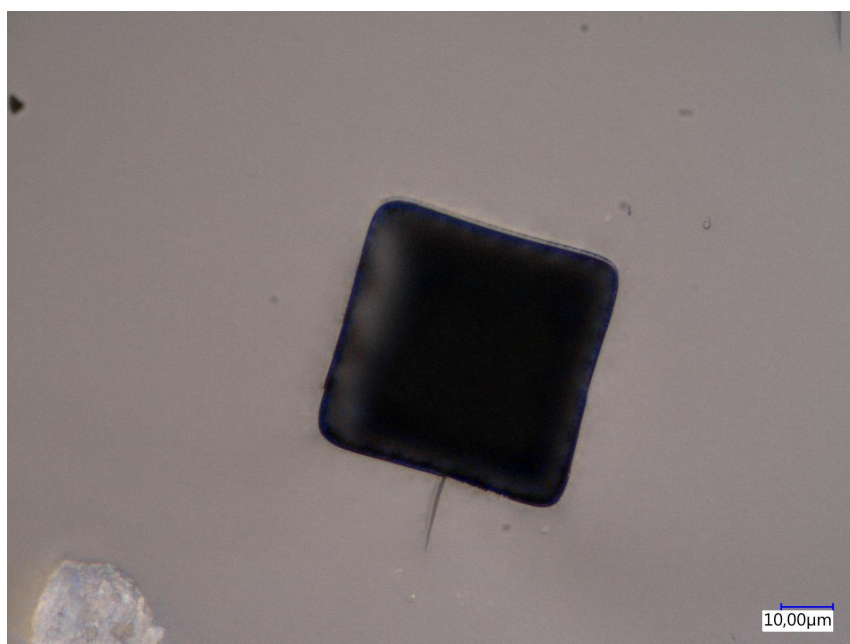


Figure A.3: Cross section of the cavity of the capillary

A.2 Pictures of the square fused silica capillary taken with a Koyence VHX5000 digital microscope

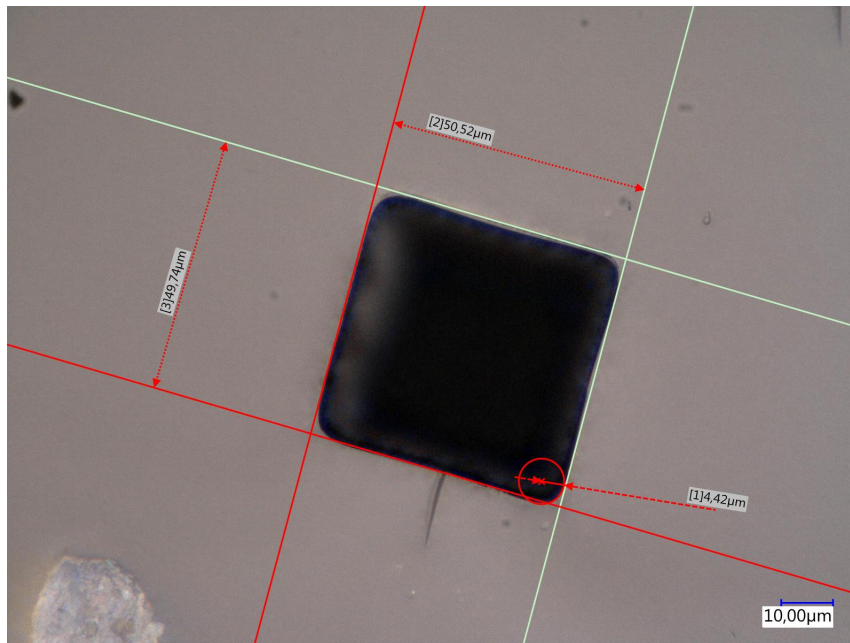


Figure A.4: Measured dimensions of the cavity of the capillary

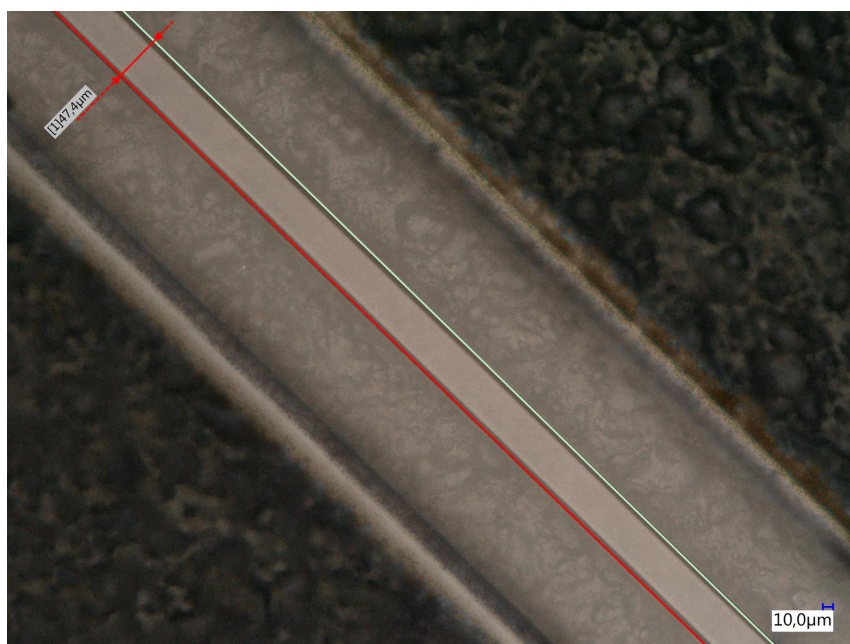


Figure A.5: Capillary from above

A.3 Calculation of the optimal relation between the fused silica and the borosilica thickness for a compensation of the refractive index difference

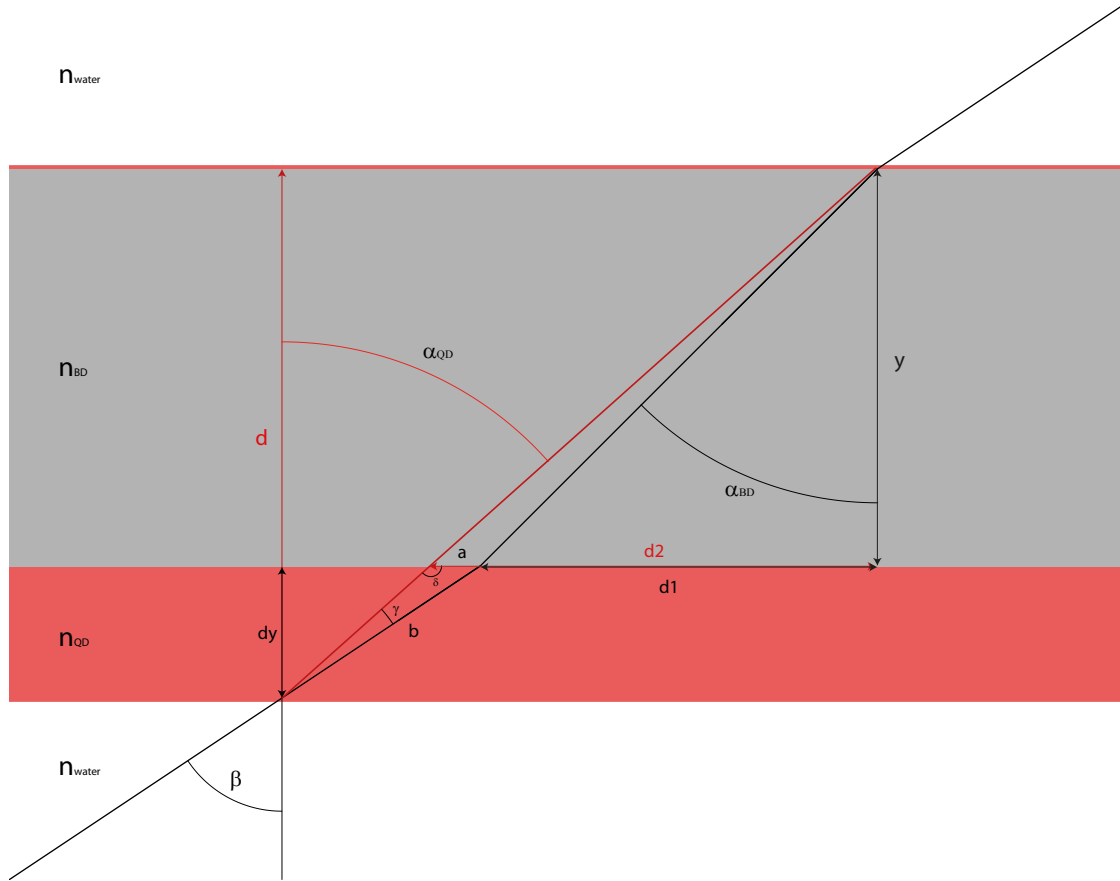


Figure A.6: Optical path in fused silica (red) and borosilicate (black): with the optimal relation between fused silica thickness d and borosilicate thickness y the difference in refractive index can be compensated.

$$d_1 = y \cdot \tan(\alpha_{\text{BD}}) \quad (\text{A.1})$$

$$d_2 = y \cdot \tan(\alpha_{\text{QD}}) \quad (\text{A.2})$$

$$a = d_2 - d_1 = y \cdot [\tan(\alpha_{\text{QD}}) - \tan(\alpha_{\text{BD}})] \quad (\text{A.3})$$

Law of sines:

$$\frac{a}{b} = \frac{\sin(\gamma)}{\sin(\delta)} \quad (\text{A.4})$$

A.4 Influence of the correction collar at the xy-cross section of the focal volume

$$b = a \frac{\sin(\delta)}{\sin(\gamma)} = y \cdot [\tan(\alpha_{QD}) - \tan(\alpha_{BD})] \frac{\sin(\alpha_{QD} + 90)}{\sin(\beta - \alpha_{QD})} \quad (\text{A.5})$$

$$d = y + dy = y + b \cdot \cos \beta = y + y \cdot \cos \beta [\tan(\alpha_{QD}) - \tan(\alpha_{BD})] \frac{\cos(\alpha_{QD})}{\sin(\beta - \alpha_{QD})} \quad (\text{A.6})$$

Snell's law:

$$\frac{n_1}{n_2} = \frac{\sin(\alpha_2)}{\sin(\alpha_1)} \quad (\text{A.7})$$

$$\alpha_{BD} = \arcsin\left(\frac{n_{\text{water}}}{n_{BD}} \sin \beta\right) = \arcsin\left(\frac{1.33}{1.53} \sin \beta\right) \quad (\text{A.8})$$

$$\alpha_{QD} = \arcsin\left(\frac{n_{\text{water}}}{n_{QD}} \sin \beta\right) = \arcsin\left(\frac{1.33}{1.46} \sin \beta\right) \quad (\text{A.9})$$

$$\frac{d}{y} = 1 + \cos \beta [\tan(\arcsin(\frac{1.33}{1.46} \sin \beta)) - \tan(\arcsin(\frac{1.33}{1.53} \sin \beta))] \frac{\cos(\arcsin(\frac{1.33}{1.46} \sin \beta))}{\sin(\beta - \arcsin(\frac{1.33}{1.46} \sin \beta))} \quad (\text{A.10})$$

A.4 Influence of the correction collar at the xy-cross section of the focal volume

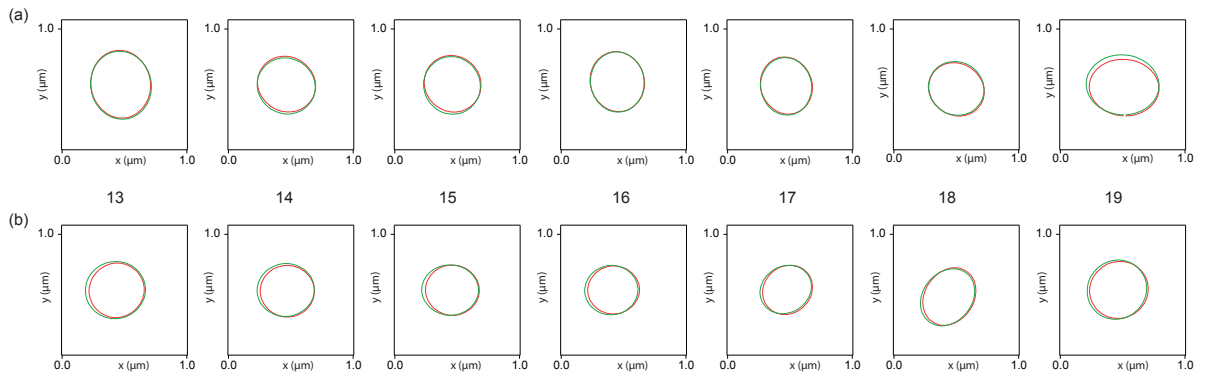


Figure A.7: Influence of the correction collar (13-19) at the xy-cross section in the center of the focal volume of the acceptor (red) and the donor (green) focus for (a) the Alexa Fluor 488/Alexa Fluor 594-setup and (b) the Alexa Fluor 488/Atto647N-setup. The radius of a focal volume is defined as the distance from the center of the focal volume to the position where the intensity decreased to $1/e^2$ of the maximal Intensity in the center of the focal volume. The sample was excited with the donor excitation wavelength of 488 nm.

A.5 FRET-efficiency histograms of the unspecifically labeled cold-shock protein A

Also the unspecifically labeled CspA (sample 3) has been investigated with FRET. Here the unfolded peak at atmospheric pressure vanishes also for the pressure measurement in the capillary. Unfortunately the unspecific labeling lead to a pressure stabilization of the protein and 2000 bar was not enough pressure to unfold the protein. Also the addition of 1.3 M Gdmcl did not lead to a complete pressure unfolding. The denaturant unfolding on the other hand was similar to the precedent measurements.

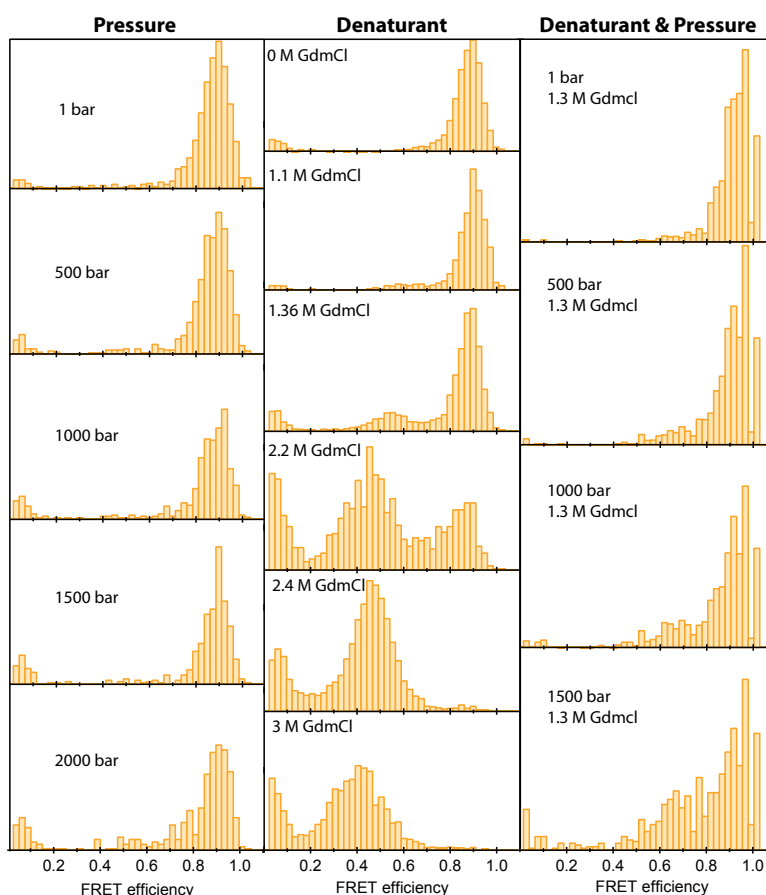


Figure A.8: Sample 3: Comparison of the FRET-efficiency histograms of 100 pM cold-shock protein A of the second unspecifically labeled stock, with increasing pressure, increasing denaturant concentration guanidiniumchloride (GdmCl) and increasing pressure with the addition of 1.3 M Gdmcl .

A.6 Fluorescence intensity measurement under pressure

As we measure FRET by the fluorescence intensity according to eq. 2.22, the pressure dependency of the fluorescence intensity of the fluorophores has to be investigated. According to our measurement (figure A.9) the fluorescence intensity of Alexa 488 and Atto 647N is not pressure dependent.

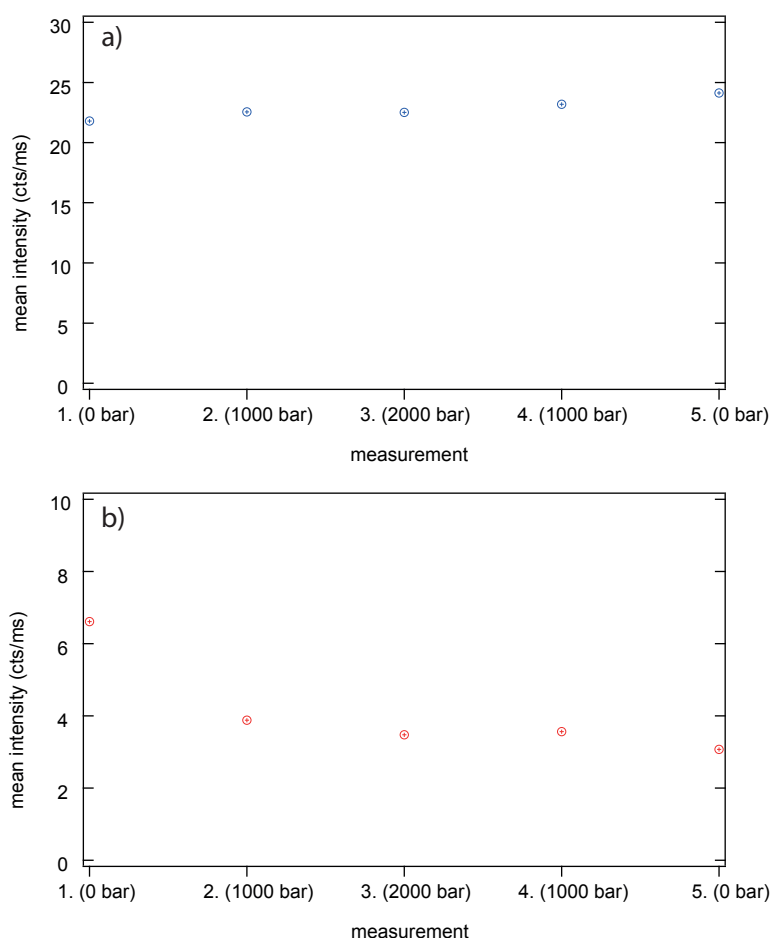


Figure A.9: Mean fluorescence intensity of (a) Alexa 488 and (b) Atto 647N under pressure

References

- [1] Fourme R., Girard E., Kahn R., Dhaussy A.-C. & Ascone I. Advances in High-Pressure Biophysics: Status and Prospects of Macromolecular Crystallography. *Annu. Rev. Biophys.*, Vol.38, 153–171, 2009

- [2] Gross M., Jaenicke R., The influence of high hydrostatic pressure on structure, function and assembly of proteins and protein complexes. *Eur. J. Biochem.* Vol. 221, 617–30, 1994
- [3] Howland J., *Extremophiles-Microbial Life in Extreme Environments*, Biochemical Education, Vol. 26, 331, 1998
- [4] Jannasch HW, Taylor CD., Deep sea microbiology. *Annu. Rev. Microbiol.* Vol. 38, 487–514, 1984
- [5] Balny, C., Hayashi, R., Heremans, K., Masson, P., eds. “High Pressure and Biotechnology”, Vol. 224, 1992
- [6] Hayashi R., Application of high pressure to food processing and preservation: philosophy and development, *Engineering and Food*, Vol. 2, 815–26, 1989
- [7] Mozhaev V.V., Heremans K., Franks J., Masson P., Balny C., Exploiting the effect of high hydrostatic pressure in biotechnological applications. *Trends Biotechnol.*, Vol.12, 493–501, 1994
- [8] Roger Fourme, Eric Girard, Richard Kahn, Anne-Claire, and Isabella Ascone, *Advances in High-Pressure Biophysics: Status and Prospects of Macromolecular Crystallography*, *Annual Review of Biophysics*, Vol. 38, 153-171, 2009
- [9] Silva, J.L., Weber G., Pressure stability of proteins. *Annu. Rev. Phys. Chem.*, Vol. 44, 89-113, 1993
- [10] Collins M. D., Kim C. U. and Gruner S. M., High-pressure protein crystallography and NMR to explore protein conformations, *Ann. Rev. Biophys.*, Vol. 40, 81–98, 2011
- [11] Bridgman P.W., The coagulation of albumen by pressure, *J. Biol. Chem.*, Vol. 19, 511–512, 1914
- [12] Thomanek U.F., Parak F., Mossbauer R.L., Formanek H., Schwager P., Hoppe W., Freezing of myoglobin crystals at high pressure, *Acta Crystallogr.*, Vol.29, 263–65, 1973
- [13] www.sigmaaldrich.com
- [14] Kundrot C.E., Richards F.M., Collection and processing of X-ray diffraction data from protein crystals at high pressure, *J. Appl. Crystallogr*, Vol. 19, 208–13, 1986

REFERENCES

- [15] Kundrot C.E., Richards F.M. . Crystal structure of hen egg-white lysozyme at a hydrostatic pressure of 1000 atmospheres. *J. Mol. Biol.*, Vol. 193, 157–70, 1987
- [16] Williamson M.P., Akasaka K., Refaee M., The solution structure of bovine pancreatic trypsin inhibitor at high pressure, *Protein Sci.*, Vol. 12, 1971–79, 2003.
- [17] Kalbitzer H.R., Gorler A., Li H., Dubovskii P.V., Hengstenberg W., NMR study of histidine containing protein (HPr) from *Staphylococcus carnosus* at high pressure. *Protein Sci.*, Vol. 9, 693–703, 2000
- [18] Kitahara R., Yamada H., Akasaka K., Two folded conformers of ubiquitin revealed by high-pressure NMR, *Biochemistry*, Vol. 40, 13556–63, 2001
- [19] Inoue K., Maurer T., Yamada H., Herrmann C., Horn G., High-pressure NMR study of the complex of a GTPase Rap1A with its effector RalGDS. A conformational switch in RalGDS revealed from non-linear pressure shifts, *FEBS Lett.* , Vol. 506, 180–84, 2001
- [20] Inoue K., Yamada H., Imoto T., Akasaka K., High pressure NMR study of a small protein, gurmarin, *J. Biomol. NMR.*, Vol. 12, 535–41, 1998
- [21] Kuwata K, Li H, Yamada H, Batt CA, Goto Y, Akasaka K., High pressure NMR reveals a variety of fluctuating conformers in beta-lactoglobulin, *J. Mol. Biol.*, Vol.305, 1073–83, 2001
- [22] Möglich A., Koch B., Gronwald W., Hengstenberg W., Brunner E., Kalbitzer H.R., Solution structure of the active-centre mutant I14A of the histidine-containing phosphocarrier protein from *Staphylococcus carnosus*, *Eur. J. Biochem.*, Vol. 271, 4815–24, 2004
- [23] Refaee M., Tezuka T., Akasaka K., Williamson M.P., Pressure-dependent changes in the solution structure of hen egg-white lysozyme. *J. Mol. Biol.* Vol.327, 857–65, 2003
- [24] Lu H.P.,Xun L. , Sunney Xie X., Single-molecule enzymatic dynamics,Vol. 282,1877-1882, 1998
- [25] Nie S., Zare R.N., Optical detection of single molecules, *Annual Review of Biophysics and Biomolecular Structure*, Vol. 26, 567-596, 1997
- [26] Xie X.S., Trautman J.K., Optical studies of single molecules at room temperature, *Annual Review of Physical Chemistry*, Vol. 49, 441-480, 1998

-
- [27] Hirschfeld T., Optical microscopic observation of single small molecules, *Appl. Opt.*, Vol. 15, 2965-2966, 1976.
- [28] Shera E. B., Seitzinger N. K., Davis L. M. , Keller R. A., Soper S. A., Detection of single fluorescent molecules, *Chemical Physics Letters*, Vol. 174, 553-557, 1990
- [29] Schuler B., Lipman E.A., Eaton W.A., Probing the free-energy surface for protein folding with single-molecule fluorescence spectroscopy, Vol. 419, 743-747, 2002
- [30] Schuler B., Single-molecule fluorescence spectroscopy of protein folding, *ChemPhysChem*, Vol. 6, 1206–1220, 2005
- [31] Stryer L., Haugland R. P. ,Energy transfer: a spectroscopic ruler., *Proc. Natl. Acad. Sci.*, Vol. 58, 719 – 726, 1967
- [32] Trautman J. K., Macklin J. J., Brus L. E., Betzig E., Near-field spectroscopy of single molecules at room temperature, *Nature*, Vol. 369, 40–42, 1994
- [33] Ambrose W. P., Goodwin P. M., Martin J. C., Keller R. A., Single molecule detection and photochemistry on a surface using near-field optical excitation., *Phys. Rev. Lett.*, Vol. 72, 160–163, 1994
- [34] Xie X. S., Dunn R. C., Probing single molecule dynamics, *Science*, Vol. 265, 361–364, 1994
- [35] Macklin J. J., Trautman J. K., Harris T. D., Brus L. E., Imaging and time-resolved spectroscopy of single molecules at an interface, *Science*, Vol. 272, 255–258, 1996
- [36] Trautman J. K., Macklin J. J., Time-resolved spectroscopy of single molecules using near-field and far-field optics, *Chem. Phys.*, Vol. 205, 221–229, 1996
- [37] Funatsu T., Harada Y., Tokunaga M., Saito K., Yanagida T., Imaging of single fluorescent molecules and individual ATP turnovers by single myosin molecules in aqueous solution, *Nature*, Vol. 374, 555–559, 1995
- [38]] Sase I., Miyata H., Corrie J. E. T., Craik J. S., Kinoshita Jr. K., Real time imaging of single fluorophores on moving actin with an epifluorescence microscope, *Biophys. J.*, Vol. 69, 212–218, 1995

REFERENCES

- [39] Schmidt T., Schuetz G. J., Baumgartner W., Gruber H. J., Schindler H., Characterization of photophysics and mobility of single molecules in a fluid lipid membrane, *J. Phys. Chem.*, Vol. 99, 17662–17668, 1995
- [40] Dickson R. M., Norris D. J., Tzeng Y.-L., Moerner W. E., Three-dimensional imaging of single molecules solvated in pores of poly(acrylamide) gels, *Science*, Vol. 274, 966–968, 1996
- [41] Nie S., Chiu D. T., Zare R. N., Probing individual molecules with confocal fluorescence microscopy, *Science*, Vol. 266, 1018–1021, 1994
- [42] Keller R. A., Ambrose W. P., Goodwin P. M., Jett J. H., Martin J. C., Wu M., Single-molecule fluorescence analysis in solution, *Appl. Spectrosc.*, Vol. 50, 12–32, 1996
- [43] Ha T., Enderle T., Ogletree D. F., Chemla D. S., Selvin P. R., Weiss S., Probing the interaction between two single molecules: Fluorescence resonance energy transfer between a single donor and a single acceptor., *Proc. Natl. Acad. Sci.*, Vol. 93, 6264–6268, 1996.
- [44] Ha T., Ting A. Y., Liang J., Caldwell W. B., Deniz A. A., Chemla D. S., Schultz P. G., Weiss S., Single-molecule fluorescence spectroscopy of enzyme conformational dynamics and cleavage mechanism., *Proc. Natl. Acad. Sci.*, Vol. 96, 893–898, 1999
- [45] Ha T., Zhuang X., Kim H. D., Orr J. W., Williamson J. R., Chu S., Ligand-induced conformational changes observed in single RNA molecules., *Proc. Natl. Acad. Sci.*, Vol. 96, 9077–9082, 1999
- [46] Jia Y., Talaga D. S., Lau W. L., Lu H. S. M., DeGrado W. F., Hochstrasser R. M., Folding dynamics of single GCN-4 peptides by fluorescence resonant energy transfer confocal microscopy, *Chem. Phys.*, Vol. 247, 69–83, 1999
- [47] Fries J.R., Brand L., Eggeling C., Köllner M., Seidel C.A.M., Quantitative identification of different single molecules by selective time-resolved confocal fluorescence spectroscopy, *J. Phys. Chem. A*, Vol. 102, 6601–6613, 1998
- [48] Deniz A. A., Dahan M., Grunwell J. R., Ha T., Faulhaber A. E., Chemla D. S., Weiss S., Single-pair fluorescence resonance energy transfer on freely diffusing molecules: Observation of Förster distance dependence and subpopulations, *Proc. Natl. Acad. Sci. USA*, Vol. 96, 3670–3675, 1999

-
- [49] Dahan M., Deniz A. A., Ha, T., Chemla D. S., Schultz P. G., Weiss S., Ratiometric measurement and identification of single diffusing molecules, *Chem. Phys.*, Vol. 247, 85–106, 1999
- [50] Deniz A. A., Laurence T. A., Beligere G. S., Dahan M., Martin A. B., Chemla D. S., Dawson P. E., Schultz P. G., Weiss S., Single-molecule protein folding: Diffusion fluorescence resonance energy transfer studies of the denaturation of chymotrypsin inhibitor 2, *Proc. Natl. Acad. Sci.*, Vol. 97, 5179–5184, 2000
- [51]] Sako Y., Minoguchi S., Yanagida T., Single molecule imaging of EGFR signalling on the surface of living cells, *Nat. Cell Biol.*, Vol. 2, 168–172, 2000
- [52] Frauenfelder H. et al., PROTEINS AND PRESSURE, *Journal of Physical Chemistry*, Vol. 94, 1024-1037, 1990
- [53] Heremans K., Smeller L., Protein structure and dynamics at high pressure, *Biochimica Et Biophysica Acta-Protein Structure and Molecular Enzymology*, Vol. 1386, 353-370, 1998
- [54] Hummer G. et al., The pressure dependence of hydrophobic interactions is consistent with the observed pressure denaturation of proteins, *Proceedings of the National Academy of Sciences of the United States of America*, Vol. 95, 1552-1555, 1998
- [55] Paladini A.A., Weber G., Pressure-Induced Reversible Dissociation Of Enolase, *Biochemistry*, Vol. 20, 2587-2593, 1981
- [56] Tekmen M., Müller J.D., High-pressure cell for fluorescence fluctuation spectroscopy, *Review of Scientific Instruments*, Vol. 75, 5143-5148 , 2004
- [57] Lakowitz J.R., *Principles of Fluorescence Spectroscopy*, Springer third edition, 2006
- [58] Winckler P., Jaffiol R., Multiphoton Cascade Absorption in Single Molecule Fluorescence Saturation Spectroscopy, *Analytical Chemistry*, Vol. 85, 4735-4744, 2013
- [59] Lang J.M., Dickamer H.G., High-pressure study of energy transfer between Coumarin 138 and Rhodamine B in a solid polymeric matrix, *J. Phys. Chem.*, Vol. 97, 5058–5064, 1993
- [60] Müller J. D., Gratton E., High-Pressure Fluorescence Correlation Spectroscopy, *Biophys. J.*, Vol. 85, 2711-2719, 2003

REFERENCES

- [61] Max B., Wolf E., Principles of Optics. Cambridge: Cambridge University Press, 461, 1999
- [62] Hecht E., Optik, Oldenbourg, 2009
- [63] Prummer M., Hübner C.G., Single Molecule Fluorescence: Biophysics, chapter 17, 2009
- [64] Webb R. H., Confocal optical microscopy, Reports On Progress In Physics, Vol. 59, 427–471, 1996
- [65] Haustein E., Schwille P., Single-molecule spectroscopic methods, Current Opinion in Structural Biology, Vol. 14, 531–540, 2004
- [66] Förster T., Zwischenmolekulare Energiewanderung und Fluoreszenz, Annalen der Physik, Vol. 2, 55–75, 1948
- [67] Stryer L. Haugland R.P., Energy transfer: A spectroscopic ruler, Proceedings of the National Academy of Sciences of the United States of America, Vol. 58, 719–726, 1967
- [68] Elson E. L., Magde D., Fluorescence correlation spectroscopy. i. conceptual basis and theory, Biopolymers, Vol. 13, 127, 1974
- [69] Magde D., Elson E., Webb W.W., Thermodynamic fluctuations in a reacting system-measurement by fluorescence correlation spectroscopy, Phys. Rev. Lett., Vol. 29, 705-708, 1972.
- [70] Krichевsky O., Bonnet G., Fluorescence correlation spectroscopy: the technique and its applications, Rep. Prog. Phys., Vol. 65, 251, 2002
- [71] Proctor B.A. , Whitney I. , Johnson J.W, The Strength of Fused Silica, JSTOR., Vol. 297, 534-557, 1967
- [72] Budynas R.G., Advanced Strength and Applied Stress Analysis, 2nd ed. McGraw-Hill, 348-352, 1999
- [73] Macomber J., Forest C.R., Polyimide Coated Capillary Tubing: Internal Pressure Capabilities, LCGC, The APPLICATION NOTEBOOK , 67, 2006
- [74] Kamin H. , Development of an heating system for a confocal microscope, Bachelor thesis, University of Lübeck, 2016

-
- [75] Vedam K., Limsuwan P., Piezo- and elasto-optic properties of liquids under high pressure-Refractive index vs. pressure and strain, *The Journal of Chemical Physics*, Vol. 69, 4762-4771, 1978
- [76] Privalov P.L.C., Cold Denaturation of Protein, *Rev. Biochem. Mol. Biol.*, Vol. 25, 281-306, 1990
- [77] Aznauryan M., Nettels D., Holla A., Hofmann H., Schuler B., Single-molecule spectroscopy of cold denaturation and the temperature-induced collapse of unfolded proteins, *J. Am. Chem. Soc.*, Vol. 135, 14040–14043, 2013
- [78] Mozhaev V.V., Heremans K., Frank J., Masson P., Balny, C., High pressure effects on protein structure and function, *Proteins-Structure Function and Genetics*, Vol. 24, 81–91, 1996
- [79] www.chemgapedia.de
- [80] Rouget J.B. et al., Size and sequence and the volume change of unfolding, *J. Am. Chem. Soc.*, Vol. 133, 6020–6027, 2011
- [81] Roche J. et al., Cavities determine the pressure unfolding of proteins, *Proc. Natl. Acad. Sci. USA*, Vol. 109, 6945–6950, 2012
- [82] Frye K.J., Royer C.A., Probing the contribution of internal cavities to the volume change of protein unfolding under pressure, *Protein Science*, Vol. 7, 2217–2222, 1998
- [83] Doster W., Friedrich J., Pressure-temperature phase diagrams of proteins, *Protein folding handbook*, WILEY-VCH, 2005
- [84] Berthelot M., *Ann. Chim.* Vol. 30, 232-237, 1850
- [85] Briggs L. J., Limiting Negative Pressure of Water, *J. Appl. Phys.*, Vol. 21, 721-722, 1950
- [86] Fersht A., *Structure and Mechanism in Protein science*, chapter 17, 518-521, 1999
- [87] Dill K.A., Denatured States of Proteins, *Annu. Rev. Biochem.*, Vol. 60, 795-825, 1991
- [88] Lobanov M., Galzitskaya O., How Common Is Disorder? Occurrence of Disordered Residues in Four Domains of Life, *Int. J. Mol. Sci.*, Vol. 16, 19490-19507, 2015

REFERENCES

- [89] Tanford. C., Protein Denaturation: Part C. Theoretical Models for The Mechanism of Denaturation , Adv. Protein Chem, Vol 24, 1-95 1970
- [90] Pace C. N., The stability of globular proteins, Crit. Rev. Biochem., Vol. 3,1-43, 1975
- [91] Tanford C., Protein Denaturation, Adv. Protein Chem., Vol. 23, 121-282, 1968
- [92] Rothman J. E., Kornberg R. D., An unfolding story of protein translocation, Nature, Vol. 322, 209-210, 1986
- [93] Verner K., Schatz G., Import of an incompletely folded precursor protein into isolated mitochondria requires an energized inner membrane, but no added ATP, EMBO J., Vol. 6, 2449-2456, 1987
- [94] Deshaies R.J., Koch B.D., Schekman R., The role of stress proteins in membrane biogenesis., Trends Biochem. Sci., Vol.13, 384-88, 1988
- [95] McLendon G., Radany E., Is protein turnover thermodynamically controlled?, Bioi. Chem., Vol. 253, 6335-37, 1978
- [96] Holzer H., Heinrich P. C. ,Control of Proteolysis, Annu. Rev. Biochem. Vol. 49, 63-92, 1980
- [97] Parsell, D. A., Sauer, R.T., The structural stability of a protein is an important determinant of its proteolytic susceptibility in Escherichia coli, Bioi. Chem., Vol. 264, 7590-95, 1989
- [98] Sanchez I.C., Phase transition behaviour of the isolated polymer chain, Macromolecules, Vol. 12, 980-988, 1979
- [99] Khechinashvili N.N., Janin J., Rodier F.,Thermodynamics of the temperature-induced unfolding of globular proteins, Protein Science, Vol. 4, 1315-1324, 1995
- [100] Levinthal C., Are there pathways for protein folding?, J. Chim. Phys., Vol. 65, 44-45, 1968
- [101] Levinthal, C., How to fold gracefully, Mössbauer Spectroscopy in Biological Systems, University of Illinois Press,Vol. 67, 22-24, 1969
- [102] Zwanzig, R., Szabo, A., Bagchi,B., Levinthal's paradox., Natl Acad.Sci. USA, Vol. 89, 20-22, 1992

- [103] Frauenfelder H., Sligar S.G., Wolynes P.G., The eenergy landscapes and motions of proteins, *Science*, Vol. 245, 1598-603, 1991
- [104] Frauenfelder H., Petsko G. A., Tsernoglou D., Temperature-dependent x-ray diffraction as a probe of protein structural dynamics, *Nature*, Vol. 280, 558-563, 1979
- [105] Ansari, J. Berendzen J., Bowne S.F., Frauenfelder H., Iben I. E., Sauke T. B., Shyamsunder E., Young R. D., Protein states and proteinquakes, *Proc. Natl. Acad. Sci. U. S. A.*, Vol. 82, 5000-5004, 1985
- [106] Baldwin R.L., Early Days of Studying the Mechanism of Protein Folding ,*Protein folding handbook*, WILEY-VCH, 2005
- [107] Anfinsen C. B., Haber E. , Sela M. , White F. H., The kinetics of formation of native ribonuclease during oxidation of the reduced polypeptide chain, *Proc. Natl. Acad. Sci. USA*, Vol. 47, 1309–1314, 1961
- [108] Dill K.D., Chan H.S., From Levinthal to pathways to funnels, *Nature structural biology*, Vol.4,10-18,1997
- [109] Mathematica notebook to generate frustrated energy landscapes (folding funnels), oaslab.com, Oas T.G., Departments of Biochemistry & Chemistry Duke University, North Carolina, USA
- [110] www.heraeus-quarzglas.com
- [111] www.qvf.com
- [112] Good NE., Winget GD., Winter W. et al., Hydrogen ion buffers for biological research. *Biochemistry*, Vol. 5, 467–477, 1966
- [113] Quinlan R.J., Reinhardt G.D., Baroresistant buffer mixtures for biochemical analyses, *Analytical Biochemistry*, Vol. 341, 69–76, 2005
- [114] Petrosian S.A., Makhatadze G.I., Contribution of proton linkage to the thermodynamic stability of the major cold-shock protein of Escherichia coli CspA, *Protein Science*, Vol.9, 387-394, 2000
- [115] Dellarole M., Royer C. A., High-Pressure Fluorescence Applications, Ch. 4, *Fluorescence Spectroscopy and Microscopy*, Springer protocols, 2014

REFERENCES

- [116] www.attotec.com
- [117] www.thermofisher.com
- [118] www.iss.com
- [119] Zhang Y.Z., Carter D., Multicolor Fluorescent Microspheres as Calibration Standards for Confocal Laser Scanning Microscopy, *Applied Immunohistochemistry& Molecular Morphology*, Vol.7, 156-163, 1999
- [120] <http://www.rcsb.org>
- [121] Kubin R. F., Fletcher A. N., Fluorescence quantum yields of some rhodamine dyes., *J. Luminescence*, Vol. 27, 455-462, 1982
- [122] Winckler P., Jaffiol R., Multiphoton Cascade Absorption in Single Molecule Fluorescence Saturation Spectroscopy *Analytical chemistry*, Vol. 85, 4735-4744, 2013
- [123] Bacia K., Schwille P., Practical guidelines for dual-color fluorescence cross-correlation spectroscopy, *Nature Protocols*, Vol. 2, 2842-2856, 2007
- [124] Scholz C., Eckert B., Hagn F., Schaarschmidt P., Balbach J., Schmid. F.X., Slyd proteins from different species exhibit high prolyl isomerase and chaperone activities, *Biochemistry*, Vol. 45,20-33, 2006.
- [125] Weininger U., Haupt C., Schweimer K., Graubner W., Kovermann M., Brüser T., Scholz C., Schaarschmidt P., Zoldak G., Schmid F.X., Balbach J., Nmr solution structure of slyd from escherichia coli: Spatial separation of prolyl isomerase and chaperone function, *J. Mol. Biol.*, Vol. 387, 295-305, 2009.
- [126] Seidel H., Einzelmoleküluntersuchungen zur Proteinkomplexbildung an den Modellsystemen ESAT-6/CFP-10 des *Mycobacterium tuberculosis* und NSP7/NSP8 des Felinen Coronavirus, 45-48, Dissertation, University of Lübeck, 2013
- [127] Kristoffersen A. S., Erga S.R., Hamre B., Frette Ø., Testing fluorescence lifetime standards using two-photon excitation and time-domain instrumentation: rhodamine B, coumarin 6 and lucifer yellow, *Journal of fluorescence*, Vol. 24, 1015–1024, 2014
- [128] Löw C. , Neumann P. , Tidow H. , Weininger U. , Haupt C. , Friedrich-Epler B. , Scholz C. , Stubbs M. T. , Balbach J., Crystal structure determination and functional characterization of the metallochaperone slyd from *thermus thermophilus*, *J. Mol. Biol.*, Vol. 398, 375-390, 2010

-
- [129] Tang Y., Schneider W.M., Shen Y., Raman S., Inouye M., Baker D., Roth M.J., Montelione G.T. Fully automated high-quality NMR structure determination of small (²H)-enriched proteins, *J. Struct. Funct. Genomics*, Vol.11, 223-32, 2010
- [130] He Y., Alam S.L., Proteasa S.V., Zhang Y., Lesuisse E., Dancis A., Stemmler T.L., Yeast frataxin solution structure, iron binding, and ferrochelatase interaction, *Biochemistry*, Vol.43, 16254-62, 2004
- [131] Vass H. and Allen R.J., Single-molecule imaging at high hydrostatic pressure, *Applied Physics Letters*, Vol. 102, 1541031-1541034, 2013
- [132] Haver T., Urayama P., An application of spatial deconvolution to a capillary-based high-pressure chamber for fluorescence microscopy imaging. *Journal of Microscopy*, Vol. 230, 363-371, 2008
- [133] Hoffmann A, Kane A, Nettels D, Hertzog D.E., Baumgartel P., Lengefeld J., Reichardt G., Horsley D.A., Seckler R., Bakajin O., Schuler B., Mapping protein collapse with single-molecule fluorescence and kinetic synchrotron radiation circular dichroism spectroscopy, *Proc. Natl. Acad. Sci. USA*, Vol. 104, 105-110, 2007
- [134] Neuweiler H., Sauer M., Using photoinduced charge transfer reactions to study conformational dynamics of biopolymers at the single-molecule level, *Curr. Pharm. Biotechnol.*, Vol. 5, 285-298, 2004
- [135] Gopich I.V., Szabo A., Single-macromolecule fluorescence resonance energy transfer and free-energy profiles, *J. Phys. Chem. B.*, Vol. 107, 5058-5063, 2003
- [136] Sherman E., Haran G., Coil-globule transition in the denatured state of a small protein, *Proc. Natl. Acad. Sci.*, Vol. 103, 11539-11543, 2006
- [137] Kuzmenkina E.V., Heyes C.D., Nienhaus G.U., Single-molecule FRET study of denaturant induced unfolding of RNase H, *J. Mol. Biol.*, Vol. 357, 313-324, 2006
- [138] Huang F., Sato S., Sharpe T.D., Ying L.M., Fersht A.R., Distinguishing between cooperative and unimodal downhill protein folding, *Proc. Natl. Acad. Sci.*, Vol. 104, 123-127, 2007
- [139] Tezuka-Kawakami T., Gell C., Brockwell D.J., Radford S.E., Smith D.A., Urea-induced unfolding of the immunity protein Im9 monitored by spFRET, *Biophys. J.*, Vol. 91, 42-44, 2006

REFERENCES

- [140] Lipman E.A., Schuler B., Bakajin O., Eaton W.A., Single-molecule measurement of protein folding kinetics, *Science*, Vol. 301, 1233-1235, 2003
- [141] Kohn J.E., Millett I.S., Jacob J., Zagrovic B., Dillon T.M., Cingel N., Dothager R.S., Seifert S., Thiyagarajan P., Sosnick T.R. et al., Random-coil behavior and the dimensions of chemically unfolded proteins, *Proc. Natl. Acad. Sci.*, Vol. 101, 12491-12496, 2004
- [142] Nicolini C. and Winter R., PressureTuning of the Morphology of Heterogeneous Lipid Vesicles: A Two-Photon-Excitation Fluorescence Microscopy Study, *Biophysical Journal*, Vol. 91, 2936-2942, 2006
- [143] Zhang J., Peng X., Jonas A., Jonas J., NMR study of the cold, heat, and pressure unfolding of ribonuclease A, *Biochemistry*, Vol. 34, 8361-8641, 1995
- [144] Meersman F., Smeller L., Heremans K., Pressure-assisted cold unfolding of proteins and its effects on the conformational stability compared to pressure and heat unfolding, *High Press. Res.*, Vol. 19, 263-268, 2000
- [145] Griko Yu.V., Kutysheko V.P., Differences of L-lactoglobulin cold and heat denaturations, *Biophys. J.*, Vol. 67, 356-363, 1994

Acknowledgement

Die letzten Zeilen dieser Arbeit sind all jenen gewidmet, die mir auf ganz unterschiedliche Art und Weise bei meinem Promotionsvorhaben geholfen haben.

Prof. Christian Hübner danke ich für seinen Optimismus und seine guten Ideen. Er hatte immer ein offenes Ohr für wissenschaftliche Fragestellungen und half selbst wenn der Druck mal zu hoch wurde. Verena Hirschfeld danke ich für die Einführung in die Benutzung der Setups und Labore, die FRET-auswertung sowie die Betreuung der Praktikumsversuche, Dana Kahra für das Labeling von slyD und die Hilfe beim Erlernen der FRET-messroutine. Erik Hinze möchte ich danken für die Herstellung und das Labeln der cspA-Probe. Auch Ben Schuler danke ich für die Möglichkeit Frataxin untersuchen zu können. Henning Seidel hat mir vor allem bei der Benutzung und Modifikation des Konfokalmikroskops geholfen und ich möchte ihm herzlich dafür danken. Lars Böttgers sei gedankt für erste Druckexperimente und die Einführung in die Verwendung einer Kapillare. Außerdem möchte ich natürlich allen Bachelor-und Masterstudenten danken, die mir eine große Hilfe waren. Es waren Daniela Breetholt, Janka Schwarzer, Thorben Blömker, Kim Reiter und Hannes Kamin, die einen Beitrag zu meiner Arbeit geleistet haben.

Außerdem danke ich meiner Familie für alles und ganz besonders danke ich meiner Freundin für das Korrekturlesen und ihr Interesse an meiner Arbeit.

Erklärung

Hiermit erkläre ich, dass ich keine anderen als die von mir angegebenen Quellen und Hilfsmittel zur Erstellung meiner Dissertation verwendet habe. Den benutzten Werken wörtlich oder inhaltlich entnommene Stellen sind als solche gekennzeichnet.

Sven Schneider

Lübeck, den 24. April 2017

Curriculum Vitae



Personal data:

name	Sven Schneider
adress	Parchamstr. 2a, 23554 Lübeck
date of birth and place	19.3.1984 in Freiburg im Breisgau

Education:

09 1994 – 06 2003	Rotteck-Gymnasium (Allgemeine Hochschulreife), Freiburg im Breisgau
09 2003 - 07 2004	civilian service, Diakonie Michaelshoven, Cologne
10 2004 - 09 2011	study of physics (Diplom Physiker), Ludwig Maximilians University of Munich
01 2012 -	phd student at the Institute of physics, University of Lübeck

Scientific contributions

Talks:

- "Single molecule FRET under high pressure", 8th North German Biophysics Meeting, Research Center Borstel, 2015
- "Pressure unfolding of a model folding protein followed by smFRET", 21st International Workshop on "Single Molecule Spectroscopy and Super-resolution Microscopy in the Life Sciences", Picoquant, Berlin 2015
- "Pressure unfolding of CspA followed by single molecule FRET", 26th Faltertage on "Protein Folding, Dynamics and Stability", Martin-Luther-University Halle-Wittenberg, Halle 2015

Posters:

- "Single-molecule fluorescence detection in fused silica capillaries", Annual Meeting of the German Biophysical Society, Göttingen, 2012
- "Single-molecule fluorescence detection in fused silica capillaries", 6th North German Biophysics Meeting, Research Center Borstel, 2013
- "Detektion einzelner Fluoreszenzmoleküle in Quarzglas kapillaren", Uni im Dialog 7. Lübecker Doktorandentag, Lübeck, 2013
- "Single-molecule fluorescence detection in fused silica capillaries", 19th International Workshop on "Single Molecule Spectroscopy and Super-resolution Microscopy in the Life Sciences", Picoquant, Berlin, 2013
- "Single-molecule fluorescence detection in fused silica capillaries", 7th North German Biophysics Meeting, Research Center Borstel, 2014
- "Single-molecule fluorescence detection in fused silica capillaries", XVI. Annual Linz Winter Workshop in Linz, Austria, 2014
- "Single-molecule FRET in fused silica capillaries under pressure", Annual Meeting of the German Biophysical Society, Lübeck, 2014
- "Single-molecule FRET in fused silica capillaries under high pressure", 10th European Biophysics Congress, Dresden, 2015

- “Pressure unfolding of a model folding protein followed by smFRET”, International Discussion Meeting “Förster Resonance Energy Transfer in life sciences: FRET 2”, Max Planck Institute for Biophysical Chemistry Göttingen, Germany, 2016
- “Pressure unfolding of a model folding protein followed by smFRET”, 10th North German Biophysics Meeting, Research Center Borstel, 2017